QUANTUM MONTE CARLO
WITH A STOCHASTIC POTENTIAL SOLVER

BY

DYUTIMAN DAS

B.Sc., Presidency College, University of Calcutta, 1997
M.Sc., Indian Institute of Technology, Kanpur, 1999
M.S., University of Illinois at Urbana-Champaign, 2001

DISSERTATION

Submitted in partial fulfillment of the requirements
for the degree of Doctor of Philosophy in Physics
in the Graduate College of the
University of Illinois at Urbana-Champaign, 2005

Urbana, Illinois

QUANTUM MONTE CARLO
WITH A STOCHASTIC POTENTIAL SOLVER

Dyutiman Das, Ph.D.
Department of Physics
University of Illinois at Urbana-Champaign, 2005
Richard M. Martin, Adviser

Quantum Monte Carlo (QMC) is an extremely powerful method to treat many-body systems. Usually QMC has been applied in cases where the interaction potential has a simple analytic form, like the $1/r$ Coulomb potential. However, in a complicated environment as in a semiconductor heterostructure, the evaluation of the interaction itself becomes a non-trivial problem. Obtaining the potential from any grid-based finite-difference method, for every walker and every step is unfeasible. We demonstrate an alternative approach of solving the Poisson equation by a classical Monte Carlo within the overall QMC scheme. We have developed a modified "Walk On Spheres"(WOS) algorithm using Green's function techniques, which can efficiently account for the interaction energy of walker configurations, typical of QMC algorithms. This stochastically obtained potential can be easily incorporated within popular QMC techniques like variational Monte Carlo (VMC) or diffusion Monte Carlo(DMC). We demonstrate the validity of this method by studying a simple problem, the polarization of a helium atom in the electric field of an infinite capacitor. Then we apply this method to calculate the singlet-triplet splitting in a realistic heterostructure device. We also outline some other prospective applications for spherical quantum dots where the dielectric mismatch becomes an important issue for the addition energy spectrum.

To all those who inspired me, both living and dead.

Acknowledgments

This thesis was made possible by the patronage and support of a large number of people through direct assistance, advice or just by being there, a support so crucial during the long years of graduate school. I am much indebted to them all. A few words of gratitude does not do justice to the true impact of the community (professional, social and personal) on this work and my general education. Here I attempt to thank the most prominent among them.

The most prominent influence of all, has been of course my tutelage under Prof. Richard Martin. I recall with both relief and heartfelt gratitude of how Richard accepted me as a student in spite of my considerable indecisiveness. It was the summer of 2000; I needed to figure out which area of research I would pursue for the rest of my life (or so I thought then). But the diversity in sub-areas of physics available for research overwhelmed me and I was unable to make up my mind. I had talked to Richard before, but had decided to work in plasma physics for the summer. At the end of that summer I came back, and Richard was still willing to accommodate me. Another week of indecision followed, and with help from Prof. Jim Wolfe (then graduate chair) I was able to obtain a teaching assistantship (even though classes had started for fall). Without the understanding and support of these two men, I would be writing a very different thesis; I am very grateful for the opportunity I was given.

Over the years that followed, I found Richard to be one of the most caring, supportive and patient men I have ever known. As an adviser he gave me a lot of attention even when he was on sabbatical; we worked very closely in the initial stages of the project, and yet he allowed me the freedom to develop my own ideas and steer the project as I saw fit. His deep insight and broad knowledge of the field was immensely helpful; his continuous support and encouragement was a driving force behind this work. I would also like to thank him for providing me with the wonderful opportunity to visit The Lawrence Livermore National Laboratories twice in Livermore, CA during

his sabbatical there. Also because of his support I was able to visit different cities in the United States while attending the APS March meetings. Many thanks to Richard for everything.

Jeongnim Kim joined our research group in the fall of 2001, and over the course of time became almost my second adviser. Whenever I had questions or doubts, she made time even when she was busy. She was invaluable in providing computer support, compiling arcane codes or implementing the latest parsers. She facilitated my transition from FORTRAN to C++, and imparted numerous tips, like those that are not often found in books but which comes from long years of experience. Most of the calculations of this thesis were carried out using QMC++ an object oriented quantum Monte Carlo code jointly written by Jeongnim Kim and Jordan Vincent. Not just writing the basic code, Jeongnim also provided me with constant help in implementing my algorithms within the overall structure of QMC++. I owe a lot to Jeongnim.

The ideas behind this thesis grew long before my entry into the field, through works of David Ceperley and John Shumway. Thanks are due to David for coming up with this neat idea of solving the potential by a Monte Carlo, during the quantum Monte Carlo simulation. David's presence has been a great influence, he was extremely helpful in introducing me to the penalty method which we adapted into the algorithm. Time and again he has made several suggestions and insights which have increased my understanding of Monte Carlo in general. His class on "Atomic Scale Simulations" was my first introduction to Monte Carlo. I must also thank John Shumway for several comments regarding spherical dots, and volunteering his QMC code. Though I used QMC++, initially going through his code was a very good learning process.

Another person instrumental to this project has been Dr. Mal Kalos. I met Dr. Kalos during my visit to Livermore, CA in the spring of 2002. In spite of our considerable difference in age I immediately felt very good rapport with his jovial nature. Though I was working with Richard (and later I learnt it was originally David's idea) it was Dr. Kalos who first pitched the idea of this thesis to me. His expansive knowledge of Monte Carlo methods, and extremely lucid explanation of otherwise difficult or confusing subjects were very helpful for my understanding. Much of what I know of Monte Carlo today I learned from Dr. Kalos's book, "Monte Carlo Methods". Later, during the preparation of our manuscript, his suggestions not only simplified several key concepts, but also improved the overall quality of the paper. But aside from the above I would also like to

commend him for discovering "The Iron Works" BBQ shack in Austin, TX where we had many delightfully interesting conversations.

I also received considerable help in our collaboration with the computational electronics group. I would like to thank Prof. Jean-Pierre Leburton, Lingxiao Zhang and Dmitriy Melnikov. Prof. Leburton has been very generous in extending his cooperation and has helped me with many useful discussions regarding the nature of heterostructure devices. I also learned a lot about semiconductor electronics from his class. Lingxiao especially had helped me a lot with obtaining data, and preparation of graphs for presentations. Recently, Dmitriy has also been invaluable in providing the input data: the device structure, the DFT solutions of potential, charge density and trial wavefunctions. Their insight was also indispensable in discussions on the heterostructure device. Both Lingxiao and Dmitriy were always available to answer questions or clarify doubts.

I have been very fortunate to be in a group with dear friends like Jordan Vincent, Nick Romero and Ken Esler. Both Nick and Ken were of great help in providing much needed computer support. Jordan not only helped with the QMC++ code, but was also a great companion in my two visits to Livermore, CA. I also had a very successful collaboration with another friend Tsu-Chieh Wei, much thanks are due to him as well.

This acknowledgment would be incomplete without the mention of the many friends in the physics class of 1999 who welcomed me to the United States, and made me a part of the class. I would like to thank Jeff Reifenberger, Jordan Vincent, John Veysey, Ken Esler, Ziggy Majumdar, Jack Sadleir, Hector Garcia-Martin, Kapil Rajaraman, Dom Ricci, Michelle Nahas and Nick Romero for all kinds of help and companionship that is too long to narrate. Argyrios Tsolakidis has also been a great friend, incidentally he also left me his car when he graduated, it has been of immense use to me.

My parents Debashis and Utpala Das have been pillars of support and encouragement throughout my life. Their silent backing of all my endeavors have made it possible for me to reach this stage. Financial limitations have prevented me from visiting home as often as I would have liked, and they have patiently born my absence for the last several years. I hope in the end it will all be worthwhile. I would also like to thank my cousin Dolonchampa Basu and her husband ParthaSarathi for their constant support, encouragement and help.

I would also like to thank the departmental staff for their supporting role, especially Wendy Wimmer and Dawn Sommers who have been of considerable help regarding various departmental needs. Lastly, I would like to thank the entire committee for making time to oversee this thesis.

This work was supported by the National Science Foundation under Grants No. DMR99-76550 and DMR-0325939 for the Materials Computation Center at the University of Illinois at Urbana-Champaign, U.S. Department of Energy under Contract No. DEFG02-91ER45439 for the Frederick Seitz Materials Research Laboratory. For an intermediate period I was also supported by the National Science Foundation grant DMR01-04399. Much of the computation in this work was performed on the following computers: University of Illinois at Urbana-Champaign Materials Computation Center IBM RS/6000 cluster and National Center for Supercomputing Applications (2500 dual processor) Tungsten cluster. I would also thank Lawrence Livermore National Laboratories for making possible my visit to Livermore during the spring and summer of 2002 at which time I started my collaboration with Dr. Mal Kalos which led to this saga.

Table of Contents

List of Tables

List of Figures

List of Abbreviations

DFT Density Functional Theory

DMC Diffusion Monte Carlo

FEM Finite Element Method

GFMC Green Function Monte Carlo

LCQD Laterally Coupled Quantum Dots

LDA Local Density Approximation

LSDA Local Spin Density Approximation

NBF Nearest Boundary Face

QMC Quantum Monte Carlo

STM Scanning Tunneling Microscope

VMC Variational Monte Carlo

WOS Walk On Spheres

Chapter 1

Introduction

Simulation of an N-particle quantum system is essentially solving the Schrödinger's equation involving the $3N$-dimensional wave-function which defines the state of the system. Stochastic methods like quantum Monte Carlo (QMC) are very appropriate, useful and accurate to treat systems of such large dimensionality [8, 23]. These methods have been applied extensively to study properties like cohesive energies of molecules [28], solids [21], properties of the electron gas [9, 53], solid hydrogen [10, 55], clusters [25] and much more.

Recently there has been great interest in studying semiconductor devices operating in highly quantum regimes, like quantum dot devices [2], quantum wires[58], single electron transistors[40] etc. For simulation purposes structural details of these devices are usually represented by simple analytically tractable models[29]. However these models sometimes lead to an inadequate description of the interaction energies[65]. There have been only a limited number of applications of QMC to realistic models of such physical devices capturing the details of the potential profile [48], and even this known work has been restricted to making simplifying assumptions on the form of the potential. The reason is that while simulation of natural or idealized structures involve interactions with simple analytic forms (like Coulomb, Lennard-Jones etc.), the interaction in artificial devices is too complicated to be efficiently treated within QMC. Our goal is to extend the application of QMC to semiconductor devices in a simple and straightforward way.

Among the several QMC methods, we will mainly focus on zero temperature methods like variational Monte Carlo (VMC) [11] and diffusion Monte Carlo (DMC), since these are the simplest to code and most extensively used. We should mention here that our approach can also be used in conjunction with any other kind of quantum or classical Monte Carlo algorithms. The methods we

are concerned with, i.e. variational and diffusion Monte Carlo both follow the same basic idea, they calculate expectation of observables associated with a particular state of the system. Consider an N-particle system, and denote the coordinate of the i-th particle by $\boldsymbol{q}_i$. The simulation generates a set of M configurations $\{\boldsymbol{R}\}$, called "walkers".

$$\{\boldsymbol{R}\} = \boldsymbol{R}_1, \ldots, \boldsymbol{R}_m, \ldots, \boldsymbol{R}_M. \quad \boldsymbol{R}_m = \{\boldsymbol{q}_1, \ldots, \boldsymbol{q}_N\} \; \forall \; m,$$

i.e. each walker is a realization of the system in a particular configuration. The algorithm to generate $\{\boldsymbol{R}\}$ depends on the method involved, but it results in the walkers being distributed according to (or something close to) Ψ^2, where Ψ is the relevant state. Accurate estimate of any observable can then be obtained.

Application of these methods to an entire device structure can be prohibitively expensive. Progress can be made by isolating the physical region dominated by quantum mechanics from the background, which can be treated semi-classically. The walkers are created only in the quantum region and are confined there. The potential profile in this region is thus governed by the complicated inter-particle interactions, the effect of the semi-classical background, induced image charges and the gate voltages on the surface boundary of the device. The net effect in general is very complicated.

This potential profile is however the defining characteristic of the system. The QMC algorithms inevitably involve repeated computation of the potential energy $V(\boldsymbol{R}_m)$ of each walker configuration $\boldsymbol{R}_m$ during and after their evolution into the final equilibrium distribution. In general, there will be no analytic expression for $V(\boldsymbol{R}_m)$ except in highly idealized cases, and will have to be obtained as an explicit solution of Poisson's equation at every step. This is unfeasible for any grid based finite element like method.

The only application [48] of QMC to realistic devices that we know of, circumvents this by approximating the background potential by a self-consistent Poisson-Schrödinger solution using an LSDA quantum charge density. The walkers move around in this rigid background, and the particles interact by a simple Coulomb interaction. But strictly speaking, the interaction is not Coulomb-like, it is modified by the induced charges at dielectric interfaces and metal surfaces. Also the LSDA approximation itself breaks down for highly correlated systems producing theoretically

impossible results like predicting phase transitions in finite systems [43, 31]. However, we will show that QMC can be applied to realistic models of such systems without these approximations, if we can solve the potential stochastically.

Our stochastic approach has several advantages. Traditional grid based methods expend a lot of computation in solving the equation at all grid points over the entire device. These grid points are placed at discrete intervals, and thus limit the resolution of the device structure. This resolution can be increased only at considerable cost. However, the stochastic method obtains the solution only at the desired points (for e.g. the walker configuration $\boldsymbol{R}_m$). Secondly, this does not suffer from the resolution issues of the grid based methods, any point can be treated with arbitrary accuracy. Moreover, the stochastic methods can handle regions of very sharp gradients much more effectively than grid based counterparts.

Furthermore we will demonstrate that the stochastically obtained potential can be easily used within the QMC framework. We need not solve the potential energy of each walker configuration with great degree of accuracy, but that the QMC algorithm will eliminate the noise in the potential. In essence what we are performing is a Monte Carlo (classical potential solver) within another Monte Carlo (quantum Schrödinger solver).

Monte Carlo methods find wide applicability in diverse areas of numerical research, and this technique can be adapted in fields outside of atomic scale simulations as well. For example, in quantitative finance, the stock price is assumed to react to the flow of information coming into the market, and as a result the return on the stock (the logarithm of the stock price) is assumed to undergo a Brownian motion. Prices of options and other instruments are often estimated based on Monte Carlo simulation of the stock price. This estimation however also depends on the interest rates prevailing in the market, which in complicated models follow a Brownian motion of its own. Due to the log-normal (logarithm of stock price is distributed normally) nature of the stock movement, the equations are very similar to the branching process of diffusion Monte Carlo, and so our approach will also be applicable to such financial problems.

This thesis is organized as follows. In chapter 2, we discuss the stochastic method of computing the potential. Then in chapter 3 we show how this potential is easily incorporated within QMC calculations. We also illustrate the modifications necessary for DMC to incorporate this stochastic

potential. In chapter 4 we implement the method in the context of a simple toy problem, namely placing a helium atom within the plates of an infinite capacitor and measuring the polarizability. Though the geometry is simple, this problem illustrates most of the important features of the algorithm. However, we also consider a far more complicated device in chapter 5, where we apply this method to a realistic model of a semiconductor heterostructure with complicated gate geometry, and compute and compare the singlet-triplet splitting of a two electron double dot. In chapter 6 we draw conclusions.

The appendices also provide additional information regarding background material and details of calculations. In appendix A we describe several Monte Carlo sampling techniques, both standard methods from textbooks and those developed during the course of this work. In appendix B we lay down the algorithm for the WOS calculations. In appendix C we describe another possible important application of the method; a spherical double quantum dot. The electronic interaction between particles near a dielectric sphere is difficult to compute analytically, however this would not pose any problem for the stochastic method, and hence this can be applied to study spherical dots between metal plates of device like a scanning tunneling microscope. In appendix D we provide the scaling of fundamental units to the effective atomic units appropriate for calculations in semiconductors. The QMC calculations of the realistic heterostructure required input data from previous density functional calculations, and these we implemented by interpolating data on a grid using tricubic splines which we describe in appendix E.

Chapter 2

Stochastic Potential Solver

The probabilistic potential theory arises from a connection between Brownian motion and classical potential theory, first made by Kakutani in 1949 [37]. Interestingly, the first use of Monte Carlo to solve Schrödinger's equation, by Fermi, Metropolis, Ulam et al was also around the same time in 1948 [52]. However, Muller [54] was the first to layout a detailed mathematical framework and algorithm to solve Laplace's equation, which was later developed by Haji-Sheikh [27] when he applied this method for non-zero constant heat-source term. Physically heat flow, natural diffusion, Brownian motion and potential, all follow similar diffusion equations and hence can be solved by similar stochastic methods. A nice and more detailed introduction can be found in the work of Bevensee[4] and Port [61].

2.1 Brownian Motion and Potential Problem

Brownian motion gets its name from the corresponding physical process reported on in 1828 by Robert Brown, an English botanist. He observed that pollen grains suspended in water perform a continuous swarming motion. Einstein in 1905, unaware of the accumulating experimental data, derived Brownian motion from statistical mechanical considerations (see works of Einstein [19] and Nelson for an historical perspective). Slightly earlier in 1900 Bachelier [3] used Brownian motion to model the fluctuations of prices of such securities as futures and options and to study various methods of hedging.

The connection between potential theory and Brownian motion comes from the nature of harmonic functions which are solutions of the Dirichlet problem, i.e. for which the solution is provided

on the entire boundary. The Dirichlet problem was first solved by Gauss in 1840, but it was Wiener [71] who first formulated the generalized Dirichlet problem which always has a solution. But neither made the connection with Brownian motion until Kakutani [37] and Doob [18]. In the intervening period Courant, Friedrichs, and Lewy [14] noted an indirect connection between the two subjects. Namely, they noted that the solution to the discrete version of the Dirichlet problem (which converges to the solution of the original problem under appropriate conditions as the grid size tends to zero) has an interpretation in terms of simple random walk. This leads to the "Fixed Random Walk".

2.1.1 Fixed Random Walk

The fixed random walk procedure can be easily understood as a finite difference approximation of Laplace's equation. For this purpose we superpose a uniform grid of length ℓ on a two dimensional region of interest Ω with boundary $\partial\Omega$ as shown in Fig.(2.2). The algorithm can be trivially extended to three dimensions. Consider Laplace's' equation (in 2D),

$$\nabla^2\Phi(x,y) = \nabla_x^2\Phi(x,y) + \nabla_y^2\Phi(x,y) = 0$$

Using a finite difference approximation for the second derivative, it is readily seen that the potential at any point $\Phi(x,y)$ is simply the average of the potential at the surrounding mesh points.

$$\Phi(x,y) = p_{x_+}\Phi(x+\ell,y) + p_{x_-}\Phi(x-\ell,y) + p_{y_+}\Phi(x,y+\ell) + p_{y_-}\Phi(x,y-\ell) \tag{2.1}$$

where

$$p_{x_+} = p_{x_-} = p_{y_+} = p_{y_-} = 1/4$$

The two equations can be given a probabilistic interpretation; that is if a random-walking particle is instantaneously at the point $(x.y)$ it has an equal probability (1/4-th to be precise) of stepping to any of the neighboring lattice points. The p-s are the associated probabilities for each possibility. In three dimensions $p = 1/6$, and so we see that the potential at any point is simply the average over its neighbors.

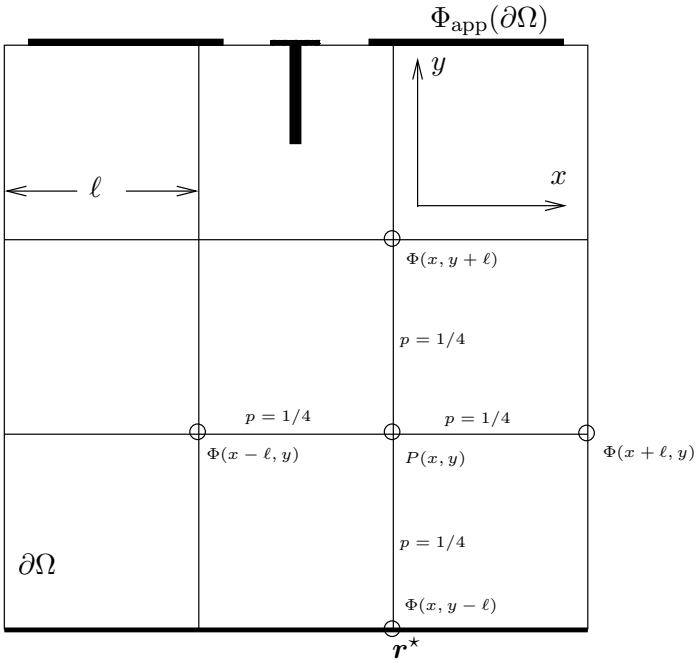

Figure 2.1: Fixed Random Walk on a fixed grid two-dimensional discretization of a system. To evaluate the potential at the point $P(x, y)$ the walk hops to one of the neighboring points with equal probability. The walk continues until it reaches the external boundary. See the section above for details.

2.1.2 Floating Random Walk

A simple extension of the above method is the "Floating Random Walk" where neither the lattice points nor the the step sizes are fixed and hence the name of the algorithm. This approach can not only solve the potential at any arbitrary point (not just lattice points), but has the added advantage of faster convergence. The main idea as before is best illustrated in a charge free system (Laplace's equation), the basic idea being same even for the completely general problem as will be shown later.

We know the solutions of Laplace's equation are harmonic functions which obey the Mean Value Theorem [74]

$$\Phi(\boldsymbol{q}) = \frac{1}{4\pi d^2} \int \Phi(\boldsymbol{r}') d^2\boldsymbol{r}' \tag{2.2}$$

i.e. as we saw for the discrete case, the potential $\Phi(\boldsymbol{q})$ at any point $\boldsymbol{q}$ is the average of the potential over a sphere or arbitrary radius d centered at $\boldsymbol{q}$. We assume Dirichlet boundary condition for now, i.e. the potential is specified on the external surface, as is often the case in practical situations where the external biases are applied through surface gates. The algorithm can be easily extended

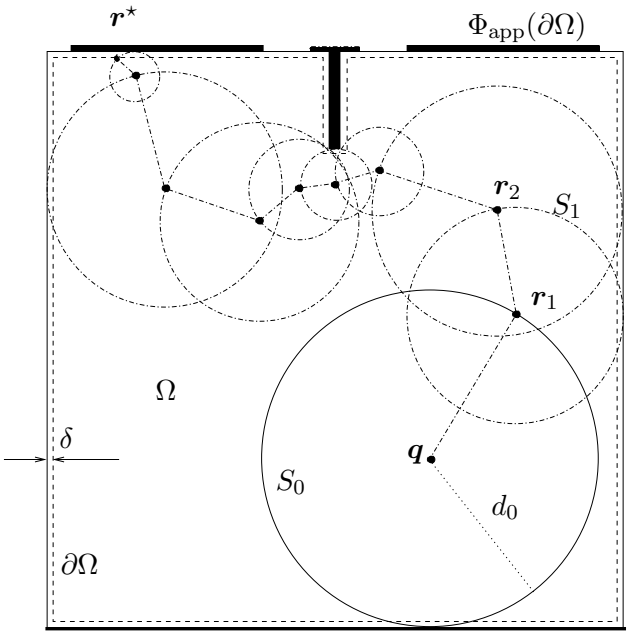

Figure 2.2: A Walk On Spheres: A generic device with metal gates on surface held at arbitrary voltages. Start by constructing the maximum sphere S_0 of radius d_0 centered on $P(\boldsymbol{q})$. Sample a point $\boldsymbol{r}_1$ uniformly on S_0. Repeat the process by constructing sphere S_1 etc. The walk ends when the sampled point $\boldsymbol{r}^\star$ is within a range δ of boundary $\partial\Omega$. Such walks will never end exactly on the boundary, but with $\delta \ll d_0$ the estimate can be made arbitrarily accurate.

for Neumann boundary conditions as in the discrete case. A simple random walk algorithm "Walk On Spheres" (WOS) due to Muller [54] can solve Eq.(2.2) in a very elegant way.

Consider a region Ω with external boundary $\partial\Omega$ where the potential $\Phi_{\rm app}(\boldsymbol{r})$ is specified for $\boldsymbol{r} \in \partial\Omega$, see Fig.(2.2). To obtain the potential at any point $\boldsymbol{q} \in \Omega$, construct the largest possible sphere S_0 centered at $\boldsymbol{q}$ but fully contained within Ω. Such constructions will be called the "maximum sphere" following Muller. The radius of the sphere is simply the minimum distance from $\boldsymbol{q}$ to the boundary $\partial\Omega$. The averaging of Eq.(2.2) is carried out by sampling points $\boldsymbol{r}_1$ (and the potential $\Phi(\boldsymbol{r}_1)$) uniformly over the surface of S_0. Hence the solution $\Phi(\boldsymbol{q})$, represented by the estimator $\langle\tilde{\Phi}(\boldsymbol{q})\rangle$ is given by $\langle\Phi(\boldsymbol{r}_1)\rangle$. Here $\tilde{\Phi}(\boldsymbol{q})$ is the estimate of an individual sample.

But of course, the potential $\Phi(\boldsymbol{r}_1)$ is unknown, and thus we need to continue the process giving rise to a "walk" as illustrated in Fig.(2.2). A maximum sphere is constructed centered about $\boldsymbol{r}_1$, and a point $\boldsymbol{r}_2$ is sampled on its surface, and the walk continues until the sampled point $\boldsymbol{r}^\star$ lies on or very close to (i.e. within some "skin" region of width δ from) the boundary $\partial\Omega$, where the potential is known; $\Phi(\boldsymbol{r}^\star \in \partial\Omega) = \Phi_{\rm app}(\boldsymbol{r}^\star)$. This generates a walk $\boldsymbol{q} \to \boldsymbol{r}_1 \to \boldsymbol{r}_2 \cdots \boldsymbol{r}^\star$, see Fig.(2.2). An

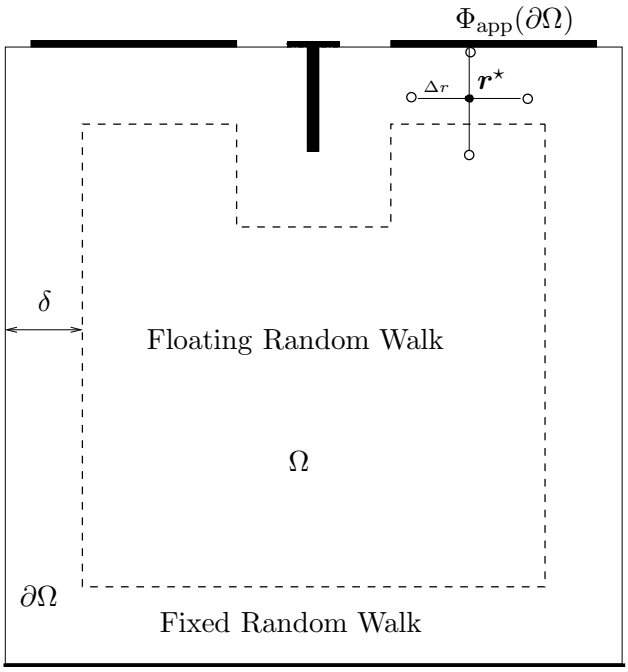

Figure 2.3: When the walk reaches a point $\boldsymbol{r}^\star$ a distance Δr ($\Delta r \leq \delta$, i.e. within the skin region, exaggerated here for clarity) from the surface, a grid of width Δr is constructed with $\boldsymbol{r}^\star$ as a grid point. The walk continues by sampling a neighboring grid point, and terminates when it reaches a boundary point. Thus the algorithm performs a floating random walk in the bulk of the device and a fixed random walk in the skin region.

average over many such walks will provide an estimate of the potential at $\boldsymbol{q}$, the starting point. Hence, $\langle\tilde{\Phi}(\boldsymbol{q})\rangle = \langle\Phi_{\text{app}}(\boldsymbol{r}^\star)\rangle$.

Thus, for $\mathcal{N}$ such walks the mean of the estimate is

$$\langle\tilde{\Phi}(\boldsymbol{q})\rangle = \lim_{\mathcal{N}\to\infty} \frac{1}{\mathcal{N}} \sum_{n=1}^{\mathcal{N}} \Phi_{\text{app}}(\boldsymbol{r}_n^\star),$$

with an error of

$$\delta\tilde{\Phi}(\boldsymbol{q}) = \lim_{\mathcal{N}\to\infty} \frac{1}{\mathcal{N}-1} \left[\frac{1}{\mathcal{N}} \sum_{n=1}^{\mathcal{N}} \Phi_{\text{app}}^2(\boldsymbol{r}_n^\star) - \langle\tilde{\phi}(\boldsymbol{q})\rangle^2 \right].$$

2.2 Boundary conditions

In the actual application of the random walk algorithms care should be taken of the possibly time consuming progress of the walk when it is near an external surface. When the random walk approaches an external surface, the radius d_k of the sphere defining the locus of the next step

becomes correspondingly small and hence convergence to the boundary is slowed down. Moreover, the spherical surface intersects a planar external boundary in exactly one point, and hence the probability of sampling a surface point is exactly zero. This is why the discussion in the previous section was simplified by terminating the walk when it reached a skin region of width δ near the external boundary.

That the WOS indeed converges to an external boundary with probability one has been shown in the mathematical works of Kakutani [37] and Muller [54]. Taking this for granted we can employ several approximate representations of the boundary for the Dirichlet problem, i.e. for the case where the external surface is at a known boundary potential $\Phi_{\text{app}}(\boldsymbol{r})$ with $\boldsymbol{r} \in \partial\Omega$. This is the case when for example a bias is applied to a device by means of metal gates on the surface. The metals are equipotentials controlled by the connected (and known) voltage sources. Haji-Sheikh [27] discusses some of the following choices:

(a) As described earlier terminate the walk when it is within a skin depth δ of the external surface and sample potential at the nearest boundary point.

(b) If at any step the walk moves to an angular position that deviates less than a preassigned quantity $\pm\theta_{\text{min}}$ from the position where the sphere intersects the external surface, the walk is terminated. This is similar to the above condition.

(c) When the walk reaches the skin region, a fixed random walk is employed to establish probabilities for the next step of the walk, Fig(2.3). For some problems it might be convenient to employ a one-dimensional form along the direction normal to the surface.

Thus when the walks reach a boundary with a specified potential, they are terminated. Such boundaries are called *absorbing* barriers. Next, consider the situation when the boundaries have specified Neumann boundary condition, i.e. the electric field is specified on the boundary rather than the potential itself. From Fig.(2.4),

$$\Phi_0 \approx \Phi_- - \mathcal{E}_x \Delta x$$

The probabilistic interpretation is to reflect the walk by the same distance Δr that the walk is

away from the surface and accumulate the quantity $-\mathcal{E}\Delta r$. Such boundaries are called *reflecting* barriers.

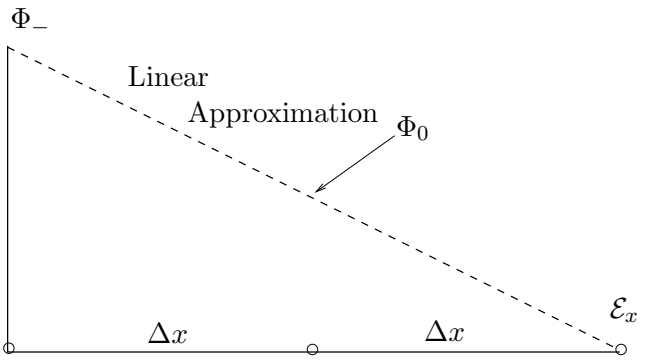

Figure 2.4: Reflecting boundary condition with a linear approximation.

There can also be convective boundary condition which is equivalent to a *partial absorbing, partial reflecting* barrier. More elaborate discussions can be found in the referenced literature.

2.3 The Green's Function Approach

Much insight into the above method can be obtained from a full mathematical treatment of the general problem, namely the Poisson's equation

$$\nabla^2\Phi(\boldsymbol{r}) = -\rho(\boldsymbol{r})/\varepsilon \tag{2.3}$$

where $\rho(\boldsymbol{r})$ is the charge density and ε is the dielectric constant of the medium. Keeping in mind the discrete nature of walker configurations in quantum Monte Carlo we are interested in the potential at a point $\boldsymbol{r}$ due to another point charge at $\boldsymbol{r}'$, given everything else in the problem. This is embodied in the idea of the Green's function, defined as

$$\begin{aligned} \nabla'^2 \quad G(\boldsymbol{r},\boldsymbol{r}') &= -\delta(\boldsymbol{r}-\boldsymbol{r}') \qquad \boldsymbol{r},\boldsymbol{r}' \in \Omega \\ G(\boldsymbol{r},\boldsymbol{r}') &= 0, \qquad \boldsymbol{r}' \in \partial\Omega \end{aligned} \tag{2.4}$$

where Ω is *any* volume within the region, and $\partial\Omega$ is the surface of that volume. Without loss of generality let's denote by Ω the entire system volume. The second equation in Eqs.(2.4) is a

consequence of Dirichlet boundary condition. In terms of this Green's function, the potential $\Phi(\boldsymbol{r})$ at any point $\boldsymbol{r}$ is given by [33](pp 44, Eq.(1.44)),

$$\Phi(\boldsymbol{r}) = \int_{\Omega} \rho(\boldsymbol{r}')G(\boldsymbol{r},\boldsymbol{r}')d^3\boldsymbol{r}' + \int_{\partial\Omega} d^2\boldsymbol{r}' \cdot \nabla G(\boldsymbol{r},\boldsymbol{r}')\Phi(\boldsymbol{r}') \tag{2.5}$$

i.e. the potential has contributions from both the volume charges (like doped charges, or electron density) and the boundary potential (like voltages applied to metal gates on the surface). also we need to know the potential $\Phi(\boldsymbol{r}')$ on the surface. Thus the Green's function plays a crucial role in the inter-particle interactions. We stress again that Eq.(2.5) holds for any volume Ω not just the entire volume as we have used here.

As we will show, a method called the domain Green's function Monte Carlo (dGFMC) [38], originally developed to solve Schrödinger's equation evaluates both integrals in Eq.(2.5) simultaneously. This is not surprising given the connection between diffusion (like imaginary time Schrödinger's equation), Brownian motion and potential theory. The key idea is to realize that Eq.(2.5) holds for any domain $\mathcal{D}$ of any arbitrary shape which is not necessarily the entire system volume Ω. This will require a redefinition of the Green's function $G_{\mathcal{D}}(\boldsymbol{r},\boldsymbol{r}')$ to be defined only within the domain $\mathcal{D}$ with surface $\partial\mathcal{D}$. Thus,

$$\begin{aligned} \nabla'^2 \quad G_{\mathcal{D}}(\boldsymbol{r},\boldsymbol{r}') &= -\delta(\boldsymbol{r}-\boldsymbol{r}') \qquad \boldsymbol{r},\boldsymbol{r}' \in \mathcal{D} \\ G_{\mathcal{D}}(\boldsymbol{r},\boldsymbol{r}') &= 0, \qquad \boldsymbol{r}' \in \partial\mathcal{D} \end{aligned} \tag{2.6}$$

Since the choice of the domain $\mathcal{D}$ is arbitrary, we should choose it such that $G_{\mathcal{D}}(\boldsymbol{r},\boldsymbol{r}')$ has a known analytic form and is inexpensive to compute. In terms of this domain Green's function, the potential in Eq.(2.5) becomes

$$\Phi(\boldsymbol{r}) = \int_{\mathcal{D}} \rho(\boldsymbol{r}')G_{\mathcal{D}}(\boldsymbol{r},\boldsymbol{r}')d^3\boldsymbol{r}' + \int_{\partial\mathcal{D}} d^2\boldsymbol{r}' \cdot \nabla G_{\mathcal{D}}(\boldsymbol{r},\boldsymbol{r}')\Phi(\boldsymbol{r}') \tag{2.7}$$

The first integral is known exactly, and the second integral is very similar to that in Eq.(2.2); in fact if the gradient term is constant, then they are identical up to a constant factor. Hence the same WOS algorithm can evaluate this term, provided we generalize it to any arbitrary domain $\mathcal{D}$

and sample its surface $\partial\mathcal{D}$ not uniformly but according to $\nabla G_{\mathcal{D}}(\boldsymbol{r}, \boldsymbol{r}')$. We have thus generalized WOS to a "Walk On Domains" $\mathcal{D}_0, \mathcal{D}_1, \ldots$ instead of spheres. The iterative nature of Eq.(2.7) is inherent in the WOS algorithm. Accumulating contributions of $G_{\mathcal{D}}(\boldsymbol{r}_k, \boldsymbol{r}_{k+1})$ from each domain $\mathcal{D}_k$ along the walk and averaging over several such walks will provide an estimate of $\Phi(\boldsymbol{r})$. There is more to say about evaluating the first integral and we will devote a subsection to it. Discussion of dielectric boundaries will also be deferred to a separate section.

Thus the "'Walk On Spheres/Domains" is a general algorithm to solve the potential problem. For completeness we should also mention that the Green's function for the entire system defined over Ω is given by

$$G(\boldsymbol{r}, \boldsymbol{r}') = G_{\mathcal{D}}(\boldsymbol{r}, \boldsymbol{r}') + \int_{\mathcal{D}} d^2\boldsymbol{r}'' \cdot \nabla G_{\mathcal{D}}(\boldsymbol{r}, \boldsymbol{r}'') G(\boldsymbol{r}'', \boldsymbol{r}') \tag{2.8}$$

and our walk is implicitly constructing this exact Green's function for the problem.

2.3.1 Choice of Domain Shape

Though theoretically the domain shape can be arbitrary, in practice it is wise to choose a shape for which $G_{\mathcal{D}}(\boldsymbol{r}, \boldsymbol{r}')$ is known and inexpensive to compute, and $\nabla G_{\mathcal{D}}(\boldsymbol{r}, \boldsymbol{r}')$ is also easy and inexpensive to sample. If we restrict ourselves to spherical domains, the Green's function has a particularly simple form. For a sphere of radius d centered at $\boldsymbol{r}$,

$$G_{\mathcal{D}}(\boldsymbol{r}, \boldsymbol{r}') = \frac{1}{4\pi\varepsilon} \left(\frac{1}{|\boldsymbol{r}' - \boldsymbol{r}|} - \frac{1}{d} \right). \tag{2.9}$$

and $d^2\boldsymbol{r}' \cdot \nabla G_{\mathcal{D}}(\boldsymbol{r}, \boldsymbol{r}') = d^2 r$, i.e. the domain surface should be sampled uniformly, exactly as in WOS. Also we see that this captures the $1/r$ Coulomb interaction directly, but adds the corrections due to the boundary conditions. The problems regarding spherical domains have already been addressed. There are mainly the issues of slow convergence and dealing with planar boundaries.

We could have chosen some other shapes like cubes or rectangular parallelepipeds. This would have allowed us to sample planar surfaces exactly, and the walks would terminate much faster than that with the choice of spherical domains. Liu et al [46] have described a method of sampling the Green's function and its gradient for rectangular domains. The main idea is that the Green's function is expressed as a time integral over known one-dimensional Green's functions. Though the

one dimensional Green's functions are in the form of infinite sums, the authors show that we need to consider only a few terms. Nevertheless, the computation involved is not as simple as with the spherical domains.

The considerations for choosing one domain shape over the other are as follows. For any arbitrary geometry, using rectangular domains would not be advantageous since in general there will not be any considerable overlap of the domain surface and the external non-planar boundaries. In the completely general case therefore the spherical domains are an ideal choice. Moreover the calculations and sampling for the spherical domains are much simpler to understand and implement on a computer. If however the device has planar surfaces then walks employing rectangular domains will converge very rapidly. The main advantage of using spherical domains, as will be shown in section 2.6, is that the Green's function is a straightforward correction to the $1/r$ Coulombic interaction. This allows us to take care of the image terms like $G(\boldsymbol{r}, \boldsymbol{r})$ in a straightforward way; implementing this for any other domain shape will in general be very complicated.

2.3.2 Accounting for the Charge Density

The fixed random walk can easily take care of the charge density by accumulating contributions from each sampled grid point, as shown in section 2.1.1. To incorporate this into the WOS algorithm, we look back to Eq.(2.7) and discuss means of evaluating the first integral. Keeping in mind the nature of systems we will be dealing with, we note that there will be mainly two types of charge densities in the system, the QMC walker charge density and the density of the semi-classical charge distribution due to processes like doping.

Let us assume that each QMC walker $\boldsymbol{R}_m$ consists of N particles where the j-th particle has cöordinates $\boldsymbol{q}_j$ and charge Q_j. The walker charge density is simply given by

$$\rho_{\text{walker}}(\boldsymbol{r}) = \sum_{j=1}^{N} Q_j \delta(\boldsymbol{r} - \boldsymbol{q}_j).$$

The volume integral in Eq.(2.7) becomes

$$\int_{\mathcal{D}} \rho(\boldsymbol{r}') G_{\mathcal{D}}(\boldsymbol{r}, \boldsymbol{r}') d^3\boldsymbol{r}' = \sum_{j=1}^{j=N} Q_j \int_{\mathcal{D}} \delta(\boldsymbol{r}' - \boldsymbol{q}_j) G_{\mathcal{D}}(\boldsymbol{r}, \boldsymbol{r}') d^3\boldsymbol{r}' = \sum_{j=1}^{N} Q_j G_{\mathcal{D}}(\boldsymbol{r}, \boldsymbol{q}_j)$$

which is simply the sum of the domain Green's functions which we already know how to compute.

If the charge distribution $\rho(\boldsymbol{r})$ is a continuous function, then the algorithm becomes slightly more involved. Sampling a point $\boldsymbol{s}$ within the domain according to $G_{\mathcal{D}}(\boldsymbol{r}, \boldsymbol{r}')$ and accumulating the charge density $\rho(\boldsymbol{s})$ should give us an estimate of the integral. DeLaurentis [17] suggests the following approach.

Let us define $d(\boldsymbol{r})$ to be the minimum distance to the boundary $\partial\Omega$ from the point $\boldsymbol{r}$, i.e. the radius of the maximum sphere. In order to sample according to the Green's function $G_{\mathcal{D}}(\boldsymbol{r}, \boldsymbol{r}')$ given by Eq.(2.9) we need to compute the normalized probability density,

$$\omega(\boldsymbol{r}, \boldsymbol{r}') = \frac{G_{\mathcal{D}}(\boldsymbol{r}, \boldsymbol{r}')}{\int_0^d d^3\boldsymbol{r} G_{\mathcal{D}}(\boldsymbol{r}, \boldsymbol{r}')} = \frac{6}{d^2} G_{\mathcal{D}}(\boldsymbol{r}, \boldsymbol{r}')$$

and the density in spherical cöordinates centered at $\boldsymbol{r}$ and with $r = |\boldsymbol{r} - \boldsymbol{r}'|$ is

$$\omega(r) dr d\theta d\phi = \left[\frac{1}{4\pi} \frac{6}{d^2} \left(\frac{1}{r} - \frac{1}{d} \right) r^2 \sin\theta \right] dr d\theta d\phi \tag{2.10}$$

where we have taken $\varepsilon = 1$ for convenience, it is just a scaling factor and not germane to the problem at hand. So we sample a point $\boldsymbol{s}$ ($|\boldsymbol{s}| \leq d$), i.e. within the spherical domain according to this distribution; Appendix A shows the mathematical details of how this is done. Once we have sampled this point, then Eq.(2.7) for each domain of the walk becomes

$$\tilde{\Phi}(\boldsymbol{r}) = \sum_{j=1}^{N} Q_j G_{\mathcal{D}}(\boldsymbol{r}, \boldsymbol{q}_j) + \frac{d^2}{6} \rho(\boldsymbol{s}) + \int_{\partial\mathcal{D}} d^2\boldsymbol{r}' \cdot \nabla G(\boldsymbol{r}, \boldsymbol{r}') \Phi(\boldsymbol{r}')$$

So the algorithm is to get domain contributions of each particle of the walker, i.e. the individual domain Green's functions for the first sum in the above equation, then sample a point $\boldsymbol{s}$ and get the charge density contribution from there, and lastly to sample a point on the surface, construct the maximum sphere and repeat the process until the walk ends near the boundary.

2.4 Dielectric Boundaries

In the previous sections we assumed the dielectric constant ε to be homogeneous throughout the system. This allows us to choose a unit system in which we could set $\varepsilon = 1$. After all, it is

nothing but a scaling factor. However when the dielectric function is inhomogeneous and is position dependent, i.e. $\varepsilon \equiv \varepsilon(\boldsymbol{r})$ the algorithm becomes more complicated. In the completely general case where the dielectric function varies widely over the entire region, the fixed random walk can be modified to handle this case.

2.4.1 Fixed Random Walk

Consider Fig.(2.1), a two dimensional discretization of a device, but now consider that the dielectric function is continuously varying throughout the device $\varepsilon \equiv \varepsilon(\boldsymbol{r})$. In this case the finite difference representation of the Poisson's equation yields

$$\Phi(x,y) = \frac{1}{4}\frac{\ell^2}{\varepsilon(x,y)}\rho(x,y) + \frac{1}{4}\sum_i \frac{\varepsilon_i}{\varepsilon(x,y)}\Phi_i$$

A three dimensional discretization would replace the factor of 4 by 6. So in this case, instead of simply averaging over all the neighbors, we have to weight each neighbor according to the value of the dielectric function at that point. Hence, the probabilities of the walk are not equal, but

$$p_i = \varepsilon_i / \sum_i \varepsilon_i \tag{2.11}$$

where i is one of the neighboring points.

However most systems or devices do not have such a strong position dependence of the dielectric function, they are usually made of different materials, and the dielectric function is assumed to be constant throughout the material. Hence we do not need a method as general as described above, we can treat each material with uniform dielectric just as we described in the previous section, and the walk needs to be modified only at the interface of different materials to take care of the boundary conditions.

2.4.2 Floating Random Walk

The floating random walk can be easily adjusted to handle systems with piecewise constant dielectric function. The algorithm was first described by Royer [66], though several other authors [63, 36] have developed clever tricks to improve efficiency. Later, we develop our own algorithm to improve

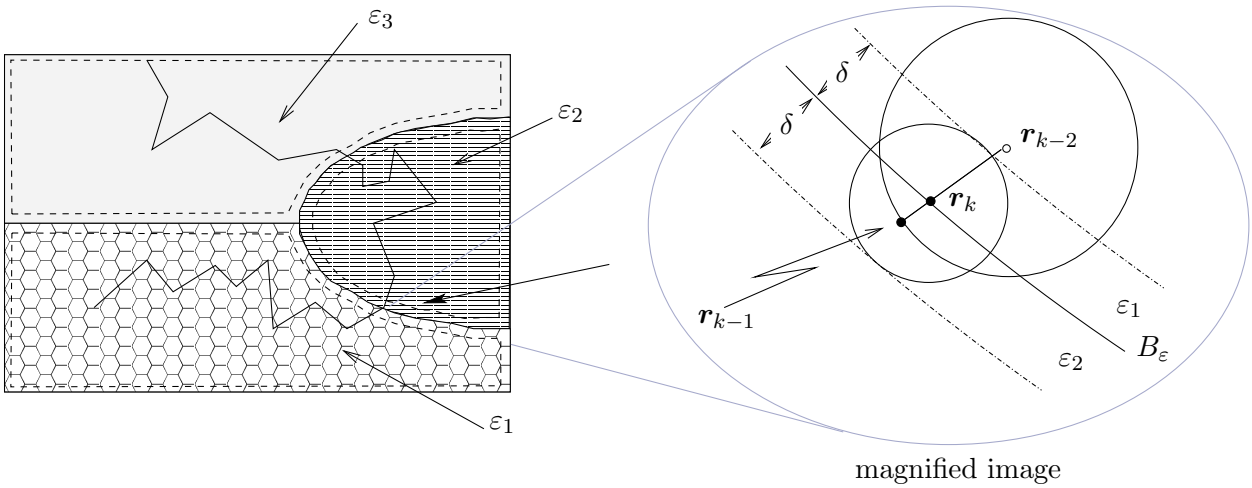

Figure 2.5: One sample path for a walk in a device with regions of different dielectric materials.

the efficiency of potential calculation in typical heterostructure device geometries.

Let the position at some point of the random walk be at the point $\boldsymbol{r}_{k-2}$, and the next position being $\boldsymbol{r}_{k-1}$ lying on the surface of the the spherical domain $\mathcal{D}_{k-2}$. Both the radius of the domain d_{k-2} and the way in which the position $\boldsymbol{r}_{k-1}$ is generated depend on the location of $\boldsymbol{r}_{k-2}$. When $\boldsymbol{r}_{k-2}$ is not on a dielectric boundary, $\boldsymbol{r}_{k-1}$ is sampled randomly and uniformly on $\mathcal{D}_{k-2}$. If however the sampled point $\boldsymbol{r}_{k-1}$ crosses the dielectric boundary B_ε, as in Fig.(2.5), it is relocated to $\boldsymbol{r}_k$ which is the intersection of the boundary B_ε and the straight line connecting $\boldsymbol{r}_{k-2}$ and $\boldsymbol{r}_{k-1}$.

The next domain $\mathcal{D}_k$ is constructed as follows:

1. First, $\boldsymbol{r}_k$ is located on a dielectric boundary. If this boundary is a plane (as in most heterostructure devices), d_k the domain radius is made equal to the shortest distance between $\boldsymbol{r}_k$ and the following surfaces: a) the external boundary $\partial\Omega$, b) dielectric interfaces other than the one $\boldsymbol{r}_k$ is located. When the dielectric interface on which $\boldsymbol{r}_k$ is located is curved as in Fig.(2.5), then $d_k = \delta$. If δ is small compared to the radius of curvature of the interfaces, this procedure ensures that the interface is essentially planar inside the domain $\mathcal{D}_k$. This will be shown to be a necessary condition in section 2.4.3.

2. When the point is in between the skin region of the external boundary $\partial\Omega$ then d_k is set equal to the skin width δ.

3. When $\boldsymbol{r}_k$ is located within Ω but not in the regions mentioned in 1. or 2. above, d_k is made

equal to the shortest distance between $\boldsymbol{r}_k$ and the external boundary $\partial\Omega$ or interfaces B_ε.

2.4.3 Transition at a Planar Interface

Once this domain $\mathcal{D}_k$ is constructed, centered on a point lying on the interface we need to sample a point $\boldsymbol{r}_{k+1}$ on its surface. Note that this domain is such that half the domain is in one dielectric medium, and the other half in another. Let us refer to these dielectric constants as ε_1 and ε_2 according to Fig.(2.5 b), i.e. the domain $\mathcal{D}_k$ is divided between $\mathcal{D}_{\varepsilon_1}$ and $\mathcal{D}_{\varepsilon_2}$ as in Fig.(2.4.3).

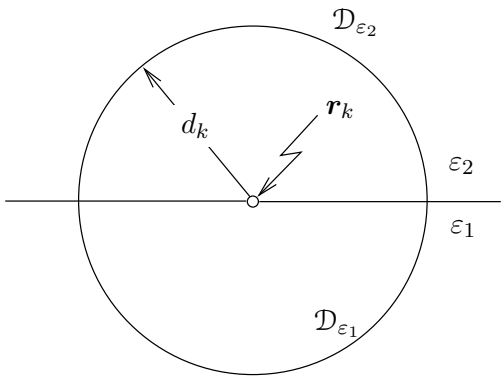

Figure 2.6: Boundary hopping

If the dielectric function was constant throughout the domain, the potential at $\boldsymbol{r}_k$ is a simple average over the spherical domain surface. However for the planar interface as described above, it will be shown in section 5.5 that the potential is given not by a simple but a weighted average,

$$\Phi(\boldsymbol{r}_k) = \frac{\varepsilon_1}{\varepsilon_1+\varepsilon_2}\left[\frac{1}{2\pi d_k^2}\int_{\partial\mathcal{D}_{\varepsilon_1}} d^2\boldsymbol{r}\cdot\hat{n}\Phi(\boldsymbol{r})\right] + \frac{\varepsilon_2}{\varepsilon_1+\varepsilon_2}\left[\frac{1}{2\pi d_k^2}\int_{\partial\mathcal{D}_{\varepsilon_2}} d^2\boldsymbol{r}\cdot\hat{n}\Phi(\boldsymbol{r})\right] \tag{2.12}$$

thus with probability $p_i = \varepsilon_i/\sum p_i$, we sample the surface $\partial\mathcal{D}_{\varepsilon_i}$ uniformly. This is the continuous version of Eq.(2.11). Hence, in this situation, we generate a uniform random number $\xi \in (0,1]$. If $\xi \leq p_1$, we sample $\partial\mathcal{D}_{\varepsilon_1}$ uniformly, otherwise we sample $\partial\mathcal{D}_{\varepsilon_1}$. So there is a finite probability of passing through to the other dielectric medium. After this the walk continues as before.

The efficiency of the method is dependent on the number of steps taken by the walk to reach the external boundary $\partial\Omega$. With several dielectric interfaces, and the requirements mentioned above, the number of steps in each walk is extended considerably, and the above method though elegant is not very efficient. We will improve the efficiency of the algorithm in a later section for a specific

class of geometries.

2.5 A Simple Estimation of the Error

So far we have discussed only the algorithm to estimate the potential at a point. Now we turn to another important issue of calculating a theoretical estimate for the error in such a calculation. If the walk is repeated an infinite number of times, then the estimate should be exact, however we are limited only to a finite number of such walks and this introduces an error in our estimate.

Instead of the completely general problem, we will discuss a very specific example. Consider the external boundary $\partial\Omega$ to be made of only two sections $\partial\Omega_1$ and $\partial\Omega_2$, with boundary potentials of V and 0 respectively. We generate n walks from $\boldsymbol{r}_0$ the point of interest.

The probability that of these n walks, m hit the $\partial\Omega_1$ surface is given by the binomial frequency function

$$B(m) = \frac{n!}{m!(n-m)!} p_1^m p_2^{(n-m)}$$

where $p_i \equiv p_i(\boldsymbol{r}_0, \partial\Omega_i)$ is the probability that a walk starting from $\boldsymbol{r}_0$ would end on the $\partial\Omega_i$ surface. In the limit of large n and $n-m$ this distribution can be approximated by the normal distribution

$$B(m) \simeq f(m) = \frac{1}{\sqrt{2\pi\sigma^2}} \exp\left[-\frac{1}{2}\left(\frac{m-\mu}{\sigma}\right)^2\right]$$

where mean $\mu = np_1$ and variance $\sigma^2 = np_ip_2$. Since the probabilities p_i-s are in general unknown, the variance is estimated from $\sigma \simeq s_m = \sqrt{np_{1c}p_{2c}}$, where $p_{1c} = m/n$ and $p_{2c} = 1 - m/n$. Replacing σ by the estimate s_m and multiplying m, μ and s_m by V/n we get

$$f(V_r(\boldsymbol{r}_0)) \simeq \frac{1}{\sqrt{2\pi s_m^2}} \exp\left[-\frac{1}{2}\left(\frac{V_r(\boldsymbol{r}_0) - V_e(\boldsymbol{r}_0)}{s_v}\right)^2\right]$$

where s_v is given by

$$s_v = \left[\frac{V_c(\boldsymbol{r}_0)(V - V_c(\boldsymbol{r}_0))}{n}\right]^{1/2}$$

and $V_e(\boldsymbol{r}_0)$ is the expected value, $V_c(\boldsymbol{r}_0)$ is the computed value and V_r is the random computed

value of the potential at $\boldsymbol{r}_0$. Now we can easily estimate bounds, for example

$$-1.96 s_v < V_r(\boldsymbol{r}_0) - V_e(\boldsymbol{r}_0) < +1.96 s_v,$$

Also note that s_v varies as $1/\sqrt{n}$.

2.6 Potential and Potential Energy

The total potential energy of the configuration is

$$\begin{aligned} V(\boldsymbol{R}_m) = \sum_{i=1}^{N} Q_i \left[\Phi_{\text{Gate}}(\boldsymbol{q}_i) + \frac{1}{2} \sum_{j \neq i} Q_j G(\boldsymbol{q}_i, \boldsymbol{q}_j) \right] \\ + \sum_{i=1}^{N} V_{\text{self}}(\boldsymbol{q}_i), \qquad \{\boldsymbol{q}_i\} \in \boldsymbol{R}_m. \end{aligned} \tag{2.13}$$

$V_{\text{self}}(\boldsymbol{q}_i)$ is the effect of the charges induced in the environment by the particle at $\boldsymbol{q}_i$ itself. This effect manifests itself in the Green's function for the particle $G(\boldsymbol{q}_i, \boldsymbol{q}_i)$ which is of course divergent due to the inherent Coulomb divergence of any charged particle. So,

$$V_{\text{self}}(\boldsymbol{q}_i) = \frac{Q_i^2}{2} \lim_{\boldsymbol{r} \to \boldsymbol{q}_i} \left[G(\boldsymbol{r}, \boldsymbol{q}_i) - \frac{1}{4\pi\varepsilon} \frac{1}{|\boldsymbol{r} - \boldsymbol{q}_i|} \right].$$

For the spherical domain, this simplifies beautifully; the $1/r$ divergence in the spherical domain Green's function Eq.(2.9) cancels with that in the self term above leaving a contribution of $-Q_i^2/(2d_0)$ from the first domain. The remainder is the contribution from each subsequent domain along the same walk. This simplification is one of the major reasons for preferring the spherically shaped domains over other shapes.

2.7 Improving Efficiency

Convergence properties of the WOS algorithm have been extensively studied by Muller [54] and de Laurentis [17]. For an N-particle system, each walk takes on average $n = \mathcal{O}(|\log \delta|)$ (see Fig.(2.2)) steps to converge. A separate walk has to be started from each particle at $\boldsymbol{q}_i$ $\forall i$ in the sum of

Eq.(2.13). An N-fold efficiency can be gained if the same walk can estimate the potential at points in the neighborhood of the origin of the walk. If the walkers $\{\boldsymbol{R}\}$ are all confined within a small region, then an algorithm by Pickles [60] to calculate electric fields, can be adapted for this purpose.

2.7.1 Interpolation using Off-centered Domains

In the previous section we generalized the Mean Value Theorem Eq.(2.2) (for spherical domains), to domains of arbitrary shapes by means of

$$\Phi(\boldsymbol{q}) = \int_{\partial\mathcal{D}} d^3\boldsymbol{r}' \cdot \boldsymbol{\nabla} G_{\mathcal{D}}(\boldsymbol{q}, \boldsymbol{r}')\Phi(\boldsymbol{r}').$$

For the sphere centered on the point $\boldsymbol{q}$ with $G_{\mathcal{D}}$ given by Eq.(2.9), this reduces to Eq.(2.2) which is uniform sampling over the domain surface. However, we could as well use an "off-centered" Green's function which would account for the potential not just at the domain center but at neighboring points as well. The basic idea is that the evaluation of the potential at some point $\boldsymbol{r}_0$ involves

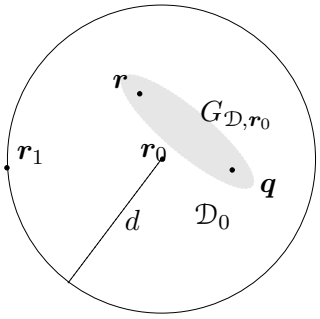

Figure 2.7: Sampling the interaction between points $\boldsymbol{q}$ and $\boldsymbol{r}$ inside the domain $\mathcal{D}_0$ centered at $\boldsymbol{r}_0$ is done by means of an off-centered Green's function.

integration of a Green's function $G(\boldsymbol{r}_0, \boldsymbol{r})$ over the second coördinate $\boldsymbol{r}$ which is any point in the integration volume $\mathcal{D}$. When the domain $\mathcal{D}$ is a sphere centered at $\boldsymbol{r}_0$, the Green's function simplifies $G_{\boldsymbol{r}_0}(\boldsymbol{r}_0, \boldsymbol{r}) \equiv G_{\boldsymbol{r}_0}(|\boldsymbol{r}_0 - \boldsymbol{r}|)$ as in Eq.(2.9). The subscript $\boldsymbol{r}_0$ indicated the domain center. However to evaluate the potential at some other point $\boldsymbol{q}$ using the same domain we need the Green's function $G_{\boldsymbol{r}_0}(\boldsymbol{q}, \boldsymbol{r})$, with the spherical domain $\mathcal{D}$ still centered on $\boldsymbol{r}_0$, and not $\boldsymbol{q}$. This approach will enable the simultaneous evaluation of the potential at several points $\{\boldsymbol{q}_i\}$ using walks starting with the same domain centered at $\boldsymbol{r}_0$.

So for a sphere of radius d and centered at $\boldsymbol{r}_0$, we need $G_{\mathcal{D},\boldsymbol{r}_0}(\boldsymbol{q}, \boldsymbol{r})$ between any two points $\boldsymbol{q}$

and $\boldsymbol{r}$ inside the sphere. This is easily obtained from the method of images [34],

$$G_{\mathcal{D},\boldsymbol{r}_0}(\boldsymbol{q},\boldsymbol{r}) = \frac{1}{4\pi\varepsilon}\left[\frac{1}{|\boldsymbol{q}-\boldsymbol{r}|} - \frac{d}{|\boldsymbol{r}-\boldsymbol{r}_0||\boldsymbol{q}-(d/r)^2\boldsymbol{r}|}\right].$$

So now the integral over the surface of the first domain involves the gradient of this Green's function Fig.(2.7)) and is no longer a constant as was the case before. A constant gradient implied a uniform sampling over the spherical surface, but even now we could sample the surface uniformly if the walk is weighted by a factor of $w_i = \nabla G_{\mathcal{D},\boldsymbol{r}_0}(\boldsymbol{q}_i,\boldsymbol{r}_1) = d(d^2-q_i^2)/|\boldsymbol{q}_i-\boldsymbol{r}_1|^3$ for each particle at $\boldsymbol{q}_i$.

So the modification needed to WOS is very simple. The first sphere is centered at some common point, say the centroid of the walker configuration. The point $\boldsymbol{r}_1$ is sampled uniformly on the domain surface, and the weight $w_i \equiv w(\boldsymbol{q}_i,\boldsymbol{r}_1)$ is computed for each particle. From then on, the walk continues using centered spheres of Eq.(2.9). The potential $\Phi(\boldsymbol{q}_i)$ sampled from this walk is obtained by weighting the walk by the prerecorded $w(\boldsymbol{q}_i,\boldsymbol{r}_1)$s. Thus the contribution of the applied potential, i.e. the $Q_i\Phi(\boldsymbol{q}_i)$ part of Eq.(2.13) becomes

$$\frac{1}{\mathcal{N}}\sum_{n=1}^{\mathcal{N}} Q_i w(\boldsymbol{q}_i,\boldsymbol{r}_1^{(n)})\Phi_{\rm app}(\boldsymbol{r}_n^\star).$$

However, if the particle position $\boldsymbol{q}_i$ happens to be far from the domain center $\boldsymbol{r}_0$, i.e. near the surface of the first domain, then the estimate of $\Phi(\boldsymbol{q}_i)$ is dominated by only a few walks with large weights and the noise in the estimate is magnified. A good rule of thumb is to choose the first sphere of radius d_0 such that $|\boldsymbol{q}_i-\boldsymbol{r}_0| \le d_0/2,\ \forall i$.

This method can be directly used for a fast and efficient estimation. Suppose we perform an initial calculation to generate $\mathcal{N}$ runs, where the n-th run samples the point $\boldsymbol{r}_1^{(n)}$ on the surface of the first domain, and the run ends on the device boundary at a point $\boldsymbol{r}_n^\star$. If we tabulate this information $\{\boldsymbol{r}_1^{(n)}, \Phi_{\rm app}(\boldsymbol{r}_n^\star)\}\ \forall\ n = 1,\ldots,\mathcal{N}$, then at any later time we can obtain a quick estimate of the potential at any point $\boldsymbol{q}_i$ by simply evaluating

$$\tilde{\Phi}(\boldsymbol{q}_i) = \frac{1}{\mathcal{N}'}\sum_{n}^{\mathcal{N}'} w(\boldsymbol{q}_i,\boldsymbol{r}_1^n)\Phi_{\rm app}(\boldsymbol{r}_n^\star), \quad (\mathcal{N}' \le \mathcal{N})$$

without the need for any more time consuming walks. The accuracy will of course depend on $\mathcal{N}'$.

Generating all our estimates from the same finite set of data can lead to undesired correlations, which can be reduced by simply limiting the number of estimates according to the size of the data used. A good rule of thumb is to obtain no more than $\mathcal{N}$ separate estimates (for e.g. $\tilde{\Phi}(\boldsymbol{q}_i),\ i = 1,\ldots,\mathcal{N}$) from a data of size $\mathcal{N}$.

Many further improvements are possible. As will be shown below, this approach (of using off-centered domains) can be slightly modified to be used as one of many variance reduction techniques which can be easily incorporated within the WOS scheme. However the effectiveness of each technique will depend on the system or rather on the various competing contributions to the potential. Here we present a general overview of some of these strategies. In section 2.9, we will discuss these approaches in light of a simple application. The contributions to the potential come mainly from the effect of the applied boundary voltages and interaction between the volume charges. The choice of noise reduction method will depend on which of these contributions dominate.

Consider for example, the approach described above of obtaining the potential at points neighboring the walk-origin. This can be used to reduce the variance in the contribution of the applied boundary potentials. Suppose we know the potential $\Phi(\boldsymbol{r}_c)$ exactly at some point $\boldsymbol{r}_c$ in the first domain (it could be the origin of the walk). Also assume that the error associated with a sampled potential $\langle\tilde{\Phi}\rangle$ is ϵ, i.e. if we perform a calculation $\langle\tilde{\Phi}(\boldsymbol{q}_i)\rangle$ with the walk starting at the point $\boldsymbol{q}_i$ in the neighborhood of $\boldsymbol{r}_c$, then the error is approximately ϵ. On the other hand, if we employ the technique using the off-centered spherical domains, and simply calculate the difference $\Delta\Phi_{ic} = \langle\tilde{\Phi}(\boldsymbol{q}_i) - \tilde{\Phi}(\boldsymbol{r}_c)\rangle$, using the weight $w_{ic} = w(\boldsymbol{q}_i) - w(\boldsymbol{r}_c)$, the error is approximately $\epsilon_{\rm oc} = \langle w(\boldsymbol{q}_i) - w(\boldsymbol{r}_c)\rangle\epsilon$. For points $\boldsymbol{q}_i$ in the vicinity of $\boldsymbol{r}_c$, this weight $\langle w_{ic}\rangle$ is much smaller than unity and hence $\epsilon_{\rm oc} \ll \epsilon$. This is simply a form of correlated sampling. Then we can easily obtain $\Phi(\boldsymbol{q}_i) = \Phi(\boldsymbol{r}_c) + \Delta\Phi_{ic}$.

Other standard variance reduction techniques may also be considered. Antithetic variates can be easily implemented by constructing pairs of walks; the walks in each pair will sample opposite points on the surface of the first domain. However, the drawback of the method is that this can be constructed only for the first domain, beyond this the walks will proceed independently. We find this to yield only a marginal improvement even when the potential profile is antisymmetric about the origin of the walk. In general this method will not be very effective for arbitrary potential profiles.

2.7.2 Importance Sampling

Importance sampling is another technique that can be considered when we have some a priori knowledge of the potential profile; we can preferentially sample the *important* regions of the device and this will reduce variance. The form of the importance function will depend on the device geometry and we will discuss a specific example in section 2.9. For now, we will simply demonstrate a zero variance principle, i.e. if we know the potential exactly, then the potential itself is the optimal importance function and WOS can recover the potential without any noise in the estimate. This by itself is an uninteresting result but the what is important to note (and will be demonstrated later) that the variance can be reduced arbitrarily if even an approximate importance function can be arbitrarily improved to approach the optimal form.

The WOS integral is of the form

$$\Phi(\boldsymbol{r}) = \int \nabla G_{\mathcal{D}}(\boldsymbol{r}, \boldsymbol{r}')\Phi(\boldsymbol{r}')d^2\boldsymbol{r}'$$

For the spherical domain, a choice of importance function $I(\boldsymbol{r})$ leads to

$$\Phi(\boldsymbol{r}) = \int \frac{\Phi(\boldsymbol{r}')}{\mathbb{N}I(\boldsymbol{r}')/I(\boldsymbol{r})}\left[\mathbb{N}\frac{I(\boldsymbol{r}')}{I(\boldsymbol{r})}\frac{\sin\theta d\theta}{2}\frac{d\phi}{2\pi}\right],$$

we sample according to the term within the square brackets, and carry a weight $I(\boldsymbol{r})/\mathbb{N}I(\boldsymbol{r}')$ for each domain. Here $\mathbb{N}$ is the normalization, and $\boldsymbol{r}$ is the center of the domain while $\boldsymbol{r}'$ is the next point in the walk sampled on the surface of that domain. As the walk proceeds $\boldsymbol{r}_0 \to \boldsymbol{r}_1 \ldots \boldsymbol{r}_m$, the accumulated weight becomes

$$\frac{1}{\mathbb{N}^{m-1}}\frac{I(\boldsymbol{r}_0)}{I(\boldsymbol{r}_1)}\frac{I(\boldsymbol{r}_1)}{I(\boldsymbol{r}_2)}\cdots\frac{I(\boldsymbol{r}_k)}{I(\boldsymbol{r}_{k+1})}\cdots\frac{I(\boldsymbol{r}_{m-1})}{I(\boldsymbol{r}_m)} = \frac{1}{\mathbb{N}^{m-1}}\frac{I(\boldsymbol{r}_0)}{I(\boldsymbol{r}_m)},$$

the walk reaches the boundary at $\boldsymbol{r}_m$ and picks up the potential $\Phi(\boldsymbol{r}_m)$, the accumulated term from the walk is $I(\boldsymbol{r}_0)\Phi(\boldsymbol{r}_m)/\mathbb{N}^{m-1}I(\boldsymbol{r}_m)$. If the importance function is chosen such that $I(\boldsymbol{r}) = \Phi(\boldsymbol{r})$, then it is seen from the Mean Value Theorem Eq.(2.2) that the importance function is normalized i.e. $\mathbb{N} = 1$, and the accumulated contribution from *each* walker is $\Phi(\boldsymbol{r}_0)$ leading to zero variance. If the importance function is not optimal, then the normalization needs to be carried along and the

zero variance principle doesn't hold any more.

2.8 Constructing the Maximum Sphere

A practical computational scheme for the WOS algorithm must provide some explicit means of constructing the random walks. A major difficulty arises in construction of the "maximum spheres", i.e. the determination of the domain radius which is also the step length $|\boldsymbol{r}_k - \boldsymbol{r}_{k+1}|$ of the walk. Theoretically this could be of any length. The domain does not necessarily need to be the maximum sphere, but the algorithm is most efficient when it is. Geometrically this reduces to the minimum distance from the domain center to the external surface $\partial\Omega$ also called the *nearest boundary face* (NBF). This estimation could become very expensive for arbitrarily complicated geometries. We could make a compromise by choosing a small step length which may not be the exact minimum distance to the external surface, but is guaranteed to limit the walk within the device. This might save time in computing the step length but would slow convergence. As the walk nears an external surface, the minimum distance to the boundary is dominated by that surface alone, and we could simply calculate this one number. But keeping track of when this happens could become tricky. In most of our calculations we have treated rectangular heterostructure devices where determining this distance has reduced to finding the minimum of six numbers, i.e. the distances from a point to the six surface planes. However in this section we discuss more general and powerful methods of dealing with geometries of far greater complexities.

We follow here the strategy discussed by Suresh et al [32]. Consider the region shown in Fig.(2.8), where the external boundary $\partial\Omega$ is a set of eight surfaces $\{\mathrm{A,B},\ldots,\mathrm{G}\}$. Determination of the potential at point P takes place by starting random walks from the point P of which two sample paths are shown. This statistical clustering is an inherent characteristic of the WOS sampling algorithm, and implies that in most trials only a small subset of the external surface $\partial\Omega$ will play a role in determining the NBF; one such subset is highlighted in the first figure of Fig.(2.8). Thus the minimum search of all the eight faces of $\partial\Omega$ is wasteful. Suresh et al suggests the division of the region into quasi-disjoint regions called *Vornoi cells*, each of which is associated with one or more faces of $\partial\Omega$. For example, the Cell A is associated with all points in Ω for which the nearest face is face A. Such a cell can be determined for example (as in this case) by constructing the

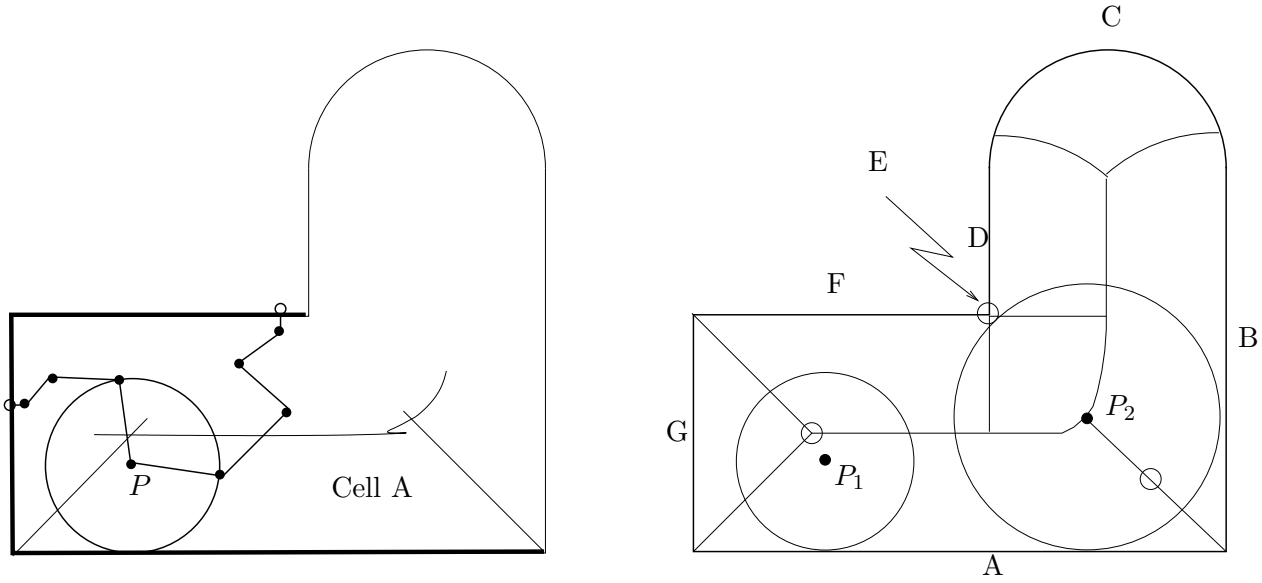

Figure 2.8: WOS in a complicated region divided into Vornoi cells.

bisectors between face A and various faces "close" to face A, thus marking off a region in Ω.

Consider the point P that lies in the Vornoi cell of A. By definition, it follows that the NBF of point P is face A. Now consider the first domain centered at P. This sphere intersects only a small number of Vornoi cells, and large portion of its surface must typically lie in the Vornoi cell of A. Thus the NBF of the point on the surface of the sphere at P is either face A with large probability, or one of those faces whose Vornoi cells are "adjacent" to the Vornoi cell of A.

Suresh et al continues this idea in the construction of "maximal graphs", which is a map of each cell onto all other cells that might be connected to it. For this consider Fig.(2.8). A domain at P_1 in A, connects A to G and F, and similarly one at P_2 also in A, connects it to B,D,E, and F. Thus by the construction of the maximal graph we can eliminate consideration of the C cell when the point is located in cell A, i.e. if a point belongs to cell A, it can not reach cell C in the next step. For details of the construction of Vornoi graphs consult the reference [32].

Construction of such graphs could also become expensive. Pickles [60] suggests construction of simple geometric rules to maintain a list of "relevant" boundary faces which are built from a library of simple standard shapes (like planes, spheres, cylinders etc.). With these simple standard shapes the distances $d(\boldsymbol{r}, \partial\Omega_i)$ between any point $\boldsymbol{r}$ and the individual surface $\partial\Omega_i$ are piecewise analytic functions which are easy to evaluate. For a given $\boldsymbol{r}_k$ the minimum distance is governed by simple

geometrical constraints

$$\begin{aligned} d(\boldsymbol{r}_k, \partial\Omega i) &\geq d(\boldsymbol{r}_{k-1}, \partial\Omega_i) - |\boldsymbol{r}_k - \boldsymbol{r}_{k-1}| \\ d(\boldsymbol{r}_k, \partial\Omega) &\leq d(\boldsymbol{r}_{k-1}, \partial\Omega) + |\boldsymbol{r}_k - \boldsymbol{r}_{k-1}| \\ d(\boldsymbol{r}_k, \partial\Omega) &\leq d(\boldsymbol{r}_k, \partial\Omega_i) \end{aligned}$$

and avoids the evaluation of every distance $d(\boldsymbol{r}_k, \partial\Omega_i \forall i$ at every step of the walk $\boldsymbol{r}_k$. More mathematically abstract but rigorous techniques can be found in the references of the cited articles, but we do not discuss them further.

2.9 Numerical Example

We demonstrate the techniques discussed in this chapter in the context of a simple problem, to calculate the potential profile within the plates of an infinite capacitor and compare it with the analytic solution which is simply a linear function.

The vertical plates of the capacitor are at a distance $z_L = \pm 1$, and the plates are at an applied voltage of $\Phi_{\text{app}} = \pm 1$ in arbitrary units. The calculations are compared in Fig.(2.9). The circles represent the calculations of the basic WOS, where the potential at any point $P(\boldsymbol{r})$ is obtained by generating runs starting from that point. Since all the runs are computationally similar, the corresponding errors are also similar, as seen from the large plateau in the inset. As we approach either side of the z-axis, i.e. near the plates of the capacitor, the errors are reduced considerably since the relative proximity of one plate increases its influence, hence reducing the variance. This is seen from the plateau falling off near the sides.

The triangles are estimates from runs all of which originate from the same point ($z_0 = 0$), and use the interpolation scheme described in section 2.7. Near the center this approach does just as well as the basic approach, as seen from the two curves in the inset coinciding. But further out near the plates the interpolation becomes worse as discussed earlier, since the entire estimate becomes dominated by only a few walks. The point is that while the basic WOS employed 10^3 runners for each of the 20 points in the plot, the interpolated method used 10^3 runners for the entire plot, hence it was about 20 times faster. In the calculations for the helium atom we expect even the

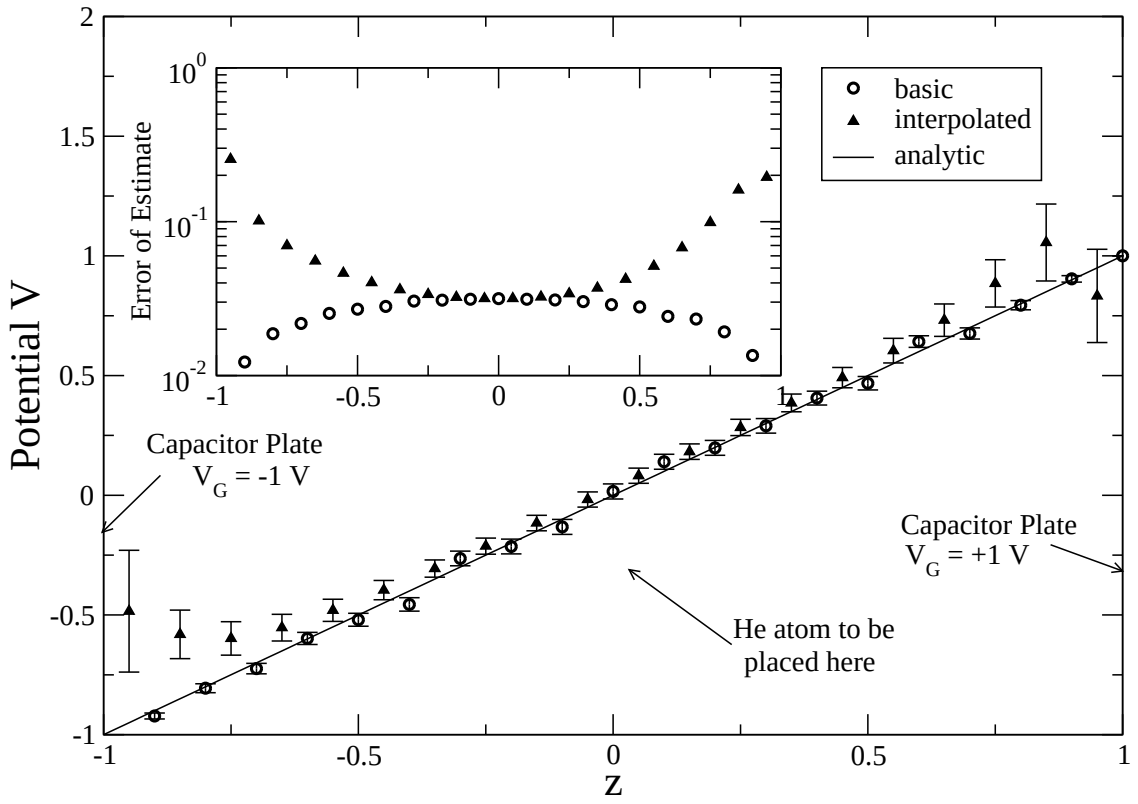

Figure 2.9: A comparison of different WOS algorithms to evaluate the potential between the plates of an infinite capacitor. The circles represent the basic WOS calculation where each run is started from the point where the potential is sought. The triangles are the interpolated estimates from runners starting from the center. The line represents the exact analytic form of the potential. The inset shows a comparison of the errors from the different schemes. Each estimate involved 10^3 runners.

polarized atom to remain well confined in the central region, and hence this approach will be three times faster (total number of particles being three) than the basic method.

We see a systematic error in the problem. Towards the edges the error in the calculations is large, but also the deviation from the theoretical value is not symmetric about the origin. This can be understood from the following argument. Even for a pair of points placed symmetrically about the origin, the symmetry is broken as soon as we sample $\boldsymbol{r}_1$, a point on the first domain surface. However uniform sampling over the sphere eliminates this bias for points close to the center. However for points far from the center the estimate is dominated by a few weights and hence the bias is not removed. Also note that since all the points are calculated using the same set of runs, these values and their error-bars are correlated. This is why we do not use this method to compute potential at points far from the center.

We also implemented the other methods mentioned earlier, namely that of using antithetic variates and that of using a reference value with the correlated sampling. As expected antithetic variates did not show significant improvement. Also as expected, the use of correlated sampling using the reference value was greatly effective in speeding up the calculation about three times (the number of particles). This also holds considerable promise for more complicated geometries.

2.9.1 Importance Sampling

Importance sampling can be illustrated for this example of an infinite capacitor. As shown in section , the optimal importance function is the potential itself. Since the external potential in a capacitor is simply $\Phi(\boldsymbol{r}) = z$, this can be implemented to illustrate the construction of such functions. This can also be derived more graphically, by noting that what we want is an importance function that leads to sampling regions of the spheres preferentially in the z direction so that the walks are directed towards the capacitor plates and hence end quickly.

The actual algorithm employing this importance function is simple to describe. Consider the k-th domain $\mathcal{D}_k$ centered at $\boldsymbol{r}_k(x_k, y_k, z_k)$ and radius d_k, and $\boldsymbol{r}_{k+1}$ is the next point in the walk sampled on $\partial\mathcal{D}_k$ the domain surface. So the optimal importance function is

$$\frac{I(\boldsymbol{r}_{k+1})}{I(\boldsymbol{r}_k)} = \frac{\Phi(\boldsymbol{r}_{k+1})}{\Phi(\boldsymbol{r}_k)} = \frac{z_{k+1}}{z_k} = 1 + \frac{d_k}{z_k}\cos\theta_{k+1}$$

where θ_{k+1} is the angle between the $z = 0$ plane and the line joining $\boldsymbol{r}_k$ and $\boldsymbol{r}_{k+1}$. The sampling just depends on the cöordinate of the point we are about to sample $\boldsymbol{r}_{k+1}$, the cöordinates of the present point $\boldsymbol{r}_k$ are already known. Note that the optimal importance function weighted kernel is normalized.

We implement this algorithm on the computer and obtain zero variance as expected. One point to note is that the variance is limited to a small non-zero number due to the finiteness of the skin depth δ which can be made arbitrarily small. A better approach is simply to switch the shape of the domain near the boundary, or easier still, to discretize the region near the boundary into a grid, and a discrete equivalent of WOS will exactly converge on the boundary and hence yield a zero variance.

Next we consider a small perturbation to the optimal importance function, $I(z) = z + \epsilon z^2$,

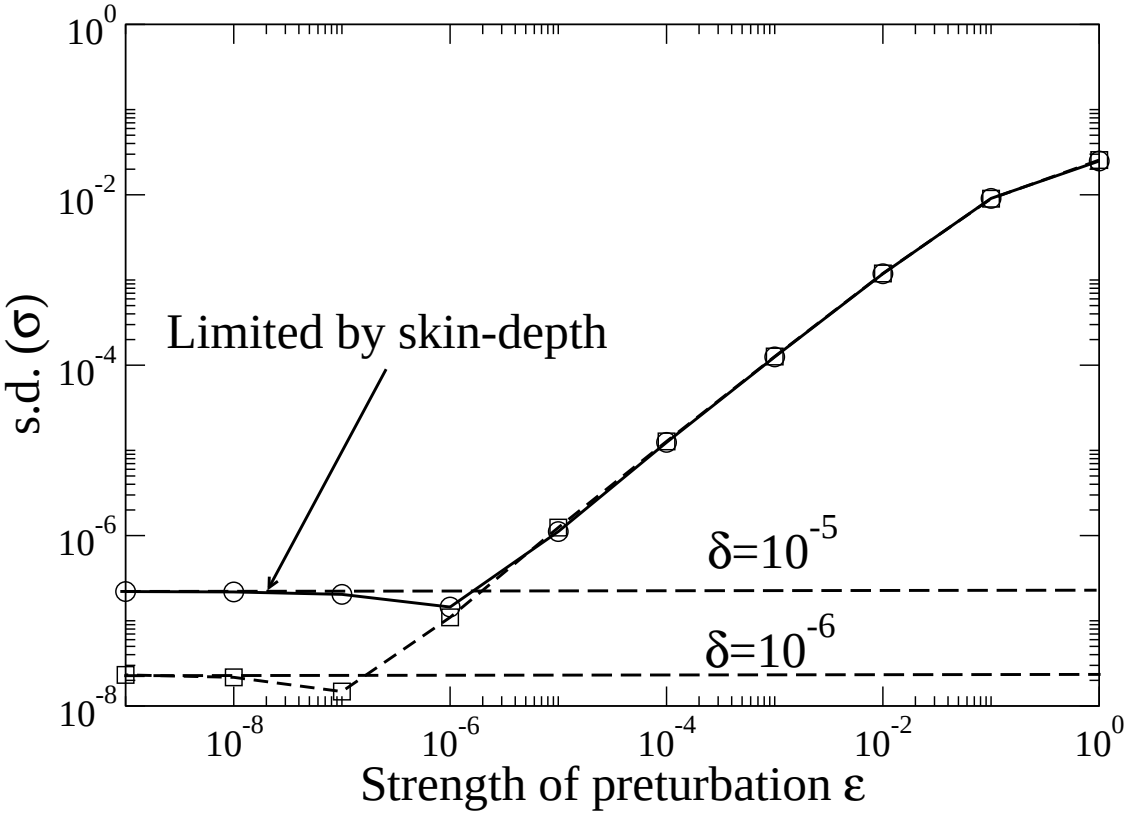

Figure 2.10: As the non-optimal importance function approaches the optimal form, variance is reduced. For an algorithm using only spherical domains the variance approaches a limiting value due to the finite size of the skin-depth δ. Discretizing near the boundary will eliminate this limit.

($\epsilon \ll 1$)i.e. we mix in a small quadratic term.

$$\frac{I(\boldsymbol{r}_{k+1})}{I(\boldsymbol{r}_k)} = \frac{z_{k+1} + \epsilon z_{k+1}^2}{z_k + \epsilon z_k^2}$$

This leads to an importance function quadratic in $\cos\theta_{k+1}$. The non-optimal importance function weighted kernel however is not normalized and we have to carry that in the weight. In Fig.(2.10) we show the result of the calculation. We plot the result with two values of skin depth δ and show that the error can indeed be arbitrarily reduced by reducing δ.

This generalizes to problems with more complicated geometries in a straightforward way. The optimal importance function is the potential itself, and for that one, the normalization of the importance-weighted kernel is unity. Hence for the general problem, one possibility is to utilize an approximate potential as the importance function. This approximate solution could be obtained in any number of ways including a finite element solution of the Poisson problem on a discretized grid using an approximate electron density. The solution, its gradient and Laplacian could be tabulated on the same mesh to generate a non-uniform distribution over a domain. To obtain the correct potential at the domain center, one would need to evaluate the approximate normalization over the domain surface and sample accordingly. Thus importance sampling would greatly improve the efficiency of the algorithm.

Chapter 3

Quantum Monte Carlo

In this chapter we discuss the two most common ground state quantum Monte Carlo (QMC) methods, namely variational Monte Carlo (VMC) and diffusion Monte Carlo (DMC). While discussing each of these methods we will also describe how by using a stochastic Poisson solver within the QMC approach we will be able to account for the correct electronic interaction. Note that we have two different samplings or "walks". The sampling to solve Schrödinger's equation will be carried out by fictitious particles which we will refer to by the standard name "walkers" described before. The walks needed to solve the classical potential problem will employ similar fictitious particles, but we will refer to them as "runners" to distinguish them from the walkers. In literature [75], they have also been referred to as "Poissonons". We call them runners since they can perform several walks during a single step of the walkers.

3.1 Variational Monte Carlo

The variational approach posits a functional form of the trial wave-function $\Psi_T(\boldsymbol{\alpha})$ which depends on a set of variational parameters $\{\boldsymbol{\alpha}\}$ [28, 23]. Minimization of the energy, (or variance or a mixture of both) with respect to the set $\{\boldsymbol{\alpha}\}$, by methods like correlated sampling [69, 22] gives the variational estimate of the energy.

$$\min_{\{\boldsymbol{\alpha}\}} \langle \Psi_T(\boldsymbol{\alpha}) | \mathcal{H} | \Psi_T(\boldsymbol{\alpha}) \rangle = E_{\mathrm{VMC}},$$

where $\mathcal{H} = -\frac{1}{2}\nabla^2 + V$ is the Hamiltonian in a.u. The minimization aside, $E = \langle \Psi_T | \mathcal{H} | \Psi_T \rangle$ (dependence on $\boldsymbol{\alpha}$ dropped for convenience) is simply a multi-dimensional integral which is performed

by the Monte Carlo. The estimator for this integral is called the "local energy"

$$E_L(\boldsymbol{R}) = \frac{\mathcal{H}\Psi_T(\boldsymbol{R})}{\Psi_T(\boldsymbol{R})} = -\frac{1}{2}\frac{\nabla^2\Psi_T(\boldsymbol{R})}{\Psi_T(\boldsymbol{R})} + V(\boldsymbol{R}). \tag{3.1}$$

The trial wave-function Ψ_T has to be a reasonably good approximation for the true ground-state wave-function. This could be produced from other approximate calculations like density functional theory (DFT) or could be analytic functions posited from theoretical considerations. It only needs to satisfy some basic conditions; both Ψ_T and $\nabla\Psi_T$ must be continuous wherever the potential is finite, and the integrals $\langle\Psi_T|\Psi_T\rangle$ and $\langle\Psi_T|\mathcal{H}|\Psi_T\rangle$ should exist. To keep the variance of the energy finite, we also need $\langle\Psi_T|\mathcal{H}^2|\Psi_T\rangle$ to exist. The variational principle establishes E_{VMC} as a rigorous upper bound on the exact ground-state energy E_0.

$$E_{\mathrm{VMC}} \geq E_0$$

A set of randomly distributed configurations $\{\boldsymbol{R}\}$ called walkers, are sampled according to the Metropolis algorithm [51, 39], to generate the distribution Ψ_T^2, i.e. $\mathbb{P}(\boldsymbol{R}_m) = \Psi_T^2$, where $\mathbb{P}$ is the probability distribution function (unnormalized). It is important to note here that this sampling *does not* involve a knowledge of the potential profile $V(\boldsymbol{r}, \boldsymbol{R}_m)$ at the point $\boldsymbol{r}$ due to the walker configuration $\boldsymbol{R}_m$. If M configurations are generated, then (after equilibration), for each of these configurations the local energy $E_L(\boldsymbol{R})$ is evaluated and the average energy is accumulated

$$E_{\mathrm{VMC}} \approx \frac{1}{M}\sum_{m=1}^{M} E_L(\boldsymbol{R}).$$

The trial moves are usually sampled from a Gaussian centered on the current position of the walker, the variance of the Gaussian being chosen such that average acceptance probability is roughly 50% or such that the diffusion constant of the random walk is maximized.

We are mainly interested in how this method can use a potential obtained by another independent sampling (and hence has some noise associated with it). To this end,

$$\langle V\rangle_{\mathrm{VMC}} = \int V(\boldsymbol{R})\Psi_T^2(\boldsymbol{R})d^{3N}\boldsymbol{R} \approx \frac{1}{M}\sum_{m=1}^{M} V(\boldsymbol{R}_m), \tag{3.2}$$

is an estimate of the potential energy of the state Ψ_T. Here $V(\boldsymbol{R}_m)$ is the exact potential energy of the walker $\boldsymbol{R}_m$ distributed according to Ψ_T^2. However even if we use a potential $\tilde{V}(\boldsymbol{R}_m)$ which is stochastic,

$$\langle V(\boldsymbol{R}_m)\rangle_{\mathrm{VMC}} = \langle \tilde{V}(\boldsymbol{R}_m)\rangle_{\mathrm{WOS}} \tag{3.3}$$

This is seen from the following. The stochastic potential can be expressed as

$$\tilde{V}(\boldsymbol{R}_m) = V(\boldsymbol{R}_m) + \Delta(\boldsymbol{R}_m),$$

where in the limit of large samples, the error $\Delta(\boldsymbol{R}_m)$ is normally distributed with mean zero. Hence $\langle \Delta(\boldsymbol{R}_m)\rangle$ is,

$$\lim_{M\to\infty} \frac{1}{M}\sum_{m=1}^{M} \Delta(\boldsymbol{R}_m) = \int d\boldsymbol{r}\mathbb{P}(\boldsymbol{R}_m)\left[\int \Delta\mathbb{P}(\Delta)d\Delta\right] = 0, \tag{3.4}$$

simply from the zero mean property of the error Δ. Thus the variational Monte Carloalgorithm can simply use the stochastic potential $\tilde{V}(\boldsymbol{R}_m)$ without any other modifications. The primary requirement for variational Monte Carloto work is that the distribution $\mathbb{P}(\Delta)$ have zero mean.

Consider a simple system with a known potential profile $V(\boldsymbol{r})$. Suppose to calculate the expectation of the potential energy corresponding to some given state Ψ_T (using variational Monte Carlo) with a target error of δV, we need N_w walkers. We can perform the same calculation using the stochastic potential instead of the known form, and using N_r runners (as described at the beginning of this section) for each walker, a total of $N_w N_r$ samples. Numerical experiments show that the the calculation is optimal when $N_r = 1$ and N_w is chosen such that an independent stochastic calculation of the potential $\Phi(\boldsymbol{P})$ at some point $\boldsymbol{P}$ using N_w runners yield an error $\delta\Phi \sim \mathcal{O}(\delta V)$. This is because while on one hand maximizing the number of walkers allow the algorithm to maximize the sampling of the phase space, on the other hand variational Monte Carlois insensitive to the accuracy of the potential sampled (as long as there are enough samples). So it is optimal to sample $\tilde{V}(\boldsymbol{R})$ for more configurations using more walkers, than increasing the accuracy of each estimate.

Optimization of the trial wave-function Ψ_T can easily be carried out by correlated sampling as usual, except that WOS can optimize only the variational energy and not the variance of the energy. This is because of the simple fact that the variance calculated using the stochastic potential would be $\langle \tilde{V}^2\rangle$ while what we need to compute is $\langle \tilde{V}\rangle^2$. This is a part of the general idea that only linear

functions can be handled using the stochastically obtained potential. One important distinction from usual computer algorithms needs to be emphasized. During the initial variational Monte Carlorun to generate the configurations, programs record the walker configurations, but usually not the corresponding local potential energies $V(\boldsymbol{R}_m)$ (the potential part of the local energy which depends on the wave-function only through the walker distribution). When the optimizer modifies the parameters $\boldsymbol{\alpha}$, changing the trial wave-function $\Psi_T(\boldsymbol{\alpha})$, the corresponding local Kinetic energy $-\frac{1}{2}\nabla^2\Psi_T/\Psi_T$ also changes. And the local energy of the walker is calculated anew because this saves storage and a known analytic potential is usually not too expensive to recompute.

However, recomputing the stochastic potential would in general produce a different estimate than before, i.e. $\tilde{V}(\boldsymbol{R}_m)$ will be different each time we recompute it. This will introduce an error which will not cancel on averaging, and hence destroy the optimization. This is easily remedied by simply recording the estimate of the local potential energy $\tilde{V}(\boldsymbol{R}_m)$ while recording the configurations $\{\boldsymbol{R}\}$. This will eliminate the overhead of recomputing the potential which can be expensive, the cost being a marginal increase in storage. Using the same local potential for a given configuration at every iteration of the optimization process we ensure that we minimize the correct estimate of the local energy.

3.2 Diffusion Monte Carlo

The stochastic potential approach is particularly compatible with variational Monte Carlo because VMC is linear in energy, and thus able to take advantage of Eq.(3.3). Exact Green's function Monte Carlo methods are also linear in energy and would be able to take advantage of this approach. However, diffusion Monte Carlo is not an exact Green's function method because of the short time approximation which simulates the Green's function by diffusion and branching processes. This makes the use of WOS with DMC not as straightforward as with VMC.

To see why this is the case, we review the basic ideas of the DMC algorithm. For practical details regarding implementation, see reviews or books like [23, 68, 28]. We follow the description of [23]. The Schrödinger's equation in imaginary time

$$-\partial_t\psi(\boldsymbol{R},t) = (\mathcal{H} - E_T)\psi(\boldsymbol{R},t)$$

can be transformed into an integral equation of the form

$$f(\boldsymbol{R}, t+\tau) = \int G(\boldsymbol{R}, \boldsymbol{R}'; \tau) f(\boldsymbol{R}', t) d\boldsymbol{R}', \tag{3.5}$$

where $f(\boldsymbol{R}, t) = \psi(\boldsymbol{R}, t)\Psi_T(\boldsymbol{R}, t)$ is a product of a known "trial" or "guiding" function Ψ_T and the eigenfunction ψ. E_T is an energy offset and $G(\boldsymbol{R}, \boldsymbol{R}'; \tau)$ is the Green's function or propagator. The integral equation is solved iteratively by starting with an initial distribution $f_{\text{init}} = \psi_{\text{init}}\Psi_T$ or rather a set of walkers distributed according to f_{init}. Repeated application of the Green's function to this state projects out the lowest energy state not orthogonal to ψ_{init}.

3.2.1 The Green's function Propagator

We first investigate the effect on the function ψ and then consider the modifications due to importance sampling on the function $f = \psi\Psi_T$. The essence of the algorithm is in calculation of this Green's function $G(\boldsymbol{R}, \boldsymbol{R}'; \tau)$,

$$G(\boldsymbol{R}, \boldsymbol{R}'; \tau) = \langle \boldsymbol{R}| \exp\left[-\tau(\mathcal{H} - E_T)\right] |\boldsymbol{R}'\rangle$$

which obeys the same equation as the wave-function

$$-\partial_t G(\boldsymbol{R}, \boldsymbol{R}'; \tau) = [\mathcal{H}(\boldsymbol{R}) - E_T] G(\boldsymbol{R}, \boldsymbol{R}'; \tau)$$

with the initial condition $G(\boldsymbol{R}, \boldsymbol{R}'; 0) = \delta(\boldsymbol{R} - \boldsymbol{R}')$. Using the spectral decomposition

$$\exp\left[-\tau\mathcal{H}\right] = \sum_i |\phi_i\rangle \exp\left[-\tau E_i\right] \langle\phi_i|,$$

we can express the Green's function as

$$G(\boldsymbol{R}, \boldsymbol{R}'; \tau) = \sum_i \phi_i(\boldsymbol{R}) \exp\left[-\tau(E_i - E_T)\right] \phi_i^\star(\boldsymbol{R}'),$$

where $\{\phi_i\}$ and $\{E_i\}$ denote the complete sets of eigenfunctions and eigenvalues of $\mathcal{H}$, respectively. It is straightforward to see that as $\tau \longrightarrow \infty$ the operator $\exp\left[-\tau(\mathcal{H} - E_T\right]$ projects out the lowest

eigenstate $|\phi_0\rangle$ that has nonzero overlap with the chosen $\psi_{\rm init}$ when the Green's function is applied to $\psi_{\rm init}$.

$$\begin{aligned}\lim_{\tau\longrightarrow\infty}\langle \boldsymbol{R}|\exp\left[-\tau(\mathcal{H}-E_T)\right]|\psi_{\rm init}\rangle &= \lim_{\tau\longrightarrow\infty}\int G(\boldsymbol{R},\boldsymbol{R}';\tau)\psi_{\rm init}(\boldsymbol{R}')d\boldsymbol{R}' \\ &= \lim_{\tau\longrightarrow\infty}\sum_i \phi_i(\boldsymbol{R})\exp\left[-\tau(E_i-E_T)\right]\langle\phi_i|\psi_{\rm init}\rangle \\ &= \lim_{\tau\longrightarrow\infty}\phi_0(\boldsymbol{R})\exp\left[-\tau(E_i-E_T)\right]\langle\phi_0|\psi_{\rm init}\rangle\end{aligned}$$

By adjusting E_T to equal E_0, we can make the exponential factor constant, while the higher states are all exponentially damped because their energies are higher than E_0. This fundamental property is the basis of the diffusion Monte Carlo method.

To discern the form of the Green's function, we note that without the potential term, the Hamiltonian is simply the Laplacian. This describes a diffusion process in $3N$-dimensional space (for N particles) for which the Green's function is of the form

$$G_{\rm diff}(\boldsymbol{R},\boldsymbol{R}';\tau)=\frac{1}{(2\pi\tau)^{3N/2}}\exp\left[-\frac{1}{2}\frac{|\boldsymbol{R}-\boldsymbol{R}'|^2}{\tau}\right]$$

It is easy to see that this Gaussian form tends to $\delta(\boldsymbol{R}-\boldsymbol{R}')$ as $\tau\longrightarrow 0$. This describes the diffusion of Brownian particles (walkers) in space and time, and thus we represent the distribution function $\psi(\boldsymbol{R},t)$ by a set of discrete Brownian sampling points or random walkers:

$$\psi(\boldsymbol{R},t)\rightarrow\{\boldsymbol{R}_m\}\equiv\sum_m\delta(\boldsymbol{R}-\boldsymbol{R}_m)$$

The Green's function $G_{\rm diff}$ can be interpreted as a transition probability density for the evolution of the walkers. Hence we have a set of Gaussians each with a variance of $3N\tau$. The procedure involves sampling each Gaussian by a new delta function the defines the new evolved position of the walker.

Now if we consider the potential part, without the kinetic term we see that it is simply a rate equation. The full Hamiltonian with the kinetic and potential together does not offer an explicit solution in general and we have make approximations. An approximation of the Green's function can be obtained using the Trotter-Suzuki formula for the exponential of a sum of operators A and

B:

$$\exp[-\tau(A+B)] = \exp[-\tau B/2]\exp[-\tau A]\exp[-\tau B/2] + \mathcal{O}(\tau^3)$$

If we write $\mathcal{H} = T + V$ where T is the full N-particle kinetic energy operator and V is the total potential energy, application of the Trotter-Suzuki formula with $A = T$ and $B = V - E_T$ gives

$$\begin{aligned} G(\boldsymbol{r}, \boldsymbol{r}'; \tau) = \langle \boldsymbol{R}| \exp[-\tau(T + V - E_T)]|\boldsymbol{R}'\rangle &\approx e^{-\tau[V(\boldsymbol{R})-E_T]/2}\langle \boldsymbol{R}| \exp[-\tau T]|\boldsymbol{R}'\rangle \times e^{-\tau[V(\boldsymbol{R})-E_T]/2} \\ &= \exp[-\tau(V(\boldsymbol{R}) + V(\boldsymbol{R}') - 2E_T)/2] \times G_{\text{diff}}(\boldsymbol{R}, \boldsymbol{R}'; \tau) \end{aligned}$$

with the error proportional to τ^3. Importance sampling introduces a trial wave-function Ψ_T, and this modifies Schrödinger's equation to

$$-\partial_t f(\boldsymbol{R}, t) = -\frac{1}{2}\nabla^2 f(\boldsymbol{R}, t) + \nabla \cdot [\boldsymbol{v}_D(\boldsymbol{R}) f(\boldsymbol{R}, t)] + [E_L(\boldsymbol{R}) - E_T] f(\boldsymbol{R}, t),$$

where ∇ is the $3N$-dimensional gradient operator, $\boldsymbol{v}_D(\boldsymbol{R})$ is the $3N$-dimensional *drift velocity* defined by

$$\boldsymbol{v}_D(\boldsymbol{R}) = \nabla \log|\Psi_T(\boldsymbol{R})| = \nabla\Psi_T(\boldsymbol{R})/\Psi_T(R)$$

and

$$E_L(\boldsymbol{R}) = \frac{\mathcal{H}\Psi_T(\boldsymbol{R})}{\Psi_T(\boldsymbol{R})}$$

is the local energy as defined for the VMC simulation. If E_L and E'_L are the local energies at points $\boldsymbol{R}$ and $\boldsymbol{R}'$ respectively, then within DMC the Green's function is approximated by

$$G(\boldsymbol{R}, \boldsymbol{R}'; \tau) \approx G_{\text{diff}}(\boldsymbol{R}, \boldsymbol{R}'; \tau) G_B(E_L, E'_L; \tau), \tag{3.6}$$

where

$$G_{\text{diff}}(\boldsymbol{R}, \boldsymbol{R}'; \tau) = \frac{1}{(2\pi\tau)^{3N/2}} \exp\left[-\frac{(\boldsymbol{R} - \boldsymbol{R}' - \tau\boldsymbol{v}(\boldsymbol{R}'))^2}{2\tau}\right],$$

and

$$G_B(E_L, E'_L; \tau) = \exp[-(E_L(\boldsymbol{R}) + E_L(\boldsymbol{R}') - 2E_T)\tau/2]. \tag{3.7}$$

G_{diff} is the Green's function for a diffusion process, and G_B is a weight factor. This approximation

holds for small time step τ.

Importance sampling has several consequences. Firstly, in the regions where Ψ_T is large the density of walkers is enhanced and vice versa. This is because the drift velocity $\boldsymbol{v}_D(\boldsymbol{R})$ carries the walkers along in the direction of increasing $|\Psi_T|$. Secondly, the exponent now contains the local energy instead of the potential, and this is crucial because for a good trial function the local energy is close to the ground-state energy eigenvalue and roughly constant. This stabilizes the walker population as we will discuss next.

3.2.2 The Branching Algorithm

The factor G_B in Eq.(3.7) acts as a time-dependent renormalization (reweighting) of the diffusion Green's function. This change of normalization can be incorporated into the process of walker evolution in various ways. The simplest possibility is to assign each walker a weight and accumulate the product of weights during the propagation of the walker. However, this is not an efficient approach, since the weights of the walkers rapidly become very different, and, in the long time limit, a few walkers dominate exponentially over the rest.

For improved stability and convergence most algorithms implement the weight factor G_B Eq.(3.7) by a "branching" or "birth/death" process in which the weight of a walker configuration is reflected by the proliferation or decay in the number density of that configuration. Let $n_B = G_B$ denote the number of walkers that survive to the next step of the evolution. In the simplest form the procedure is as follows:

1. If $n_B < 1$ the walker continues its evolution with probability n_B.

2. If $n_B \geq 1$ the walker not only continues its evolution, but another identical walker with the same configuration is created with probability $n_B - 1$.

Both these possibilities are incorporated in an algorithm in which $n_B = \text{int}[G_B + \xi]$ copies of the walker survive to the next step [64]. Here ξ is a random number drawn uniformly in the range $(0, 1]$. Thus in the regions of high potential energy G_B is small and the walkers disappear, while in the regions of low potential energy G_B is large and the walkers proliferate. The branching algorithm therefore transforms the weight accumulation in the low-energy regions into an increase in the density of the walkers there.

This is a marked difference from the VMC algorithm since here the number of walkers and hence the walk itself depends on our estimate of the potential. If we sample the potential very crudely, then the estimate could be much larger or smaller than the actual potential, this would lead to a grossly incorrect branching. The consequences could be severe, relevant configurations could be killed due to low estimates of the potential, while marginal configurations could proliferate. The effect of such a calculation would in general be unpredictable and this problem needs to addressed and solved before we can use the stochastic potential to perform DMC.

The energy offset E_T, which determines the overall asymptotic renormalization, is used to control the total population of walkers. During the propagation E_T is occasionally adjusted so that the overall number of walkers fluctuates around a desired mean value.

3.2.3 Branching with Stochastic Potential

The local energy as defined in Eq.(3.1) is the sum of kinetic and potential terms. But all that is germane to the following discussion is contained in the simplest unsymmetrized form of the weight G_B. Thus

$$\mathbb{G}_B(V,\tau) = \exp\left[-V\tau\right]$$

which depends only on the potential energy $V(\boldsymbol{R})$, is enough to illustrate all the issues of using a stochastic potential with DMC. $G_B(E_L)$ is simply $\mathbb{G}_B(V)$ with a factor which is independent of the potential and hence not relevant to the ensuing discussion. These considerations greatly simplify the notation. However in the numerical experiments in section 4.3 we use the importance sampled DMC with the Green's function given by Eqs.(3.6) and (3.7).

Sampling with a stochastic potential has serious implications for the branching. Unlike the situation in VMC the effect here is nonlinear (exponential) and hence a simple averaging will not get rid of the noise in the potential.. If we branch using a stochastically obtained potential $\tilde{V}$, then in effect we will be branching on average according to $\langle\exp[-\tilde{V}\tau]\rangle$. This is however not equal to $\exp[-\langle\tilde{V}\rangle\tau]$ (i.e. $\exp[-\langle V\rangle\tau]$ since $\langle\tilde{V}\rangle = V$) which is the branching we need. But nevertheless,

$$\langle\exp[-\tilde{V}\tau]\rangle = \exp[-\langle V\rangle\tau] + \mathcal{O}(\tau^2), \tag{3.8}$$

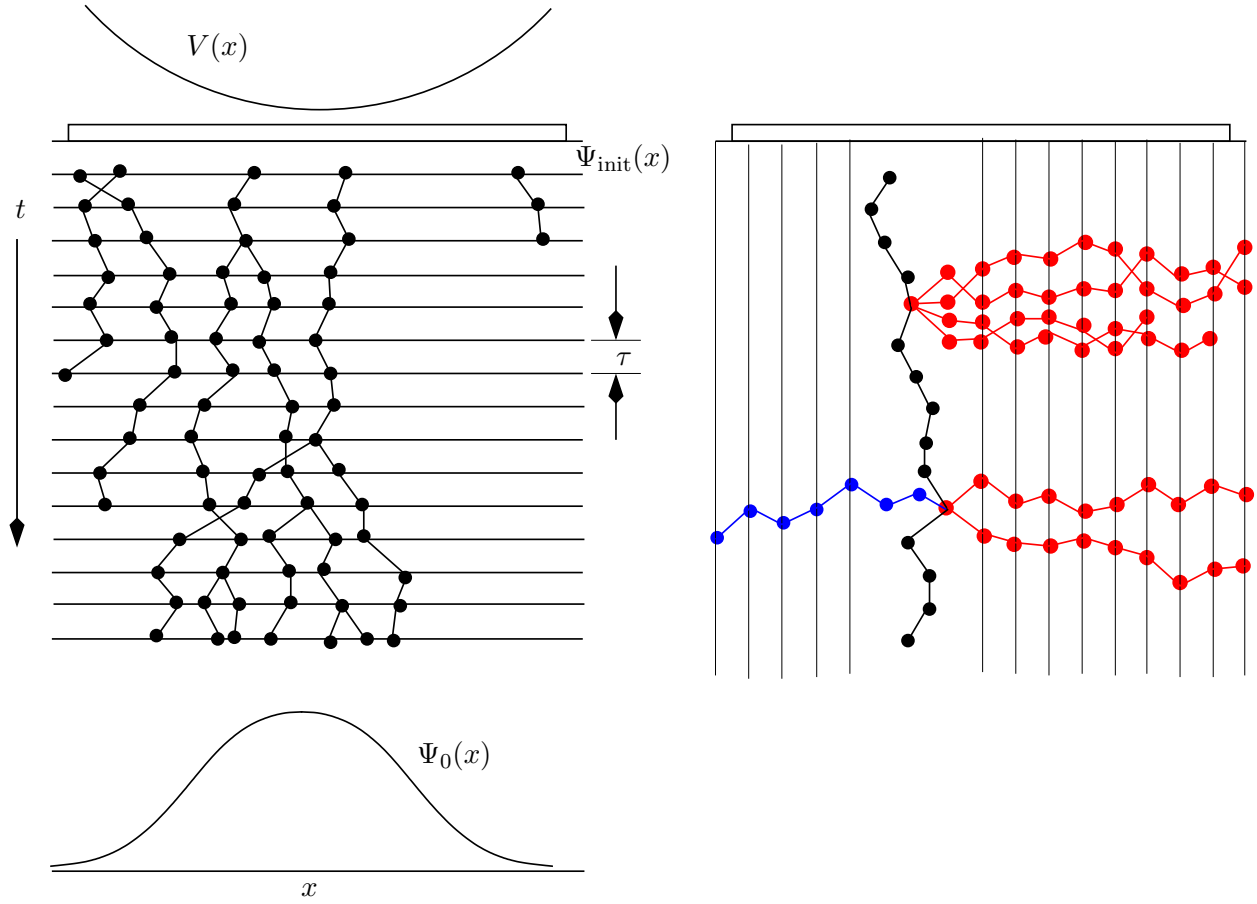

Figure 3.1: The Branching algorithm

i.e. the branching obtained by using the stochastic potential is correct to second order in τ. Hence this poses a limitation on the size of the time step that we can use. However, the most important factor in the error is the prefactor of τ^2 which depends on the device geometry in the problem. This error is unacceptable since our main motivation of sampling the potential stochastically is to improve the accuracy over other alternative methods. To improve the accuracy of the branching we could use a large enough number of runners to estimate the potential so that the noise is negligible, but this is *very* expensive and contrary to the philosophy of improving accuracy using a stochastic estimate of the potential.

To overcome this problem we use tecniques inspired by the penalty method [12] which modifies a random walk to accept noisy energies. The major part of the following discussion is a direct application of the penalty method. However as we will show there are also some very subtle and special considerations in the present use of the penalty method. Let $\tilde{V}$ be a WOS potential

estimate for some configuration $\boldsymbol{R}$, while V is the exact potential for the same configuration. $\mathbb{G}_B(V)$ is the previously defined branching term using the exact potentials, while $\tilde{\mathbb{G}}_B(\tilde{V})$ is the same expression using the WOS potentials. This branching factor will definitely be biased, and hence we introduce a modified branching factor $g_B(\tilde{V})$ which depends only on the estimate $\tilde{V}$. Let $\mathbb{P}(\tilde{V})$ be the probability for obtaining the estimate $\tilde{V}$. For the calculation using the WOS potential to be accurate, we require that the average branching must satisfy

$$\langle g_B \rangle \equiv \int_{-\infty}^{\infty} d\tilde{V}\ \mathbb{P}(\tilde{V}) g_B(\tilde{V}) = \mathbb{G}_B(V, \tau), \tag{3.9}$$

so that even with a stochastic potential the walker would branch correctly on average.

In order to make progress we have to assume a form for the probability distribution $\mathbb{P}(\tilde{V})$. In the limit of large number of runners, the central limit theorem guarantees that the distribution will be normal, but our primary goal is to use as few runners as possible and hence the distribution will certainly be somewhat different from a standard normal. Nevertheless, for now we assume a normal distribution with mean V and a known variance σ^2.

$$\mathbb{P}(\tilde{V}) = \frac{1}{\sqrt{2\pi\sigma^2}} \exp\left[-\frac{1}{2}\frac{(\tilde{V}-V)^2}{\sigma^2}\right]. \tag{3.10}$$

The variance σ^2 is not known in general but we assume that we know it for now; the penalty method estimates the necessary corrections which we will briefly mention at the end of this section.

A simple solution for the modified branching term $g_B(\tilde{V})$ which satisfies the above considerations is

$$g_B(\tilde{V}) = \exp[-(\tilde{V} + \sigma^2\tau/2)\tau]. \tag{3.11}$$

To see that this indeed satisfies the condition that $\langle g_B(\tilde{V}) \rangle = \mathbb{G}_B(V)$, consider a simple form for the modified branching $g_B = \gamma(\sigma^2)\tilde{\mathbb{G}}_B(\tilde{V})$ along with the probability distribution Eq.(3.11) and substitution in Eq.(3.9) leads directly to the form of $\gamma(\sigma^2) = \exp\left[-\sigma^2\tau^2/2\right]$. Since σ^2 is always positive, this shows that we rely less on a noisy potential and branch less than what we would if the estimate was exact.

This can be easily extended to the importance sampled branching factor

$$g_B(\boldsymbol{R}, \boldsymbol{R}') = \exp\left[-(\tilde{E}_L + \tilde{E}'_L + (\sigma^2 + \sigma'^2)\frac{\tau}{2} - 2E_T)\frac{\tau}{2}\right] \tag{3.12}$$

where $\tilde{E}_L(\tilde{V})$ is the local energy using the stochastic estimate of the potential. The analysis up to this point is a direct extension of the penalty method of Ceperley and Dewing [12], but certain special considerations need to be made to apply the penalty method in the present context.

Branching according to the above factor in Eq.(3.12) instead of the branching of Eq.(3.7) will produce the correct expectation of observables independent of the WOS potential $\tilde{V}$, for example the kinetic energy. If however the observable is dependent on the stochastic potential $\tilde{V}$, like the potential energy itself, we have to take care of the correlations between the observable and the branching factor. This can be seen from considering the expectation of the energy which is usually evaluated from the mixed estimator [23] given by

$$\begin{aligned} E_{\mathrm{DMC}} = \frac{\langle\psi_0|\mathcal{H}|\Psi_T\rangle}{\langle\psi_0|\Psi_T\rangle} &= \lim_{\tau\to\infty} \frac{\int d\boldsymbol{R} f(\boldsymbol{R},\tau) E_L(\boldsymbol{R})}{\int d\boldsymbol{R} f(\boldsymbol{R},\tau)} \\ &= \lim_{\tau\to\infty} \frac{\int d\boldsymbol{R} d\boldsymbol{R}' G(\boldsymbol{R},\boldsymbol{R}';\tau) f_{\mathrm{init}}(\boldsymbol{R}') E_L(\boldsymbol{R})}{\int d\boldsymbol{R} d\boldsymbol{R}' G(\boldsymbol{R},\boldsymbol{R}';\tau) f_{\mathrm{init}}(\boldsymbol{R}')} \\ &= \frac{1}{M}\sum_m E_L(\boldsymbol{R}_m) \end{aligned} \tag{3.13}$$

where we have simply used the form of Eq.(3.5) starting with the initial distribution f_{init}. If however, we use DMC with a stochastic potential, then the expectation of the local energies become

$$\begin{aligned} \tilde{E}_{\mathrm{DMC}} &= \frac{1}{M}\sum_m \tilde{E}_L(\tilde{V}, \boldsymbol{R}_m) \\ &= \frac{\int d\boldsymbol{R} d\boldsymbol{R}' d\tilde{V} d\tilde{V}' d\tilde{V}'' \tilde{g}(\boldsymbol{R},\boldsymbol{R}',\tilde{V},\tilde{V}';\tau) f_{\mathrm{init}}(\boldsymbol{R}') \mathbb{P}(\tilde{V}') \mathbb{P}(\tilde{V},\tilde{V}'') \tilde{\mathcal{E}}_L(\tilde{V}'',\boldsymbol{R})}{\int d\boldsymbol{R} d\boldsymbol{R}' d\tilde{V} d\tilde{V}' \tilde{g}(\boldsymbol{R},\boldsymbol{R}',\tilde{V},\tilde{V}';\tau) f_{\mathrm{init}}(\boldsymbol{R}') \mathbb{P}(\tilde{V}) \mathbb{P}(\tilde{V}')}. \end{aligned} \tag{3.14}$$

Here $\tilde{g}(\boldsymbol{R},\boldsymbol{R}',\tilde{V},\tilde{V}';\tau) \approx G_{\mathrm{diff}}(\boldsymbol{R},\boldsymbol{R}';\tau)\tilde{g}_B(\tilde{V},\tilde{V}';\tau)$ is the modified Green's function, $\mathbb{P}(\tilde{V})$ is the distribution of the WOS estimate, and $\mathbb{P}(\tilde{V},\tilde{V}'')$ is the joint probability distribution of obtaining the estimates $\tilde{V}$ and $\tilde{V}''$. $\tilde{V}''$ is the estimate used to evaluate the "modified" local energy $\tilde{\mathcal{E}}_L(\tilde{V}'',\boldsymbol{R})$. The estimate $\tilde{E}_{\mathrm{DMC}}$ given by Eq.(3.14) is not in general equal to the desired estimate E_{DMC}. The problem and a solution can be seen from a simple analysis and a modification of the estimator that

will give the desired result. The simplest way to accomplish this is to require the numerators and denominators in Eq.(3.13) and Eq.(3.14) to be equal separately. Our previous choice of $\tilde{g}_B$ makes the denominators equal. This is seen from the fact that

$$\tilde{g} = \gamma G_{\text{diff}} \tilde{G}_B = [\gamma(\sigma^2, \sigma'^2) e^{-\Delta\tau} e^{-\Delta'\tau}] G(\boldsymbol{R}, \boldsymbol{R}')$$

where as in prior notation $\Delta = \tilde{V} - V$ and similarly for Δ'. Substitution into the integral in the denominator of Eq.(3.14) proves the result.

The numerator is more tricky, and depends on the algorithm for obtaining the estimator. The part of the estimator that does not depend on the WOS estimate, i.e. the kinetic energy is does not pose any trouble, it integrates in the same way as the denominator. The potential part could be obtained in two different ways. In the simplest case, we could use separate and independent estimates $\tilde{V}$ and $\tilde{V}''$ for the branching and the estimator. In this case the probabilities would be uncorrelated and $\mathbb{P}(\tilde{V}, \tilde{V}'') = \mathbb{P}(\tilde{V})\mathbb{P}(\tilde{V}'')$. In this case, the integrals again become similar to those explained before and no modification is necessary, i.e. $\tilde{\mathcal{E}}_L = \tilde{E}_L$. We will call this the uncorrelated penalty correction. If however, we use the same potential $\tilde{V}$ for both the branching and the estimator, then the two estimates are identical, i.e. $\mathbb{P}(\tilde{V}, \tilde{V}'') = \delta(\tilde{V} - \tilde{V}'')\mathbb{P}(\tilde{V})$. In this case a modification of the form $\tilde{\mathcal{E}}_L(\boldsymbol{R}) = \tilde{E}_L(\tilde{V}, \boldsymbol{R}) + \sigma^2\tau$ makes the estimator $\tilde{E}_{\text{DMC}}$ equal to the desired $\tilde{E}_{\text{DMC}}$. This can be seen from simply substituting and performing the integration in Eq.(3.14).

Up to this point we have assumed that the distribution of the WOS potential $\tilde{V}$ is normal, $\mathbb{P}(\tilde{V})$ given by Eq.(3.10) with a known noise σ^2. Ceperley and Dewing [12] discuss the practical issues using the penalty method. Following them, for a potential estimate using n WOS runners, we generate a sequence $\{\tilde{V}_0, \ldots, \tilde{V}_{n-1}\}$, where each $\tilde{V}_k$ is independent. We use $\tilde{V} = \sum_i \tilde{V}_i/n$ as the potential estimate, and $\chi^2 = \sum_i (\tilde{V}_i - \tilde{V})^2/n(n-1)$ as the estimator for the noise σ^2. Their suggested form for the correction to the noise when the distribution is not normal is

$$\frac{\sigma^2\tau^2}{2} \longrightarrow \frac{\chi^2\tau^2}{2} + \frac{\chi^4\tau^4}{4n(n+1)} + \frac{\chi^6\tau^6}{3(n+1)(n+3)} + \ldots \tag{3.15}$$

in of Eq.(3.11).

We conclude this section by a comment on implementation. While constructing the propagator

$G(\boldsymbol{R}, \boldsymbol{R}')$ it is customary to reuse the energy $E_L(\boldsymbol{R})$ which was calculated in a prior step during the move to the configuration $\boldsymbol{R}$. However, with the stochastic potential we need to reevaluate $\tilde{\mathcal{E}}_L(\boldsymbol{R})$ again, as otherwise this will introduce a bias.

Chapter 4

QMC-WOS: A Toy Problem

We demonstrate the techniques discussed in this paper in the context of a simple problem and calculate the polarizability of helium by placing a helium atom in the electric field generated between the plates of an infinite capacitor. This will illustrate several features of implementing the WOS algorithm. Alternatively, we can model the system by a constant electric field and compare the accuracy of QMC using the stochastically estimated potential. The model potential neglects the effect of induced image charges which is small when the plates are far apart, but the WOS solution includes these corrections. We first describe the device, and compare the efficiency and accuracy of different refinements of the basic WOS algorithm to estimate the potential profile within the device.

4.1 Polarizability of He by QMC

We implement these techniques to measure the polarizability of helium, and compare the results with that obtained by using a model potential. The polarization (estimated by $\langle z \rangle$) is not an observable of the Hamiltonian, and so we have to use the mixed estimator

$$p \equiv \langle z \rangle = 2\langle z \rangle_{DMC} - \langle z \rangle_{VMC}$$

This clearly is not the best way to measure polarizability since this increases the variance of the estimate. If the variance of the VMC and DMC calculations are σ_V^2 and σ_D^2 respectively then the variance of p is $(\sigma_V^2 + 4\sigma_D^2)^{1/2}$. Caffarel et al uses the Laplace transform of a two- (imaginary) time correlation function for a more accurate estimate of the polarization by QMC [7]. Nevertheless,

this simple approach will be able to investigate the main goal of this test, i.e. how the calculations using the WOS potential compare with those using the model potential.

We place a helium atom between the plates of an infinite capacitor. The plates are at $z_L = \pm 10$ a.u. and the helium atom is placed at $z_0 = 0$. A voltage of $\pm\Phi_{\rm app}$ is applied to the gates, and this is compared with a model electric field of $\mathcal{E}_z = -\Phi_{\rm app}/z_L$. All numbers are in atomic units. The plates are kept sufficiently far away from the atom such that the effect of the images charges induced in the plates is small. This allows a comparison of results obtained with WOS with that using a model linear potential $-\mathcal{E}_z z$. Also if the plates are very close to the atom it could interfere with the electron cloud and distort the atom radically.

4.2 The Trial Wave function

We choose a trial wave-function of the form

$$\Psi_T(\boldsymbol{q}_1, \boldsymbol{q}_2) = |\mathbf{1}s(\boldsymbol{q}_1)\rangle|\mathbf{1}s(\boldsymbol{q}_2)\rangle \exp\left(-\frac{aq_{12}}{1+bq_{12}}\right)$$

where the $\boldsymbol{q}$s are the electron coordinates, $q_{ij} = |\boldsymbol{q}_i - \boldsymbol{q}_j|$, and a and b are variational parameters. We can determine a to be $-1/2$ by imposing the cusp condition [23] which reflects the divergence in the wave-function when the two electrons approach each other. Here $|\mathbf{1}s(\boldsymbol{q})\rangle$ is the single particle orbital and same for up and down spins. This simple two electron problem avoids the complications of nodes in wave-functions and helps illustrate the main issues of using WOS with quantum Monte Carlo.

The conditions of the problem have been set such that the capacitor adds only a small perturbation to the helium atom, and thus we need only modify the single particle orbitals very slightly to reflect the polarization of the atom in the z direction. The wave-function of helium in free space is spherically symmetric, and since VMC does not modify the wave-function it would not be able to polarize the atom. Hence we introduce a parameter α which would control the polarization of the atom. A zero value of α would correspond to the unpolarized case.We choose a form

$$|\mathbf{1}s(\boldsymbol{q})\rangle = (1+\alpha q_z)\sum_{j=0}^{4} c_j \exp(-\lambda_j q),$$

where q_z is the z-coordinate of $\boldsymbol{q}$, and the parameters c_j, λ_js are obtained from calculations of Clementi and Roetti [13]. We use pre-optimized values of these parameters ($c_1 = 2.063076 \times 10^{-1}$, $c_2 = 2.2346 \times 10^{-1}$, $c_3 = 4.082 \times 10^{-2}$, $c_4 = -9.94 \times 10^{-3}$, $c_5 = 2.3 \times 10^{-3}$ and $\lambda_1 = 1.4171, \lambda_2 = 2.3768, \lambda_3 = 4.3963, \lambda_4 = 6.527, \lambda_5 = 7.9425$).

We optimize the Jastrow parameter b and the polarization parameter α by correlated sampling. When we use the stochastic potential we minimize only the mean of the local energy, and not any combination of the variance. As described before, we record not only the configurations $\{\boldsymbol{R}\}$, but also the local potential energy $V(\boldsymbol{R}_m)\ \forall\ m$ for use in minimization of the variational energy. The polarization obtained from VMC with the optimized parameters provide an estimate for the polarization, but as noted earlier this is not very accurate since polarization is not an observable of the Hamiltonian.

4.3 Polarizability Results and Analysis of the Penalty Method

We test our code by calculating the ground state energy of a helium atom, our result $-2.90361(9)$ a.u. compares well with the best known theoretical estimate of -2.903724377034119598 a.u. [26] and experimental value of -2.9038 a.u. [70]. Next we carry out the calculations in presence of an electric field by two different methods as described before. WOS refers the calculations using the stochastic potential, and "model" refers to the linear potential model. The results are shown in Table 4.1. From a least-square fit of the data our estimate for the polarization is 1.417(16) a.u. from the WOS data as in Fig.(4.1) and 1.362(16) a.u. from the model calculation, which can be compared with 1.382(16) a.u. as obtained by Cafarrel et al. [7], and with the established value of 0.201×10^{-24} cm^3 or 1.36316 a.u. [15, 56, 35].

The result suffers from the drawbacks of our estimator as discussed before, but the main point to note is the comparison between the WOS and "model" results. The difference in the result comes from the induced charges in the capacitor (not captured in the model) as will be discussed below. From Table 4.1 we see that the results agree within error-bars for both the optimized VMC calculations and DMC. The DMC calculations were carried out using only twenty runners for each walker configuration. We also use the penalty method the results of which will be discussed next.

To investigate the effect of using the WOS potential in DMC we study the time-step error,

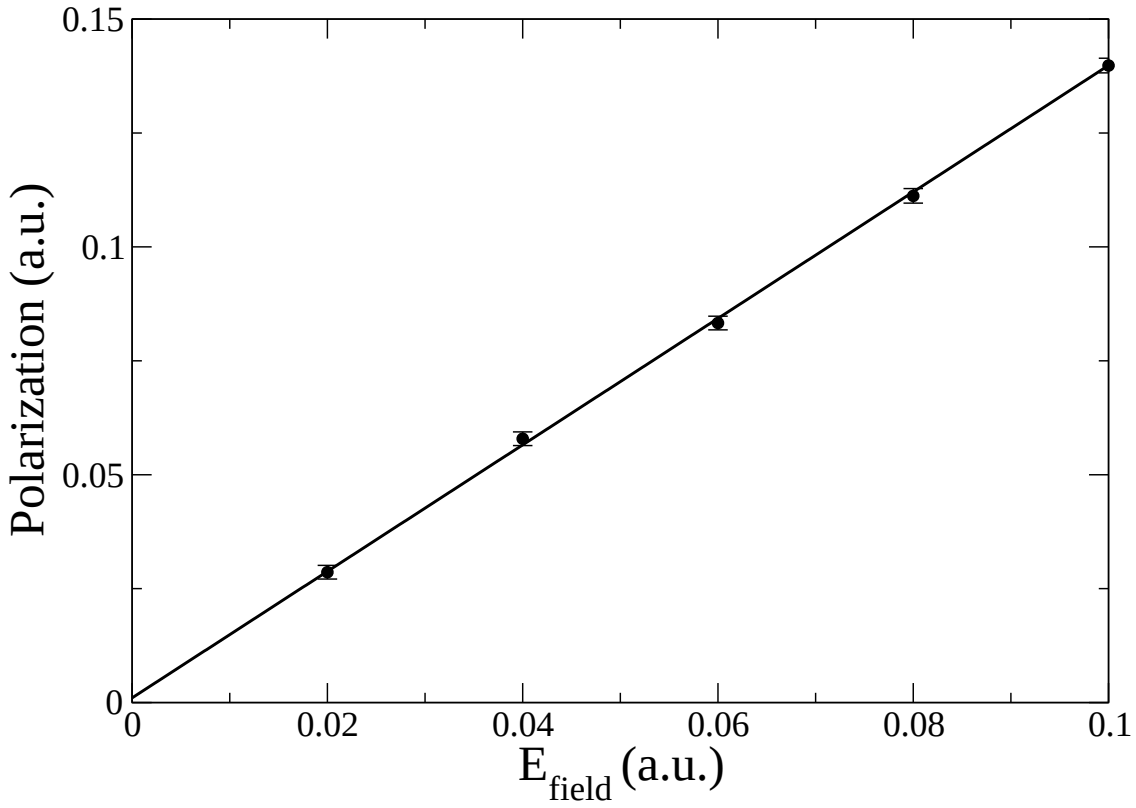

Figure 4.1: Least square fit of the polarization data obtained from the WOS calculation of the helium atom placed between the plates of an infinite capacitor. The result used is the mixed estimator obtained from the VMC and DMC data presented in Table 4.1. The data for the model calculation is not shown since it nearly overlaps with the WOS data.

since we expect the effect of the using the stochastic potential to be magnified with increasing time-step, as seen in Eq.(3.8). In Fig.(4.2) we compare the DMC ground state energy from the model potential calculation to that using WOS for different number of runners (per walker). The uppermost curve labeled "model" is the linear potential model which shows a quadratic scaling with the time-step. The lowermost curve labeled WOS(1) represents DMC calculations using a single runner (per walker) without any penalty correction. This obviously suffers from the branching error which is magnified at larger time-steps.

If however we increase the number of runners (per walker) to 5, we see from the WOS(5) curve that the result is improved but still suffers from the bias. The use of the penalty method corrects this problem, and the curve marked penalty(5) follows the model potential for the entire range of τ that we tested. We also note that the correction of Eq.(3.15) did not make a difference to the calculation within the given error-bars. If we increase the number of runners to about twenty, then

	E_G				p_z					
	VMC		DMC		VMC		DMC		Mixed	
$\mathcal{E}_z$	WOS	model	WOS	model	WOS	model	WOS	model	WOS	model
0.02	-2.888461(92)	-2.888080(97)	-2.904313(85)	-2.904149(89)	0.0268(6)	0.0257(6)	0.0277(7)	0.0277(7)	0.0286(15)	0.0297(15)
0.04	-2.889087(95)	-2.888904(93)	-2.905298(82)	-2.904932(82)	0.0611(6)	0.0469(6)	0.0595(6)	0.0529(6)	0.0579(15)	0.0589(15)
0.06	-2.890392(100)	-2.890119(94)	-2.906741(87)	-2.906314(81)	0.0827(6)	0.0702(7)	0.0830(7)	0.0776(7)	0.0833(15)	0.0850(16)
0.08	-2.892102(100)	-2.891927(99)	-2.908636(84)	-2.908208(86)	0.1084(7)	0.1081(7)	0.1098(7)	0.1109(7)	0.1112(16)	0.1137(16)
0.10	-2.894533(110)	-2.894134(95)	-2.911209(89)	-2.910856(89)	0.1332(7)	0.1332(7)	0.1385(7)	0.1341(7)	0.1438(16)	0.1350(16)

Table 4.1: Calculation of polarization of helium with quantum Monte Carlo. The system consists of a helium atom placed between the plates of an infinite capacitor as described in this section. Two similar calculations were run, one using the stochastic potential using the WOS algorithm, and the other using a model linear potential. The VMC results here are obtained by optimizing the trial wave-function. For DMC, we used a time-step of $\tau = 0.01$.

the basic WOS calculation without the penalty method is greatly improved, and it overlaps with the correct result for a large range of τ up to about 0.2 in this calculation; but beyond that the bias in the result becomes apparent. Since the calculations using the penalty method with five runners and twenty runners (per walker) overlapped with each other we did not show them separately in the figure.

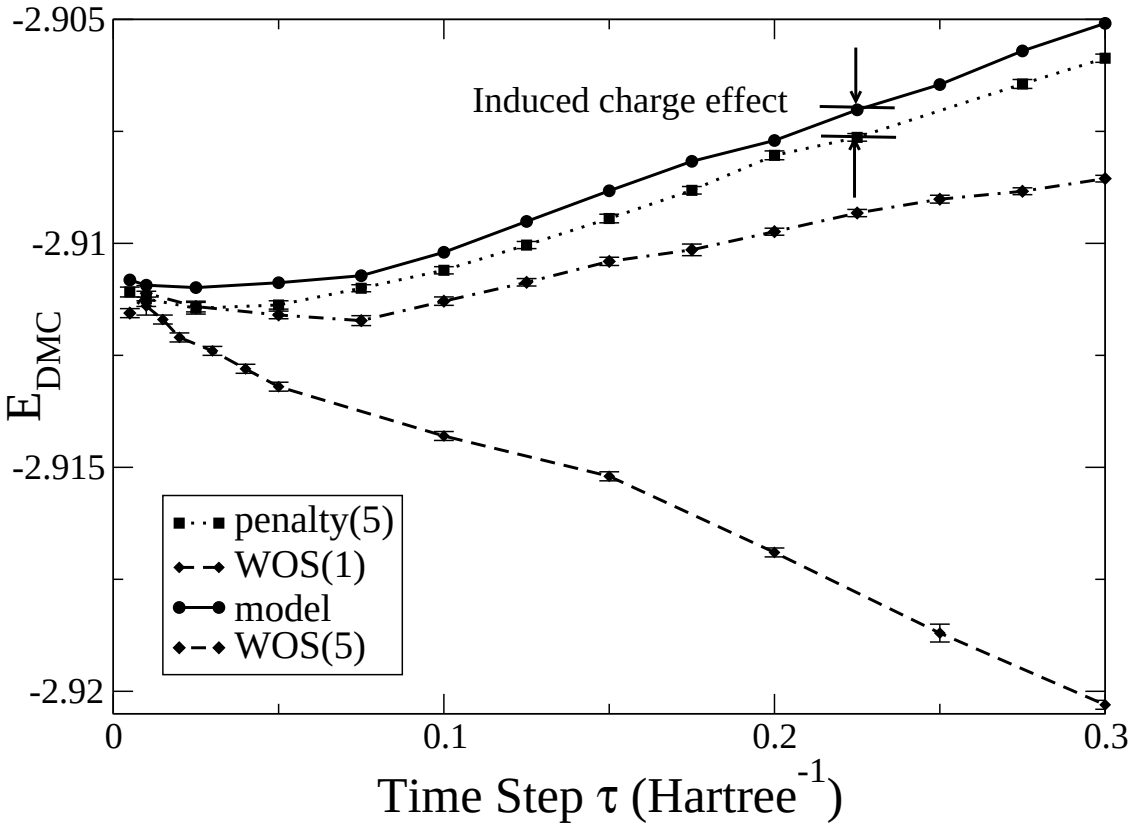

Figure 4.2: Ground state DMC energy of the helium atom in an electric field of $\mathcal{E}_z = 0.1$ for different time steps. In parenthesis is the number of runners used per walker for the WOS calculations. This is compared with the calculation using the model field.

Though the model and the penalty calculations run parallel, they are offset by a constant amount. This is to be expected since the model calculation neglects the effect of the charges induced on the capacitor plates. A very simple calculation using dipole images (but neglecting multiple reflections) estimates this effect to be about 2×10^{-4} a.u., the same order of the observed shift of 3×10^{-4} a.u. Thus the WOS calculation can capture the induced charge effect neglected by the model.

To study the effect of the penalty method, we compare in Fig.(4.3) the effect of the two different

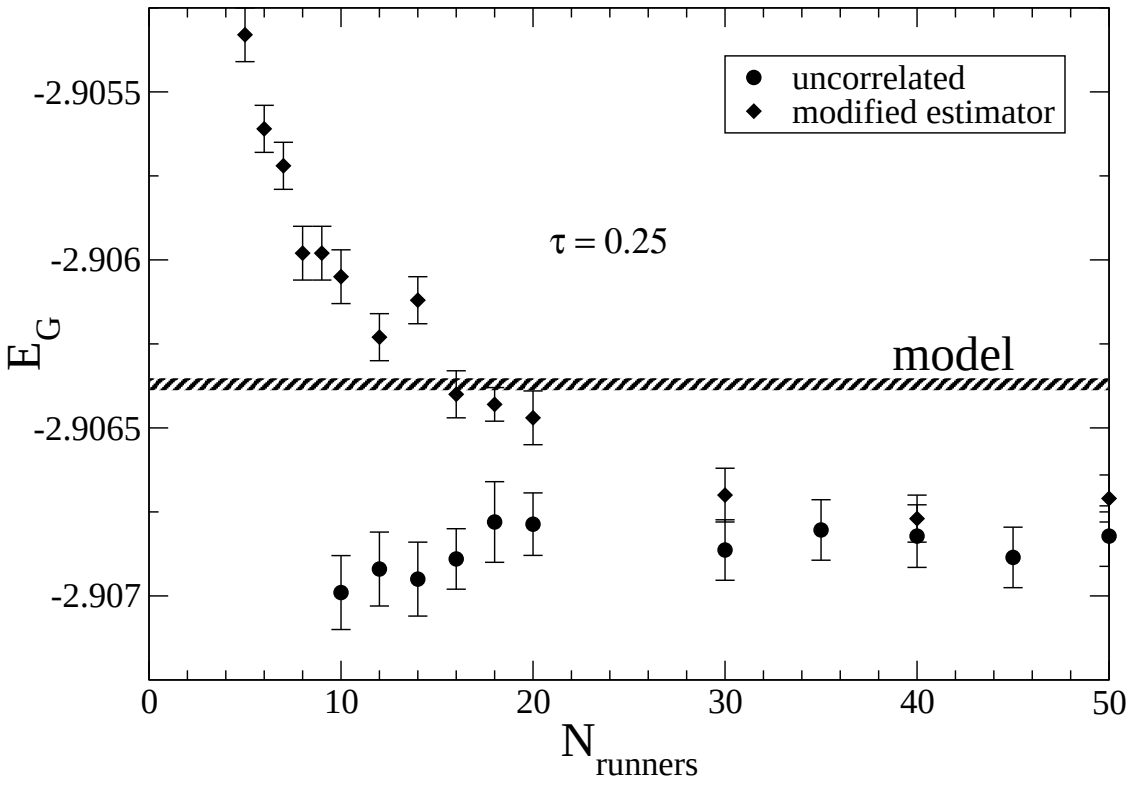

Figure 4.3: Testing the convergence of the two penalties. The uncorrelated penalty method using an independent uncorrelated (to the branching) potential estimate converges much faster than the approach where we modify the estimator. However, for a large number of runners the second converges to the correct result from above. The calculation was carried out at $\tau = 0.25$. The difference from the model is due to the induced charge effect.

types of penalty corrections that we discussed in section 3.2. In the calculations we use a large number of runners (per walker) to estimate the potential to be used in the branching term. The first estimator uses a separately sampled value, we call this the uncorrelated penalty approach. We can construct another estimator using the same estimate that we use for the branching, but then we have to add another correction to it as discussed before. Fig.(4.3) shows that the uncorrelated penalty method has a faster convergence, but both approaches converge for large number of runners (per walker).

Also shown in Fig.(4.3) is the estimate of the model calculation. We see that the WOS calculations converge to a value lower than the model. This is the induced charge effect as mentioned earlier. As we increase the separation of the capacitor plates, this effect decreases and for a plate separation of about 100 a.u. (keeping the electric field constant) the WOS results converge to the

model value. This demonstrates another important feature of the algorithm. In order to keep the field constant, we had to increase the gate voltages. The algorithm remained stable under this scaling.

The WOS calculations with a single runner (per walker) were only about four times slower than that with the model potential, this is not too bad considering the generality of the WOS method. The WOS method can be applied to any complicated geometry for which a model might not exist, however the time taken by the code will also depend on the complexity of the device geometry. However, calculations scales linearly with the number of runners, for instance the calculation with twenty runners was about twenty times more expensive than the one with a single runner.

Chapter 5

Laterally Coupled Quantum Dot

Advances in semiconductor technology has allowed the construction of nano-scale devices which can create small islands of discrete number of electronic charges called quantum dots. These islands exhibit electronic properties (like ionization energy and discrete excitation spectrum) very similar to that of atoms and are hence also known as artificial atoms [45] . A common way to fabricate quantum dots is to restrict the two-dimensional electron gas in a semiconductor heterostructure laterally by electrostatic gates, or vertically by etching techniques [62]. This creates a bowl-like potential in which the conduction electrons are trapped. The fact that their properties can be manipulated by controlling gate voltages or by manufacturing techniques make these "designed atoms" an extremely interesting system to study and candidates for a variety of technical applications, from quantum computing to biological applications. The fabrication and etching methods and experimental background has been covered exhaustively in the literature [62, 72]. Of particular interest to scientific studies are the shell like electronic structure , addition energies [24], Coulomb blockade [44] and the effect of magnetic fields on the singlet-triplet splitting [73].

The traditional approach to attack a correlated few-electron problem like the few electron quantum dot has been to apply configuration-interaction methods [6], but they scale very poorly with increasing electron number. Moreover most theoretical calculations assume that the excited state in the vertical direction is inaccessible to the electrons, and hence only two dimensional calculations are considered. Unfortunately recent studies by Rontani [65] have concluded that 2D models lead to inadequate estimations of the Coulomb interactions in realistic dots. As a consequence they conclude that studies in 2D are overly biased towards electronic localization. In real quantum dots the lateral confinement is about 10 times that of the vertical confinement,

however studies [41] have shown that the exact exchange energy of the system approach the 2D limit only when the lateral confinement is about 30 times that of the vertical confinement. Wilkens [72] discusses in some detail the historical background of applying quantum Monte Carlo to realistic three dimensional model of quantum dots. There has been investigations into the extent of the singlet-triplet splitting on model 2D potentials, either by Hartree-Fock [73] or even spin-density-functional theory and VMC [67]. But none has applied diffusion Monte Carlo to a realistic 3D model. We use the DFT calculations [50] on a realistic device to apply the quantum Monte Carlo algorithm.

5.1 The Device Structure

We follow the semiconductor heterostructure model described by Elzerman [20] and Zhang [76]. The upper part of Fig.(5.1) shows the top view of the LCQD and QPC gates in the xy-plane. The metal gates are used to define the two wells which confine the dots. The lower part of the figure shows the cross sectional view of the layer structure in the vertical z-direction. The model involves four different layers of semiconductors, each of different thickness and with different doping. The composition of the device structure is given in Table (5.1).

material	thickness ($\mathring{A}$)	type	doping(cm^{-3})	ϵ	$m^\star$	E_c(eV)
GaAs	50	n	$N_D = 1.5 \times 10^{18}$	12.406	0.067	0.0
$Al_{0.27}Ga_{0.73}As$	650	n	$N_D = 1.5 \times 10^{18}$	12.244	0.092	0.33
$Al_{0.27}Ga_{0.73}As$	200	–	undoped	12.244	0.092	0.33
GaAs	16,100	p	$N_A = 1.0 \times 10^{15}$	12.406	0.067	0.0

Table 5.1: The vertical composition of the heterostructure.

The 2D electron gas is formed in the interface between the undoped AlGaAs layer and the lightly p-type doped GaAs layer, approximately $900\mathring{A}$ below the top surface. Biases applied to the top gates clear islands in this gas to form the double well structure represented by the ovals in the figure. This is due to the geometry of the L and R gates. The coupling between the two dots is dependent on the height of the potential barrier between the two well, and this is controlled by the M and T gates. The PL and PR gates, called the "plungers", have smaller feature sizes and are used for fine tuning the confinement of each dot, i.e. they control the depth of the wells. The QPC-L and QPC-R are associated with the L and R gates (via the tips) and forms the quantum

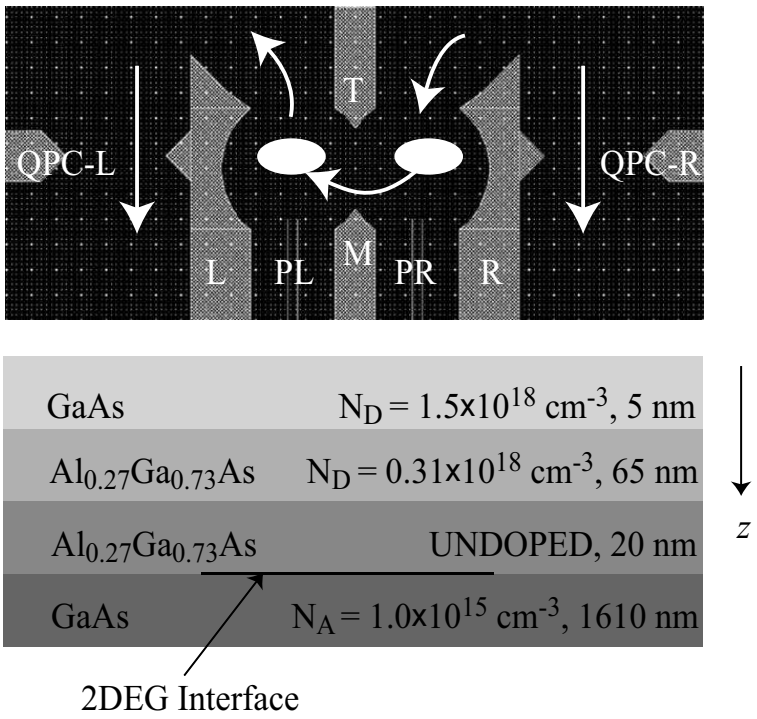

Figure 5.1: A schematic diagram of the laterally coupled double quantum dot heterostructure. The upper section of the figure shows the top surface with the external gates. The length along the horzontal direction is 1400 nm, with the distance between the L and R gates being about 500 nm, and that between PL and PR being about 300 nm. The lateral dimension of the device is 570 nm.

point contact (QPC) detectors. The charging path of the dots are shown by the curved arrows while the detection current is shown by the straight ones. The current through the dots influences the detector currents which is picked up by the QPCs.

5.2 The Density Functional Approach

The starting point of the QMC calculation is from the solutions of the density functional theory (DFT) calculations. We will only describe the approach, details can be found in the works of Leburton and coworkers [59, 47, 76] The electronic charge density in the quantum dot region is obtained by simultaneously solving the Kohn-Sham equations [42] for the spin up and spin down electrons. The density if obtained through the eigen-functions of the Kohn-Sham Hamiltonian

$$\mathcal{H} = -\frac{\hbar^2}{2}\nabla\left[\frac{1}{m^\star(\boldsymbol{r})}\nabla\right] - e\Phi(\boldsymbol{r}) + \Delta E_c + \Phi_{xc}(n),$$

where $m^\star(\boldsymbol{r})$ is the material dependent (i.e. for the heterostructure, position dependent) effective mass. $\Phi(\boldsymbol{r})$ is the potential obtained from $\Phi = \Phi_{\text{ext}} + \Phi_{\text{doping}} + \Phi_H$. Φ_{ext} is the potential due to the external gates, Φ_{doping} is the potential due to the ionized donors and acceptors, and Φ_H is the Hartree potential arising due to the repulsive inter-electronic interaction. ΔE_c is the conduction band offset between different materials. $\Phi_{xc}(n)$ is the exchange correlation potential energy for spin-up and spin-down, computed within the local spin density approximation (LSDA) according to the Perdew and Wang formulation [57].

The electron density in the LCQD region $n(\boldsymbol{r})$ is computed from the sum of the densities of the up and down eigen-functions (i.e. their modulus squared). The electrostatic potential, which is of special interest for the QMC-WOS calculation, is obtained by solving the Poisson's equation

$$\nabla \cdot [\varepsilon(\boldsymbol{r})\nabla]\Phi(\boldsymbol{r}) = -\rho(\boldsymbol{r})$$

by a finite element method (FEM). $\varepsilon(\boldsymbol{r})$ is the material (position) dependent permittivity and $\rho(\boldsymbol{r})$ is the total charge density given by

$$\rho(\boldsymbol{r}) = e[N_D^+(\boldsymbol{r}) - N_A^-(\boldsymbol{r}) + p(\boldsymbol{r}) - n(\boldsymbol{r})]. \tag{5.1}$$

Here $N_D^+(\boldsymbol{r})$ and $N_A^-(\boldsymbol{r})$ are the ionized donor and acceptor concentrations in the relevant device layers, and $p(\boldsymbol{r})$ is the hole concentration. The electron density $n(\boldsymbol{r})$ is obtained from solving the Kohn-Sham equations in the LCQD region, while outside this region, the free electron charge density is determined from the semi-classical Thomas Fermi approximation.

So the charge density depends on the potential through the Kohn-Sham equations while the potential depends on the charge density by the Poisson equation. This is solved self-consistently by FEM. For the Poisson equation, Neumann boundary conditions (normal component of the electric field goes to zero) are assumed on the lateral and bottom surfaces, while the potential on the top surface is governed by the metal gates and the Schottky barrier. So the LCQD is in a small region embedded deep within the device structure. In the model, the physics in the LCQD is dominated by quantum mechanics, while outside the electrons are treated semi-classically, as noted above. This is also reflected in the grid mesh used to represent the device. The Poisson equation is solved

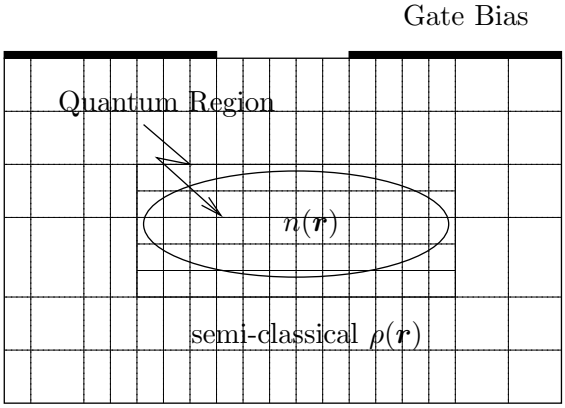

Figure 5.2: A schematic diagram of the heterostructure model. The device is represented on a non uniform rectangular grid which is finer near the quantum dot region, represented here by the oval. Since the electrons are completely confined within this region the Schroedinger's equation is solved within this inner grid.

over the entire device represented on a three dimensional non-uniform rectangular grid of dimension $141 \times 52 \times 96$. Since the wave function of the electrons in the dot vanish deep within the structure, the Kohn-Sham equations are solved on a smaller section of the grid spanning $71 \times 45 \times 19$ grid points. Fig.(5.2) shows a schematic diagram of the model.

5.3 The Quantum Monte Carlo Model

In QMC we simulate only the electrons in the LCQD region. The calculations are carried out under the effective mass approximation, just like the DFT model. In this approximation, the electrons are assumed to occupy the conduction band (E_c) and move through the semiconductor lattice in such a way that its motion can be described as that of a free electron but with an effective mass $m^\star$ which is related to the curvature of the band [30]. QMC is a zero temperature method, and hence to a good approximation, the electrons occupy only the lowest conduction band, and at the minima their effective mass remains approximately constant while they move through the semiconductor's bulk.

For numerical accuracy, we follow the standard practice of adopting the effective atomic units by setting $e^2/(4\pi\epsilon\epsilon_0) = m^\star_{\text{GaAs}} m_e = \hbar = 1$. Since the effective mass of the electron in GaAs is only a fraction of the free electron mass m_e, the effective units are different from the standard atomic units and represent the energy and length scales of the problem more effectively. The

effective Bohr radius $a_B^\star$ and the effective Hartree $Ha^\star$ are given by $a_B^\star = (4\pi\epsilon\epsilon_0\hbar^2)/(m^\star e^2)$ and $\mathrm{Ha}^\star = (m^\star e^4)/(4\pi\epsilon\epsilon_0\hbar)^2$. In terms of the standard atomic units

$$a_B^\star = \frac{\epsilon m_e}{m^\star} a_B, \qquad \mathrm{Ha}^\star = \frac{m^\star}{m_e \epsilon^2}\mathrm{Ha}$$

where $a_B = 0.5291772108\mathring{A}$, and Ha=27.2113845 eV. Since the electrons are mostly confined in the region slightly below the interface between the GaAs and AlGaAs layers, we use the GaAs as the reference material. With this choice the effective units become $a_B^\star = 9.79847$ nm and $\mathrm{Ha}^\star = 0.0118457$ eV.

We employ two different approaches within the QMC framework. In the first approach following Matagne et al [48, 72] we use the potential profile within the device obtained from the converged self consistent solution of Poisson and Kohn-Sham equations within DFT as described in the previous section. In the second approach we use the hybrid QMC-WOS method to derive the potential consistent with the boundary conditions while solving the quantum problem.

5.3.1 QMC with External Potential

In the effective units the Hamiltonian reduces to

$$\mathcal{H} = -\frac{1}{2}\sum_{i-1}^{N_e} \nabla_i \cdot \left[\frac{1}{m^\star(\boldsymbol{r}_i)}\nabla\right] + \sum_{i=1}^{N_e} \Phi_{\mathrm{conf}}(\boldsymbol{r}) + \sum_{i\neq j}^{N_e} \frac{1}{\epsilon|\boldsymbol{r}_i - \boldsymbol{r}_j|} \tag{5.2}$$

where $m^\star$ and ϵ are both unity as long as the electrons remain within the GaAs layer, otherwise the ratio of the parameters is used. Φ_{conf} is the confining potential of the dot arising from the applied gate voltages and the screening of the doped charges. This is obtained from the DFT calculations $\Phi_{\mathrm{conf}} = \Phi_{\mathrm{ext}} + \Phi_{\mathrm{doping}}$, discrete values distributed on the three dimensional grid as described before. These values $\Phi_{\mathrm{conf}} \equiv \Phi_{\mathrm{conf}}(i,j,k)$ are then interpolated using tricubic splines to obtain $\Phi_{\mathrm{conf}}(\boldsymbol{r})$ at any arbitrary point within the device. Of course, the electrons remain well confined within the LCQD region, but this is immaterial to the QMC algorithm. Thus the electrons can forget about the entire device and merely deal with the fact that they are confined by some potential supplied to the problem.

The last term in the Hamiltonian is the repulsive inter-electron Hartree energy, dependent

simply on the inter-particle separation. As mentioned above, the permittivity is unity (in the scaled units) as long as the electrons are in GaAs. Since the permittivity does not vary appreciably between the materials we use $\epsilon = 1$ throughout the calculation. This neglects the effect of image charges as the dielectric interface but is a reasonable approximation to make.

The external potential however is also an approximation. It is calculated using an average electron density in the DFT calculation, and the resulting image charges at the surface and interfaces. However, as the electrons evolve in the QMC, the images in the metal gates also respond. This Hamiltonian does not capture these effects.

5.3.2 QMC with Stochastically Obtained Potential

The idea behind obtaining the potential by a separate stochastic process during the QMC sampling is to capture the electronic interaction exactly. The Hamiltonian can be simply written as

$$\mathcal{H} = -\frac{1}{2}\sum_{i-1}^{N_e} \nabla_i \cdot \left[\frac{1}{m^\star(\boldsymbol{r}_i)}\nabla\right] + \Phi_{\mathrm{WOS}} \tag{5.3}$$

where Φ_{WOS} represents the entire potential energy obtained by the WOS method. This method captures the electronic interaction, the effect of the charges induced at the dielectric interfaces and the external surfaces.

The WOS calculations satisfy the boundary conditions. For ease of computation, we import the boundary values on the grid from the DFT calculation. This is simply an easy way of representing the boundary values, we could have employed any other scheme. The WOS walks (or runs) always end on the boundary where the solution is specified. Hence Dirichlet boundary conditions make the calculations more efficient. However this also modifies the problem slightly, imposing the boundary values make the surfaces act as metals. The top surface is indeed embedded with metal gates (all other surfaces are too far away), but the remainder of the surfaces are free to the external media (could be vacuum). The WOS algorithm is well equipped to handle this kind of problems, and we show a few sample paths which accomplish the task in Fig.(5.3). Since the potential is now not specified on sections of the top surface, the walks can diffuse through them outside the device. We could assume the exterior to be vacuum without any boundary, in that case the walks would have to

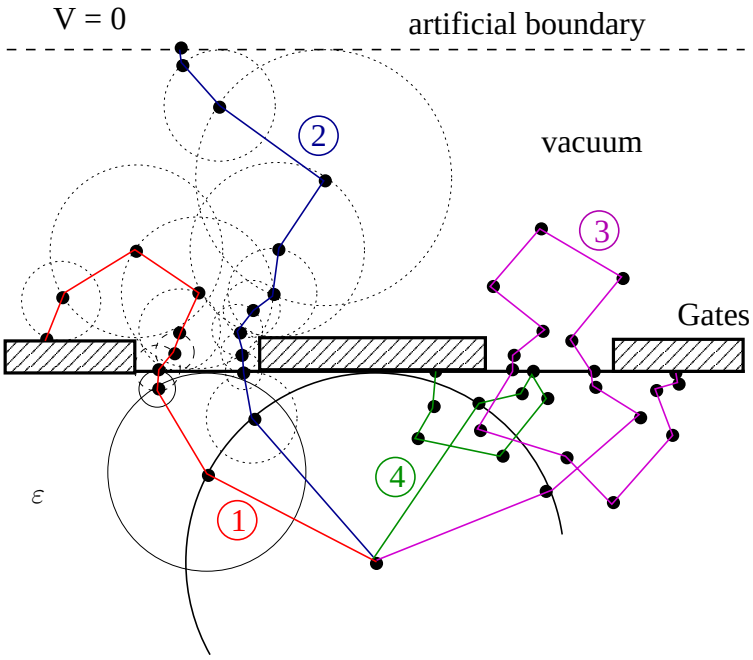

Figure 5.3: A schematic diagram of paths if we do not impose Dirichlet boundary conditions on the ungated sections of the top surface. Four typical types of path are shown. Path 1 diffuses through the surface but terminates on a gate where the potential is specified. Path 2 diffuses far outside the device, and is assumed to terminate on an artificial grounded surface. Path 3, diffuses outside, but then comes back into the device and Path 4 is reflected from the surface back into the device. Since typically $\varepsilon \gg 1$, most of the paths would be of this type.

diffuse back to the metallic plate before they can end. On the other hand we could impose artificial boundaries, for example to encase the entire device within a large grounded metal box. This will provide faster convergence. Typically the permittivity of the material will be much larger than that of vacuum $\varepsilon \gg 1$, this would mean that most paths (a fraction of $\varepsilon/(\varepsilon+1)$ on average) would be reflected back into the device like path number 4 in Fig.(5.3). But this approach becomes too expensive a calculation, and we simply assume the boundary conditions from the DFT calculations.

Other than the boundary conditions effecting Φ_{ext} we also have to account for the effect of doping Φ_{doping} on the confining potential. The doped distribution of these charges (treated semi-classically) is the initial condition of the problem. However as seen from Eq.(5.1) the charge density itself depends on the electronic walker density, and the initial dopant density is modified by emergence of the depletion layers. However the dependence of the charge density on the electronic density is extremely nonlinear [59] and this poses considerable difficulty for the WOS method which is effective primarily for linear problems. One possible approach is to assume a Thomas

Fermi like distribution with adjustable parameters for this density, and optimize those parameter by a variational calculation. However we have not experimented with such an approach. We take the simpler route of using the doped charge density on the grid ($\rho(\boldsymbol{r})-n(\boldsymbol{r})$) from the DFT solution and assume that this is not affected by the electronic motion.

5.4 Construction of the Wave Function

Quantum Monte Carlo requires a trial wave-function Ψ_T supplied to the algorithm. For this purpose we construct the singlet and triplet wave functions from single particle orbitals. First we review the structure of these wave-functions following Ashcroft and Mermin [1]. The spin part of the singlet wave-function $(|\uparrow\downarrow\rangle - |\downarrow\uparrow\rangle)/\sqrt{2}$ is antisymmetric and hence the space part is symmetric due to Pauli exclusion principle. Conversely, the space part of the triplet state is the lowest energy antisymmetric state. Since the Hamiltonian is spin independent, the spin part integrates out, and we need only focus on the space part.

The trial wave function is of the form

$$\Psi_T(\boldsymbol{r}_1, \boldsymbol{r}_2) = \exp\left(-\frac{ar}{1+br}\right)\psi_{s,t}(\boldsymbol{r}_1, \boldsymbol{r}_2)$$

where $r = |\boldsymbol{r}_1 - \boldsymbol{r}_2|$ and $\psi_{s,t}$ is the wave function for the singlet or triplet.

5.4.1 Singlet and Triplet wave functions

Let $\psi_0(\boldsymbol{r})$ and $\psi_1(\boldsymbol{r})$ be the solutions of lowest energy of the single particle problem. The symmetric solution of lowest energy under independent electron approximation is

$$\psi_s(\boldsymbol{r}_1, \boldsymbol{r}_2) = \psi_0(\boldsymbol{r}_1)\psi_0(\boldsymbol{r}_2)$$

and the lowest antisymmetric solution is

$$\psi_t(\boldsymbol{r}_1, \boldsymbol{r}_2) = \psi_0(\boldsymbol{r}_1)\psi_1(\boldsymbol{r}_2) - \psi_0(\boldsymbol{r}_2)\psi_1(\boldsymbol{r}_1)$$

For well separated wells, the tight binding method provides an excellent approximation; in this approach the one-electron-stationary-state wave functions of a solid are expressed as linear combinations of atomic stationary-state wave functions centered at lattice points. The laterally coupled quantum dot structure is much like a hydrogen molecule, instead of the two nuclei the two electrons are confined by the double well. In that vain consider $\phi_L(\boldsymbol{r})$ and $\phi_R(\boldsymbol{r})$ to be the single particle orbitals centered on the left and right dot respectively. The $N = 2$ correct linear combinations are

$$\begin{aligned} \psi_0(\boldsymbol{r}) &= \phi_L(\boldsymbol{r}) + \phi_R(\boldsymbol{r}) \\ \psi_1(\boldsymbol{r}) &= \phi_L(\boldsymbol{r}) - \phi_R(\boldsymbol{r}) \end{aligned} \tag{5.4}$$

If the one-electron levels have this form them the two electron wave functions become

$$\begin{aligned} \psi_s(\boldsymbol{r}_1, \boldsymbol{r}_2) &= \phi_L(\boldsymbol{r}_1)\phi_R(\boldsymbol{r}_2) + \phi_R(\boldsymbol{r}_1)\phi_L(\boldsymbol{r}_2) \\ &+ \phi_L(\boldsymbol{r}_1)\phi_L(\boldsymbol{r}_2) + \phi_R(\boldsymbol{r}_1)\phi_R(\boldsymbol{r}_2) \end{aligned} \tag{5.5}$$

and

$$\psi_t(\boldsymbol{r}_1, \boldsymbol{r}_2) = 2[\phi_R(\boldsymbol{r}_1)\phi_L(\boldsymbol{r}_2) - \phi_L(\boldsymbol{r}_1)\phi_R(\boldsymbol{r}_2)] \tag{5.6}$$

When the wells are very close to each other (for a large gate bias for example), Eq.(5.5) is an excellent approximation. In the extreme case when the two wells coincide, this corresponds to a well of double the strength. On the other hand, when the dots are well separated, the overlap of $\phi_L(\boldsymbol{r})$ and $\phi_R(\boldsymbol{r})$ is negligible, and electrons located in different wells will have negligible contribution from the last two terms in Eq.(5.5), and effectively reduce to

$$\bar{\psi}_s(\boldsymbol{r}_1, \boldsymbol{r}_2) = \phi_L(\boldsymbol{r}_1)\phi_R(\boldsymbol{r}_2) + \phi_R(\boldsymbol{r}_1)\phi_L(\boldsymbol{r}_2), \tag{5.7}$$

the Heitler-London approximation.

5.4.2 The Single Particle Orbitals

A good possible starting point for constructing the QMC trial wave function Ψ_T is the LDA single particle solution of the problem. However, the LDA data on the grid suffers from very small noise

at several orders of magnitude smaller than the peak value (typically $\mathcal{O}(10^{-6})$). Such small noise is irrelevant to any integrating scheme, but it adversely effects the Monte Carlo sampling. The noisy part of the LDA wave function is close to the wells and the electrons do indeed sample the gradient at neighboring points. Furthermore we found the grid point density in the vertical direction to be insufficient for accurate Monte Carlo calculations.

We performed our calculations with a hybrid of analytic functions, and discrete valued functions on the grid. We assumed a separable form of the wave function

$$\phi_T(\boldsymbol{r}) = X(x)Y(y)Z(z).$$

The functional forms were taken so as to approximate the LDA by fitting them along cross sections. We plotted the LDA orbitals along the principal directions through the point of the maxima, and fitted the analytic functions to those curves. Hence the single particle orbitals were smooth and well behaved and did not have spurious nodes.

Along the y-axis the potential is approximately parabolic, and so a Gaussian is a very good approximation. We chose the mean and width of the Gaussian to fit the data.

Along the x-axis, the potential is in the form of a double well, and the wells are locally parabolic. We tried approximating the wave function as a sum of two Gaussians centered on each well. This however does not provide the proper overlap between the two orbitals $\phi_L(\boldsymbol{r})$ and $\phi_R(\boldsymbol{r})$. A much better approach is to plot the LDA grid orbitals along the x-axis passing through the maxima of the wave function, and interpolate between these grid points to obtain a smooth and well behaved function with a better overlap.

Along the z-direction the region of interest is just adjacent to the band offset region. In this region the potential is almost linear below the interface. At the interface, the band offset creates a finite step. For this triangular well, an AiryAi function is a very good approximation. So, below the interface we assumed and AiryAi function, and above we assumed exponential decay. At the interface we simply matched their derivatives to produce a smooth and continuous function.

If the potential is modeled as shown in Fig.(5.5) then a very good approximation to the single

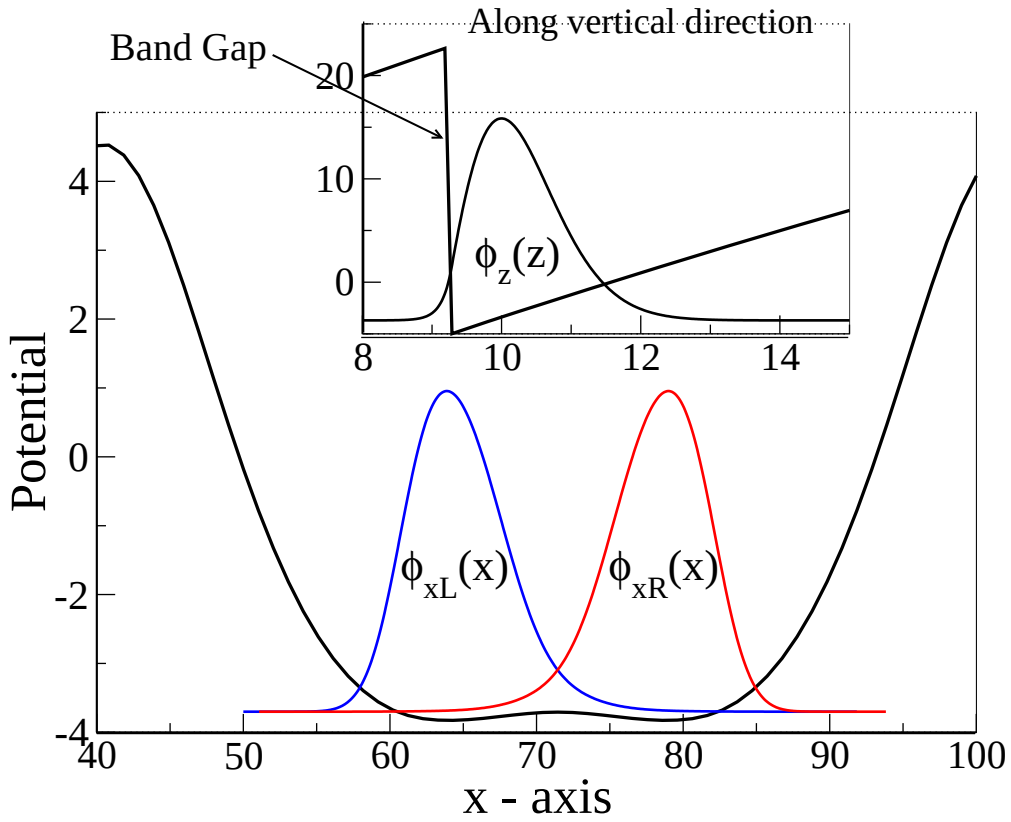

Figure 5.4: The trial functions for the construction of the wave function. Along the x-axis we use splines to interpolate between data points extracted from the LDA solution. Along the z-axis, its a combination of the AiryAi function below (to the right of) the interface and an exponential decay above.

particle orbital is given by

$$Z(z) = \begin{cases} A_0 \exp\left[-\kappa(z - z_I)\right] & \text{if } z < z_I \\ \text{AiryAi}[(2m_{eff}E_z)^{1/3}(z - z_0 - E_L/E_z)] & \text{otherwise} \end{cases}$$

The matching conditions give

$$A_0 = \text{AiryAi}[(2m_{eff}E_z)^{1/3}(z_I - z_0 - E_L/E_z)]$$

κ and E_L are obtained from a self consistent calculation to match the derivative of the function at the boundary z_I.

Both the $Y(y)$ and $Z(z)$ forms depends on adjustable parameters and can be optimized. But our fit was sufficiently good such that these parameters did not vary under optimization. The width

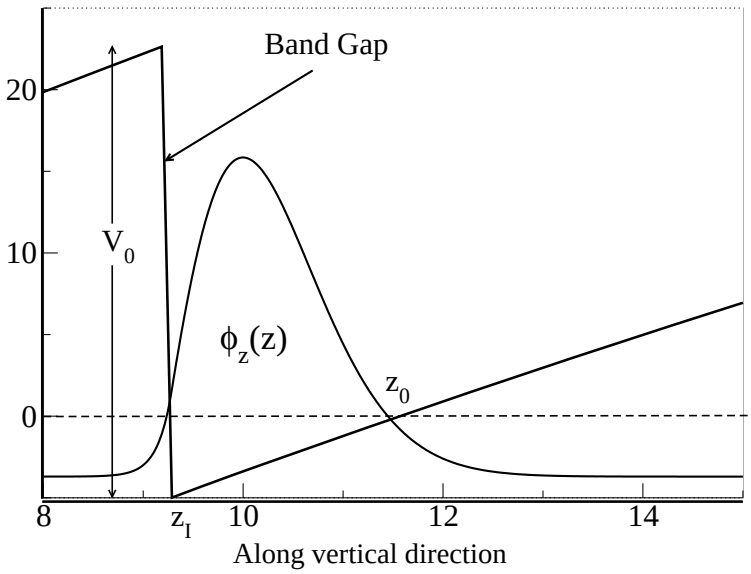

Figure 5.5: Schematic plot of the potential along the vertical direction. V_0, z_I, z_0 and E_z are obtained from the LDA potential.

of the wells and the barrier is controlled by the gate voltages, but the functions did not vary much along these transverse directions, so we used the same parameters for all voltages.

5.5 A Modified Sampling Technique

The heterostructure device is a rectangular structure with planar interfaces between each layer; though the layers have different dielectric functions, within each layer the dielectric is uniform. In order to calculate the potential at any point in the device by employing the WOS algorithm (as described in section 2.4.2), we would have to construct a skin region around each interface. This algorithm would be rather slow since each time to cross over to another layer the walk would have to converge to the interface, hop with some given probability depending on the relative dielectric constants, and continue. Of course we could have used rectangular domains for faster convergence, but then calculating the image potential would have become difficult (as described in section 2.3.1).

In this section we will device a modified sampling technique which will enable us to sample more efficiently, i.e. the walk will converge faster to the external surface. The main idea is as follows. In the basic technique outlined above we construct the spherical domain limited to only one material. This inhibits large step sizes. Instead of this approach we will construct the maximum sphere within

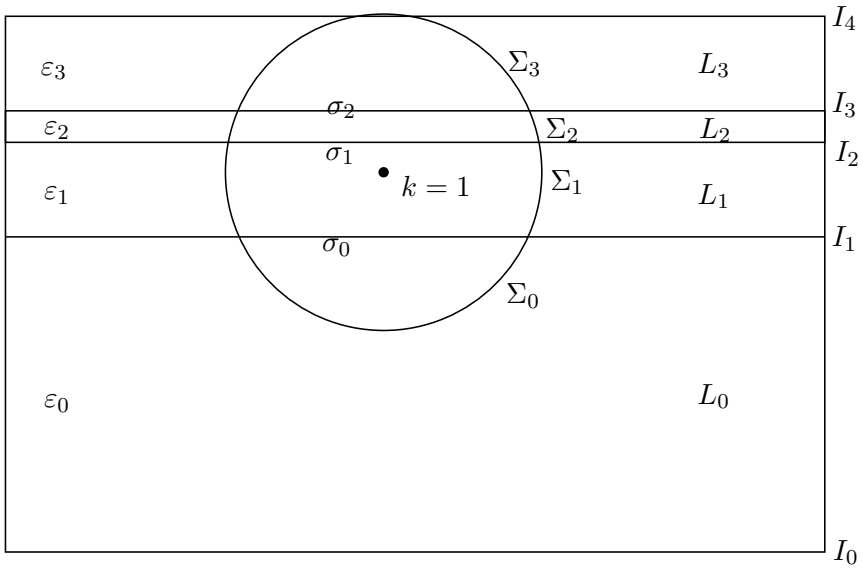

Figure 5.6: A schematic diagram of the quantum dot heterostructure, and labeling the layers and interfaces for the WOS algorithm.

the device which will allow for larger domain radii. But these domains would straddle several layers, and hence the sampling would involve the interfaces as well as the domain surfaces.

The general problem is to obtain the Green's function for the Poisson equation defined in a region of spatially varying dielectric function $\varepsilon(\boldsymbol{r})$. As in section 2.3, we will build the exact Green's function $G(\boldsymbol{R}, \boldsymbol{R}')$ from another Green's function $G_{\mathcal{D}}(\boldsymbol{R}, \boldsymbol{R}')$ which is exact only within the domain $\mathcal{D}$.

$$\nabla \cdot [\varepsilon(\boldsymbol{r})\nabla]\Phi(\boldsymbol{r}) = -\rho(\boldsymbol{r}) \tag{5.8}$$

The Green's functions between two points $\boldsymbol{r}$ and $\boldsymbol{R}_{s+1}$ are defined by

$$\begin{aligned} \nabla \cdot [\varepsilon(\boldsymbol{r})\nabla]G(\boldsymbol{r}, \boldsymbol{R}_{s+1}) &= -\delta(\boldsymbol{r} - \boldsymbol{R}_{s+1}) \qquad G(\boldsymbol{r}, \boldsymbol{R}_{s+1}) = 0, \text{if } \boldsymbol{r} \in \partial\Omega \\ \nabla \cdot [\epsilon_0\nabla]G_{\mathcal{D}}(\boldsymbol{R}_s, \boldsymbol{r}) &= -\delta(\boldsymbol{R}_s - \boldsymbol{r}) \qquad G_{\mathcal{D}}(\boldsymbol{R}_s, \boldsymbol{r}) = 0, \text{if } \boldsymbol{r} \in \partial\mathcal{D} \end{aligned} \tag{5.9}$$

We perform the following mathematical operations on the above and subsequently derived equations. We multiply the above set of equations by $G_{\mathcal{D}}(\boldsymbol{R}_s, \boldsymbol{r})$ and $G(\boldsymbol{r}, \boldsymbol{R}_{s+1})$ respectively, subtract the first from the second and integrate over the entire domain volume $\mathcal{D}$ to obtain an expression for $G(\boldsymbol{R}_s, \boldsymbol{R}_{s+1})$. Using the identity $a\nabla^2 b = \nabla \cdot [a\nabla b] - \nabla a \cdot \nabla b$, Gauss's divergence

theorem and the Dirichlet boundary condition that the Green's functions vanish on the boundaries, we have

$$\begin{aligned} G(\boldsymbol{R}_s, \boldsymbol{R}_{s+1}) = G_{\mathcal{D}}(\boldsymbol{R}_s, \boldsymbol{R}_{s+1}) \quad &+ \quad \int_{\mathcal{D}} d^3r[\epsilon_0 - \varepsilon(\boldsymbol{r})]\nabla G_{\mathcal{D}}(\boldsymbol{R}_s, \boldsymbol{r}) \cdot \nabla G(\boldsymbol{r}, \boldsymbol{R}_{s+1}) \\ &- \quad \epsilon_0 \int_{\partial\mathcal{D}} d^2\boldsymbol{r} \cdot \nabla G_{\mathcal{D}}(\boldsymbol{R}_s, \boldsymbol{r}) G(\boldsymbol{R}_s, \boldsymbol{R}_{s+1}) \end{aligned} \tag{5.10}$$

This result is completely general and holds for any arbitrary domain shape. However for the particular geometry of interest, namely that of the heterostructure device discussed earlier, we can decompose the integrals over each layer of constant dielectric function. Defining $\delta\varepsilon_i = \varepsilon_i - \epsilon_0$, and using the definitions of the Green's function Eq.(5.9) and Gauss's divergence theorem we get

$$\frac{\varepsilon_k}{\epsilon_0} G = G_{\mathcal{D}} - \sum_{i=0}^{N-1} \varepsilon_i \int_{\sigma_i} d^2r\hat{r} \cdot G_{\mathcal{D}} G + \sum_{I=1}^{N-1} \Delta\varepsilon_I \int_{\sigma_I} d^2r\hat{z} \cdot \nabla G_{\mathcal{D}} G \tag{5.11}$$

where the center of the domain $\boldsymbol{R}_s$ lies in the k-th layer. $\Delta\varepsilon_I = \varepsilon_I - \varepsilon_{I+1}$, I being the index of the interfaces. Σ_i denotes the spherical part of the domain surface while σ_i denotes the planar interface within the spherical domain. Consult Fig.(5.6) for labels and indices.

5.5.1 The Spherical Green's function

Considering the domain Green's function for the spherical domain given by Eq.(2.9)

$$G_{\mathcal{D}}(\boldsymbol{R}_s, \boldsymbol{r}) = \frac{1}{4\pi\epsilon_0} \left(\frac{1}{|\boldsymbol{R}_s - \boldsymbol{r}|} - \frac{1}{d_s} \right),$$

where d_s is the radius of the domain. Without loss of generality we can assume $\boldsymbol{R}_s = \boldsymbol{0}$, such that $G_{\mathcal{D}} = (1/4\pi\epsilon_0)(1/r - 1/d_s)$. The gradients on the surfaces, the spherical part on the domain surface, and on the interfaces become

$$\nabla G_{\mathcal{D}}\Big|_{\Sigma} = -\frac{1}{4\pi\epsilon_0} \frac{1}{d_s^2} \hat{r}, \qquad \nabla G_{\mathcal{D}}\Big|_{\sigma} = -\frac{1}{4\pi\epsilon_0} \frac{1}{(d_I^2 + \ell^2)} \hat{r}$$

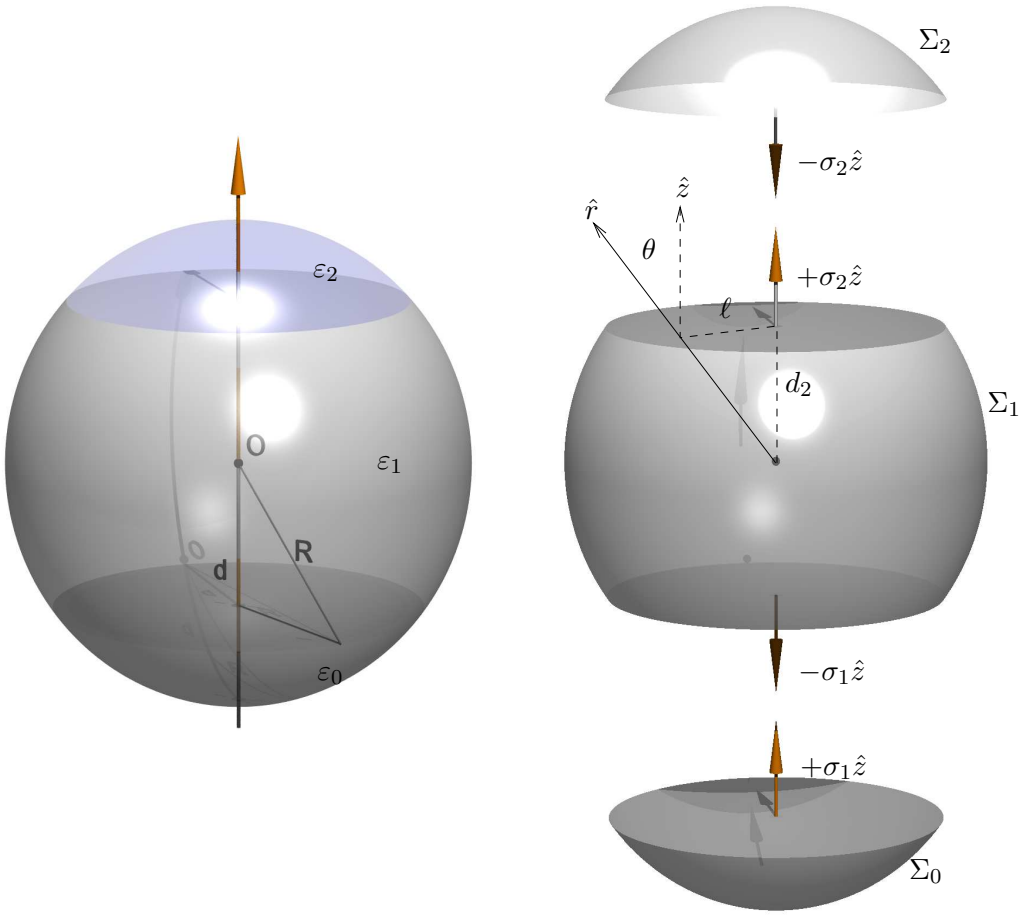

Figure 5.7: Spherical domain straddling several dielectric layers. The domain is divided into two types of surfaces, the spherical surface denoted by Σ_i and the planar-circular disks denoted by σ_i. We note that each surface section can be written as follows. $\boldsymbol{S}_0 = \Sigma_0\hat{r}+\sigma_1\hat{z}$, $\boldsymbol{S}_1 = -\sigma_1\hat{z}+\Sigma_1\hat{r}+\sigma_2\hat{z}$, ...

After some algebra, we get the final sampling equation

$$\begin{aligned} G(\boldsymbol{R}_s, \boldsymbol{R}_{s+1}) = G_{\mathcal{D}}(\boldsymbol{R}_s, \boldsymbol{R}_{s+1}) \quad &+ \quad \sum_{i=0}^{N-1} \frac{\varepsilon_i}{\varepsilon_k} \int_{\theta_{i+1}}^{\theta_i} \sin\theta \frac{d\theta}{2} \int_0^{2\pi} \frac{d\phi}{2\pi} G(\boldsymbol{r}_S, \boldsymbol{R}_{s+1}) \\ &- \quad \sum_{I=1}^{N-1} \frac{\Delta\varepsilon_I}{2\varepsilon_k} \bar{d}_I \int_0^{2\pi} \frac{d\phi}{2\pi} \int_0^{L_I} \frac{\ell d\ell}{(d_I^2 + \ell^2)^{3/2}} G(\boldsymbol{r}_I, \boldsymbol{R}_{s+1}) \end{aligned} \quad (5.12)$$

where $\boldsymbol{r}_S(d_s, \theta, \phi)$ is a point on the surface of the spherical domain, and $\boldsymbol{r}_I(\ell, \phi, z_I)$ (in cylindrical coordinates) is a point on the I-th interface. And $\bar{d}_I = z_I - R_{sz}$. The problem now is reduced to sampling this expression.

5.5.2 Sampling the Green's function

A method to sample expressions of the form of Eq.(5.12) is given in Appendix A.7. Here we lay out the steps of the algorithm, for details refer to the Appendix. As usual the random walk starts from the point we need to evaluate the potential at. A maximum sphere is constructed centered at this point. This sphere will in general straddle several dielectric layers as described above. The probabilities of sampling each section of the surfaces are calculated from the following formulae. For each spherical surface-section Σ_i compute

$$\mathcal{N}_i^{(1)} = \frac{1}{2}\frac{\varepsilon_i}{\varepsilon_k}\frac{\bar{d}_{i+1} - \bar{d}_i}{d_s} \quad \forall\, i = 0, \ldots, N-1$$

and for each of the planar interface section σ_i compute

$$\mathcal{N}_I^{(2)} = \frac{1}{2}\frac{\Delta\varepsilon_I}{\varepsilon_k}\frac{1 - d_I/d_s}{d_I} \quad \forall\, I = 1, \ldots, N-1$$

These are summed to obtain the total weight

$$\mathcal{N} = \sum_i^{N-1} \mathcal{N}_i^{(1)} + \sum_{I=1}^{N-1} \mathcal{N}_I^{(2)} = \sum_i^{N-1} \frac{1}{2}\frac{\varepsilon_i}{\varepsilon_k}\frac{\bar{d}_{i+1} - \bar{d}_i}{d_s} + \sum_{I=1}^{N-1} \frac{1}{2}\frac{\Delta\varepsilon_I}{\varepsilon_k}\frac{1 - d_I/d_s}{d_I}$$

and we define the normalized probabilities

$$n_i^{(1)} = \mathcal{N}_i^{(1)}/\mathcal{N} \qquad \text{and} \qquad n_I^{(2)} = \mathcal{N}_I^{(2)}/\mathcal{N}$$

and these are the associated probabilities of sampling each of the surface segments Σ_is and σ_Is.

A uniform random number is drawn $\xi \in (0, 1]$, and according to the above probabilities we decide which surface segment is to be sampled. If it is one of the spherical segments, we sample a point on that section according to the density

$$w_i^{(1)} = \frac{1}{2\pi}\frac{d_s}{\bar{d}_{i=1} - \bar{d}_i}\sin\theta$$

otherwise if it is on the interface segments, then we sample a point on the circular disc according

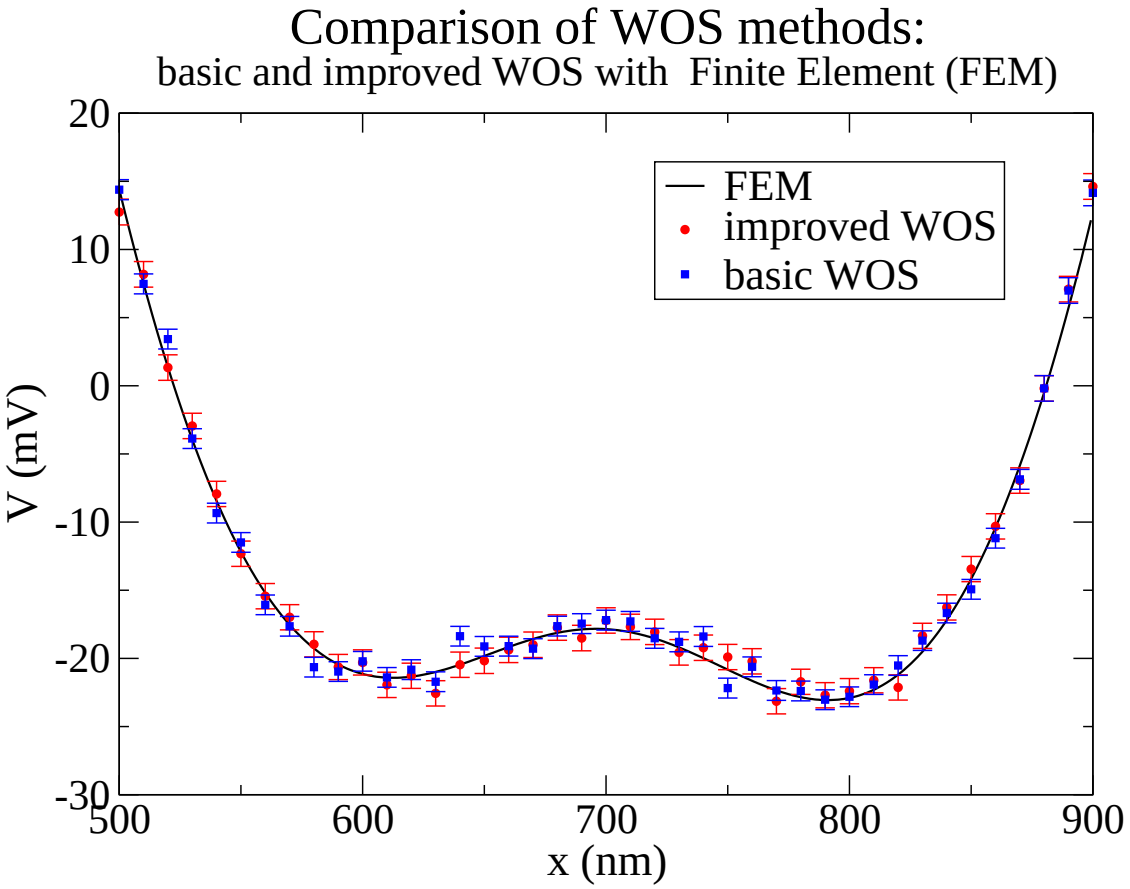

Figure 5.8: Comparison of the potential obtained from finite element calculation with that obtained from WOS calculations. Both the basic and the improved algorithm employed 10^6 walks to estimate the potential, however the improved algorithm was about seven times faster. This graph is generated for comparison purposes, during the QMC-WOS calculation the main idea is to avoid the construction of this potential surface. Also note that though belonging to the same heterostructure, this potential profile was obtained for a different gate bias configuration than that used for the singlet-triplet calculations.

to the density

$$w_I^{(2)}(\ell,\phi) = \frac{1}{2\pi}\frac{d_I}{1-d_I/d_s}\frac{\ell}{(d_I^2+\ell^2)^{3/2}}$$

If the interface section σ_I is sampled then sign$[-\Delta\varepsilon_I \bar{d}_I]$ is accumulated for the wight. This introduces a sign problem as discussed in Appendix A.7.

From then on the walk repeats itself until convergence on the external surface where the applied potential is sampled with the appropriate weight accumulated along the path. All other considerations are same as that of the basic WOS algorithm described in chapter 2.

5.6 Singlet-Triplet Splitting

Singlet-triplet splitting in the double dot structure is an important characteristic to study beacause of potential applications in quantum computing. For operational purposes the register of a quantum computer needs to be initialized, i.e. all the spins have to be aligned (up or down). But the ground state of a two electron system for a local Hamiltonian is guaranteed to be a singlet by the Perron-Frobenius theorem [16]. Hence, to carry out quantum computation by means of this double dot structure, we need to induce a singlet to triplet transition by manipulating the bias of the surface gates (namely PL and PR in Fig.(5.1)). This can be accomplished by tuning the gates such that the singlet and triplet are degenerate. The goal of the simulations is to determine the corresponding bias configuration.

The operational configuration of the device was as follows: (referring to Fig.(5.1) QPC-L,QPC-R at -0.7V, L,R at -0.7V, and T,M at -0.5V. The sweeping voltage is the bias applied to gates PL and PR, they are both at the same voltage.

DFT calculations (obtained from the CEG group [49]) as described in section 5.2 are shown in Fig.(5.9). The problem with the calculation is that in the range $-0.5V$ to $-0.9V$, the gap is negative, i.e. triplet is lower than singlet, an unphysical result. Hence the need for more accurate QMC calculations. The DFT solution provides a good starting point for construction of the trial wave-functions, but the functions obtained from the above calculations were not sufficinetly smooth at small values, (showed oscillations at $\mathcal{O}(10^{-8})$ times the peak value). This is negligiible for integration schemes, but QMC uses the gradient of the wave-function and this is problematic especially since the region of oscillation is very close to the peak of the wave-function.

Trial wave-functions as described in section 5.4 were used. DMC calculations using the Hamiltonian in Eq.(5.2) showed a gap (shown in blue in Fig.(5.9)) about double of that obtained using DFT , but the gap remained positive as required from theoretical considerations [16]. Fig.(5.9) shows that the double well coalesces into a single well as the magnitude of the gate bias increases; the barrier vanishes at around a bias of $-1.5V$. In literature [73] this gap has been estimated by Hartree-Fock methods to be around 0.4 meV for a two center 2D oscillator dot model. Given the difference in geometry, our result of about 0.7 meV is reasonable.

The above calculation used the converged potential solution from the DFT calculations as a

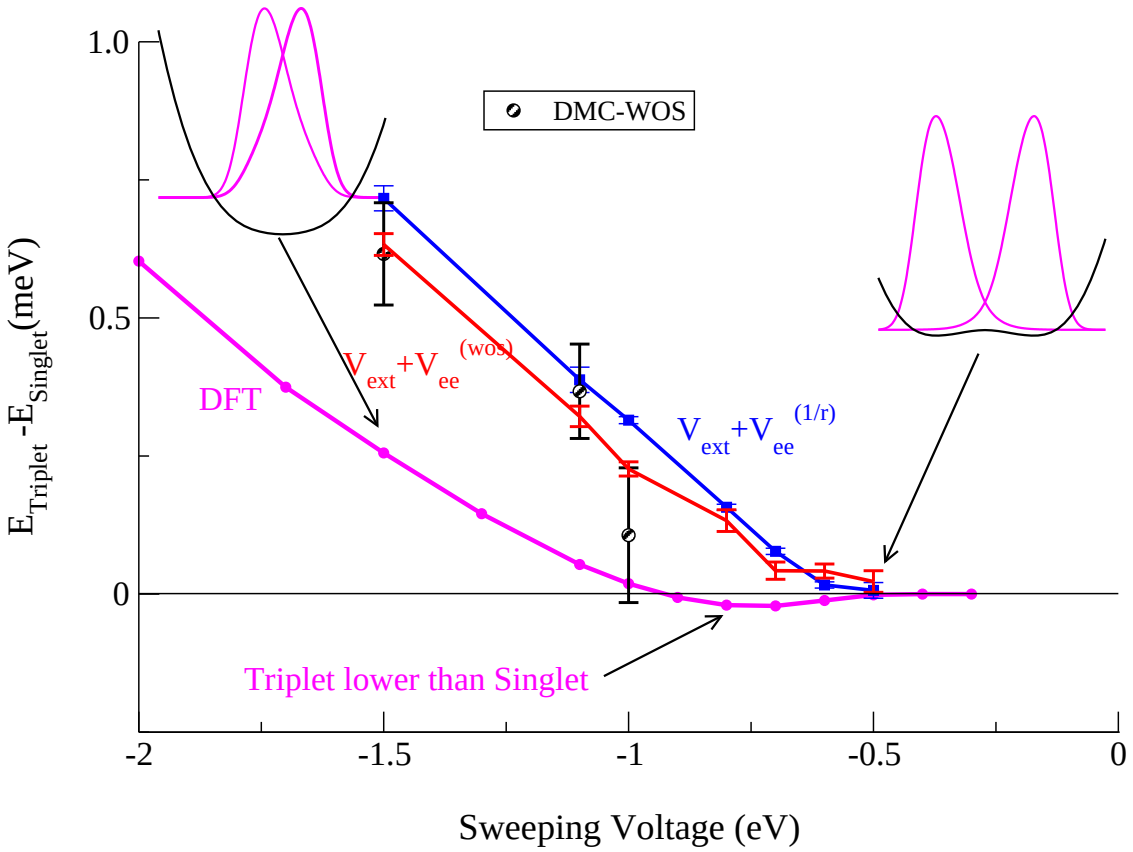

Figure 5.9: The singlet-triplet splitting curves with respect to the sweeping voltage i.e. the bias in the gates PL and PR in Fig.(5.1). The DFT gap goes becomes negative at small bias, i.e. the singlet higher than triplet. But the DMC result shows that the gap always remains positive. In blue is the DMC result where the electronic interaction is taken to be $1/\epsilon r$. In red is another DMC calculation, where only the electronic interaction is computed by WOS. The green dots are from a full WOS calculation. The DFT data was provided by the Computational Electronics Group (CEG) [49].

rigid external potential V_{ext}, but the total potential energy can be calculated using WOS. The data points marked DMC-WOS in Fig.(5.9) show the gap obtained by using the Hamiltonian of Eq.(5.3). This takes into account the full electronic interaction while infering the external potential from boundary conditions. However, this poses some difficulties. Each of the points in Fig.(5.8) took about 5 million runs to estimate. Hence to have a reasonable estimate of the variance to use in the branching of DMC we still need a very large number of runs. As seen from Table (5.2), we used only 200 runners per walker and still this was extremely slow leading to a very large variance in the estimate.

The DMC calculation is expensive primarily due to the non-linear branching term, so a reason-

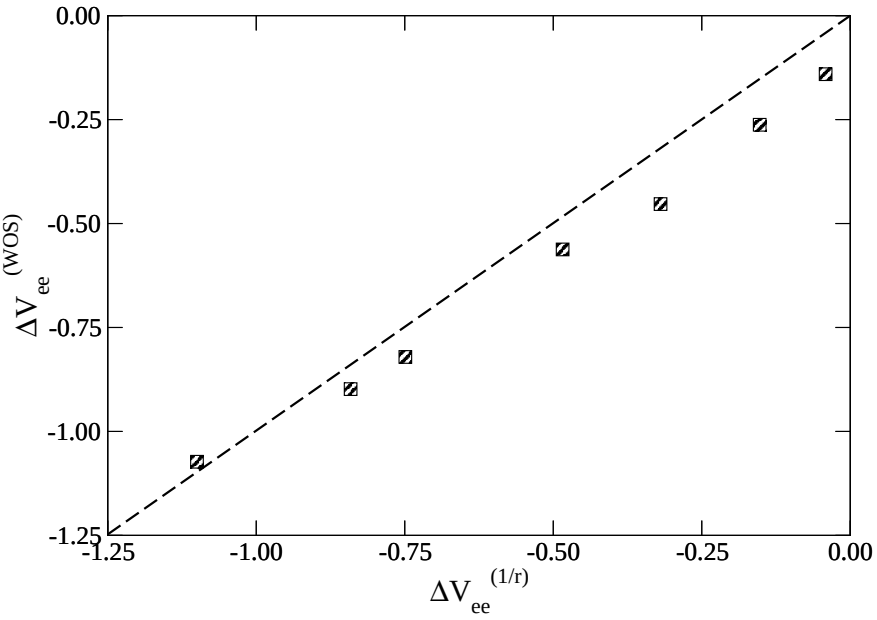

Figure 5.10: Comparison between the gap in the two interactions, $V = 1/\epsilon r$ and $V_{\rm wos}$. The plotted quantity along either axis is the difference of triplet - singlet electronic interaction.The units are in eV.

ably accurate estimate of the branching term will allow the use of WOS to account for the correct electronic interaction. Consider a potential $V = V_{\rm ext} + V_{\rm ee}^{(1/r)}$, constructed from the external potential and a $1/\epsilon r$ interaction as used for the previous DMC calculation. A calculation using this energy to branch and use $V = V_{\rm WOS}$ as the estimator for potential energy will show the same convergence properties as the previous calculation.

We however take a slightly different approach. The physics of the potential essentially consists of two parts, the external potential and the electronic interaction. Though the external potential can be infered by WOS from the boundary conditions, this is the main contribution to the variance. Hence, using a potential of the form $V = V_{\rm ext} + V_{\rm ee}^{(\rm wos)}$, where only the electronic interaction is calculated by WOS would have much better convergence than the full DMC-WOS calculation. The assumption which makes this calculation work is that the electrons do not significantly modify the environment which remains fixed, it is only the image charges which react instantly to variations in the electronic density and hence modify the interaction. This calculation is shown in red in Fig.(5.9).

To understand the effect of the electronic interaction we next compare the electronic interaction

Potential type	Walkers	Runners /Walker	Steps	Blocks	Time/Block (sec)	Processors	Total Time (hrs)
$V_{\text{ext}} + 1/r$	10^3	–	$2 \cdot 10^2$	10^3	1.02	8	2.26
$V_{\text{ext}} + V_{\text{WOS}}^{\text{ee}}$	10^3	5	$2 \cdot 10^2$	10^3	10.81	8	24.01
V_{WOS}	$2 \cdot 10^2$	$2 \cdot 10^2$	10^2	50	$3 \cdot 10^3$	8	335

Table 5.2: A comparison of run times for calcualtion. The first row denotes the calculation using the external potential with the $1/r$ interaction. The second row denotes the calculations using the external potential but with the interaction calculated by the WOS method. The last row denotes the calculations where the entire potential is calculated by the WOS method. As seen from the numbers, the full DMC-WOS calculation is extremely time consuming

of the two calculations in Fig(5.10). We plot the difference of the singlet and triplet $1/\epsilon r$ interaction along the x-axis and the same for $V_{\text{ee}}^{(wos)}$ along the y-axis. In other words, we plot the quantities

$$V_{\text{ee}}^{\text{triplet}}(1/r) - V_{\text{ee}}^{\text{singlet}}(1/r), \qquad \text{and} \qquad V_{\text{ee}}^{\text{triplet}}(\text{wos}) - V_{\text{ee}}^{\text{singlet}}(\text{wos}).$$

So this is the difference in the contribution of the electronic interactions and not the difference in the total energy which is shown in Fig.(5.9).

If the two contributions were identical, then they would lie on the dashed line. However, we see that the magnitude of the difference of the interaction when calculated by WOS is slightly smaller than that when computed by the $1/\epsilon r$ model because of the induced charge effects.

Also note that the difference in the interactions are negative. This is because in the singlet the electrons have opposite spin, and hence are closer together, and hence the interaction energy is higher than in the triplet where the same spin keeps the electrons apart.

The calculations were performed on the NCSA Tungsten cluster which is a dual processor Dell PowerEdge 1750 server with 3GB ECC DDR SDRAM memory with 1280 compute nodes and Intel Xeon 3.2 GHz(32-bit) processors.

Chapter 6

Conclusions

The main conclusions of this thesis has been the following

1. We have implemented quantum Monte Carlo calculations where the potential is computed simultaneously by another Monte Carlo algorithm. We have adapted the "Walk On Spheres" algorithm for the purpose of stochastically solving the Poisson equation. In this thesis we have laid out the principles behind the algorithm and further adapted it to suit different device geometries and dielectric media.

2. We have demonstrated the compatibility of the two Monte Carlo methods by studying a toy problem, that of measuring the polarizability of helium atom, by placing it within the plates of an infinite capacitor. We have also adapted and modified the penalty method to allow diffusion Monte Carlo to accept the stochastic potential.

3. We have performed Monte Carlo calculations on a realistic model obtained from the Computational Electronics Group [49]. We have used their DFT solutions as input to the QMC calculation, and found the singlet-triplet gap to remain positive even at low bias.

4. We have demonstrated the general applicability of this method by applying it to a realistic model of a semiconductor heterostructure. Different algorithms can be developed to improve efficiency. We have measured the singlet-triplet splitting of the laterally coupled double quantum dot for two electron occupancy. We have carried out this measurement in several ways. Firstly, using the external potential with an $1/r$ inter-electronic interaction. Secondly, by the full QMC-WOS method, and finally using the external potential, but evaluating the electronic interaction by WOS.

5. We found that the completely generic model can become very expensive. Better results can be obtained if we use the confining potential but compute the modified electronic interaction by WOS.

6. We conclude that this method has great potential to be useful in systems where the dielectric mismatch plays an important role, like spherical quantum dots. For feasibility of calculations it is also important to have a good approximation to the wave-function, since otherwise the variational calculations are not reliable.

Appendix A

Sampling Distributions

A.1 Probability: definitions

Much of the material in the following sections can be found in [39]. We present them here for completeness and to facilitate understanding of the sampling methods extensively used in the algorithms discussed in this thesis.

Given an event with a countable set of random outcomes $\{E\} \equiv \{E_1, E_2, \dots, \}$ there is associated with each possible outcome E_i a positive number called *probability*, p_i, i.e. $\mathbb{P}(E_i) = p_i$, which must lie in the range

$$0 \leq p_i \leq 1 \quad \forall\, i$$

If the k-th event never occurs, $p_i = 0$, if it is sure to occur $p_i = 1$. If the set $\{E_i\}$ is exhaustive, then $\sum p_i = 1$, i.e. at least one of the k events is bound to occur. This property is called *normalization*.

In the following we shall assume that for every outcome E_i, there is a real number x_i which can be called a random variable. The expectation of this random variable x, i.e. the stochastic mean value is defines as

$$\mathbb{E}(x) = \sum_i p_i x_i \equiv \langle x \rangle \equiv \mu$$

and the variance is given by

$$\mathrm{var}\{x\} = \langle (x - \mu)^2 \rangle = \langle x^2 \rangle - \langle x \rangle^2.$$

The square root of the variance is a measure of the dispersion of the random variable, this is

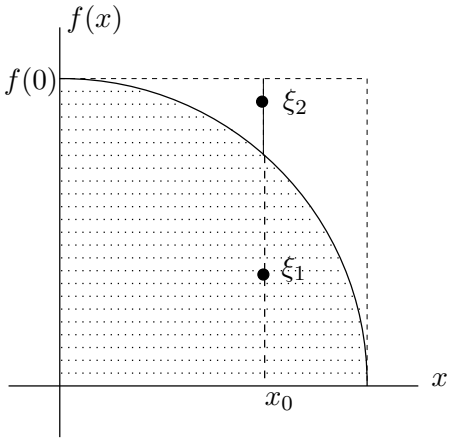

Figure A.1: The rejection technique. ξ_1 is accepted and ξ_2 is rejected.

also called the *standard deviation*. These discussions can be carried over from the discrete to the continuous case where the sums are simply replaced by integrals.

A.2 Methods of Sampling Standard Distributions

We will take it for granted that there exists codes to generate pseudo-random numbers uniformly distributed in the range $(0, 1]$. Given this our task is to generate a set of random numbers $\{x_i\}$ distributed according to $f(x)$. We will deal primarily with one dimensional distributions for which this means

$$\mathbb{P}\{x_k \in (a, b)\} = \int_a^b f(x)dx, \qquad 0 < a < b < 1$$

We will discuss only two methods of sampling, rejection and transformation.

A.2.1 Rejection

The idea behind the rejection technique is very simple, a trial value x_0 for a random variable x is selected and proposed. This value is subjected to one or more tests, and it maybe accepted, that is used as needed, or rejected. The test is accomplished by accepting x_0 with probability proportional to $f(x_0)$. For the distribution in Fig.(A.1), after the trial point x_0 is proposed, a random number $\xi \in (0, 1]$ is sampled. x_0 is accepted if $\xi \leq f(x_0/f(0)$ for the function in Fig.(A.1), and rejected otherwise.

If it is rejected, the cycle of choosing and testing a trial value is repeated until an acceptance

takes place. An important property of this technique is that the normalization of the density need not be known explicitly to carry out the sampling. The difficulty is that if a large number of trials are rejected, then the method become extremely inefficient.

A.2.2 Transformation of Random Variables

Suppose that x, $(x_i < x < x_f)$ is a random variable with a probability density function (pdf) $f_X(x)$ $(\int_{x_i}^{x_f} f_X(x)dx = 1)$and a cumulative distribution function (cdf) given by

$$F_X(x) = \int_{x_i}^{x} f_X(x)dx$$

and that $y \equiv y(x)$ is a continuous non-decreasing function of x. The question is, what is $F_Y(y)$? The variable x and the function $y(x)$ map into each other

$$y(X) \leq y(x) \quad \text{iff } X \leq x$$

so the probabilities become

$$\mathbb{P}\{y(X) = Y \leq y(x)\} = \mathbb{P}\{X \leq x\}$$

or

$$F_Y(y) = F_X(x) \quad \text{where } y = y(x).$$

The relationship between the probability distribution functions maybe determined by differentiating the above equation

$$f_Y(y)\frac{dy}{dx} = f_X(x)$$

If $y(x)$ is a non-increasing function of x, then

$$\mathbb{P}\{y(X) = y(x)\} = \mathbb{P}\{X \geq x\} = 1 - \mathbb{P}\{X < x\}$$

since

$$\mathbb{P}\{X \geq x\} + \mathbb{P}\{X < x\} = 1.$$

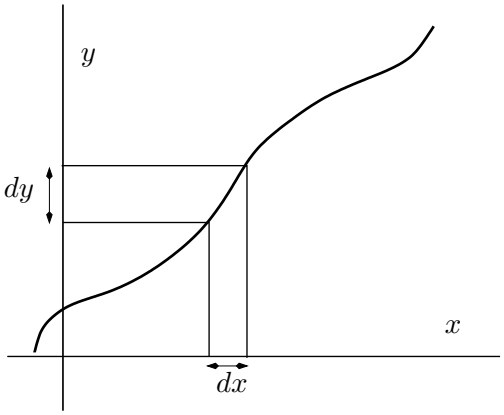

Figure A.2: The cumulative distribution function.

The c.d.f. for y is therefore

$$F_Y(y) = 1 - F_X(x)$$

and

$$f_Y(y)\frac{dy}{dx} = -f_X(x)$$

These can be combined to state

$$|f_X(x)dx| = |f_Y(y)dy|$$

reflecting the fact that all the values of x in dx map into values of y in dy.

Now, if ξ is uniform, its cdf is

$$F_\xi(\xi) = \begin{cases} 0, & \xi < 0 \\ \xi, & 0 \leq \xi \leq 1 \\ 1, & \xi \geq 1 \end{cases}$$

Therefore on $(0, 1]$ the cdf for y is determined by solving the equation

$$F_Y(y) = \xi$$

We will be using this equation repeatedly.

A.3 Sampling a Normal Distribution

A normal variable with mean zero and variance one, denoted by $N(0,1)$, is distributed according to

$$\varphi(x|0,1) = \frac{1}{\sqrt{2\pi}} \exp\left(-\frac{1}{2}x^2\right), \qquad -\infty < x < \infty \tag{A.1}$$

A variable distributed according to $N(\mu, \sigma^2)$ is obtained easily from

$$\varphi(x|\mu,\sigma^2) = \mu + \sigma\varphi(x|0,1)$$

Hence it is sufficient to demonstrate methods of generating standard normal variates, i.e. variables distributed according to $N(0,1)$.

Consider another variable y distributed normally according to Eq.(A.1), and multiply this to the distribution for x to obtain

$$\varphi(x)\varphi(y)dxdy = \frac{1}{2\pi}\exp\left(-\frac{x^2+y^2}{2}\right)dxdy = \left[\exp\left(-\frac{1}{2}r^2\right)rdr\right]\left[\frac{d\phi}{2\pi}\right]$$

where we have transformed the variables to polar cöordinate r and ϕ where $0 \le r < \infty$ and $0 \le \phi \le 2\pi$. We note in passing that the integral $\int_0^\infty \exp[-r^2/2]rdr = 1$, and hence both the expressions with square brackets in the above equation can be considered as probability densities.

So two independent random numbers distributed normally can be obtained simultaneously as follows. Draw two random numbers ξ_1 and ξ_2, $\xi \in (0,1]$. Set $\phi = 2\pi\xi_2$, thus sampling ϕ uniformly in the range $(0, 2\pi]$.

For the expression in r, the cumulative distribution function is given by

$$F_R(r) = \int_0^r \exp[-u^2/2]udu = 1 - \exp[-r^2/2] = \xi$$

Inverting the equation,

$$r = [-2\log(1-\xi)]^{1/2} \equiv [-2\log\xi_1]^{1/2}$$

since both ξ and $1-\xi$ are distributed uniformly in $(0,1]$. Putting it all together

$$\begin{aligned} x &= [-2\log\xi_1]^{1/2}\cos(2\pi\xi_2) \\ y &= [-2\log\xi_1]^{1/2}\sin(2\pi\xi_2). \end{aligned}$$

this is known as the *Box-Muller* method, though this was first invented by Wiener.

An approximate normal random variable may also be generated by invoking the central limit theorem. By sampling N uniform random variables $\xi_1, \xi_2, \ldots, \xi_N$ and forming the sum

$$x = \sqrt{\frac{12}{N}}\left(\sum_{k=1}^{N}\xi_k - \frac{N}{2}\right)$$

a variable of mean zero and variance one is generated. The central limit theorem asserts that this will be nearly normal for large N. A value of $N = 12$ appears to be sufficiently large for many purposes and avoids the evaluation of the factor $\sqrt{12/N}$.

A.4 Sampling Uniformly on a Spherical Surface

Given a point $P(x,y,z)$ we want to uniformly sample a point P' on the surface of a sphere of radius d centered at P. This can be done in two different ways. The simplest approach is to look at the normalized differential form

$$\left[\frac{\sin\theta}{2}d\theta\right]\left[\frac{d\phi}{2\pi}\right]$$

hence we sample ϕ uniformly in the range $(0, 2\pi]$ as described before. For θ the cumulative distribution function is given by

$$F_\Theta(\theta) = \int_0^\theta \frac{\sin\theta}{2}d\theta = \frac{1}{2}(1-\cos\theta) = \xi$$

inverting the equation

$$\cos\theta = 1 - 2\xi$$

The new point can be generated as follows

$$\begin{aligned} P'(x) &= P(x) + 2d\sqrt{\xi_1(1-\xi_1)}\cos[2\pi\xi_2] \\ P'(y) &= P(y) + 2d\sqrt{\xi_1(1-\xi_1)}\sin[2\pi\xi_2] \\ P'(z) &= P(z) + d(1-2\xi_1) \end{aligned}$$

Another simple way of generating points uniformly on the surface of a sphere is suggested by Muller [54]. Construct a vector $\boldsymbol{a} = (X_1, X_2, X_3)$ where $X \in N(0,1)$. Normalize the vector, i.e. $\boldsymbol{a}/a$ where $a = |\boldsymbol{a}|$. Scale it up to the length of the radius of the sphere, i.e. $d\boldsymbol{a}/a$.

$$\boldsymbol{P'} = \boldsymbol{P} + d\boldsymbol{a}/a$$

is distributed uniformly on the surface of the sphere of radius d centered at $\boldsymbol{P}$.

A.5 Monte Carlo Integration

If we want to evaluate an integral of the form

$$G = \int g(X) f(X) dX$$

where

$$f(X) \geq 0, \qquad \int f(x) dX = 1$$

then the following *game of chance* may be used to make numerical estimates. We draw variables $X_1, X_2, \ldots, X_N$ from $f(X)$ and form the arithmetic mean

$$G_N = \frac{1}{N} \sum_i g(X_i)$$

A.6 Variance Reduction: Importance Sampling

Suppose we have an n-dimensional integral

$$G = \int g(X) f(X) dX$$

that we wish to evaluate. The function $f(X)$ is not necessarily the pdf to use in a Monte Carlo calculation even though it appears in the integrand. A different pdf, $\tilde{f}(X)$ can be introduced into the integral as follows:

$$G = \int \left[\frac{g(X) f(X)}{\tilde{f}(X)} \right] \tilde{f}(X) dX$$

where

$$\tilde{f}(x) \geq 0, \qquad \int \tilde{f}(X) dX = 1$$

and $g(X)f(X)/\tilde{f}(X) < \infty$ except perhaps on a (countable) set of points. The variance is minimized when

$$\tilde{f}(X) = \frac{g(X) f(X)}{G},$$

i.e. if we already know the correct answer G, the Monte Carlo calculation will certainly give it back with zero variance! This corresponds to the minimum variance calculation. Although in practice we can not use $\tilde{f}(X)$ as prescribed above, we expect that "similar" functions will reduce the variance.

A.7 Sampling a Sum of Terms

To understand how to sample a complicated expression like Eq.(5.12) we study a few simple examples.

Example 1. Consider the following expression

$$T = W_1 A_1 + W_2 A_2 - W_3 A_3, \qquad A_i, W_i > 0, \forall i$$

We want to sample T, by sampling the A_i terms. Define the following

$$\mathcal{N} = \sum W_i \qquad w_i = W_i / \mathcal{N} \qquad A_i' = \mathcal{N} A_i$$

Thus,

$$T = w_1(A'_1) + w_2(A'_2) + w_1(-A'_3)$$

now the w_is can be treated as normalized probabilities ($\sum w_i = 1$). Pick a uniform random number ξ, $\xi \in (0, 1]$, if $\xi < w_1$, sample A'_1, else if $\xi < (w_1 + w_2)$, sample A'_2, else sample $-A'_3$. Averaging over many such samples will give an estimate of T. Generalization to larger number of terms is obvious.

A Sign Problem

The error in the estimate of T suffers from the sign problem, due to the negative sign in front of the W_3A_3 term. This is seen from the variance of the sampling.

$$\text{var}[T] = \langle T^2 \rangle - \langle T \rangle^2; \qquad \text{where } \langle T^2 \rangle = w_1 A'^2_1 + w_2 A'^2_2 + w_3 A'^2_3$$

Thus,

$$\begin{aligned}\text{var}[T] &= [w_1 A'^2_1 + w_2 A'^2_2 + w_3 A'^2_3] - [w_1 A'_1 + w_2 A'_2 - w_3 A'_3]^2 \\ &= w_1(1 - w_1)A'^2_1 + w_2(1 - w_2)A'^2_2 + w_3(1 - w_3)A'^2_3 - 2w_1 w_2 A'_1 A'_2 \\ &\qquad + 2w_3 A'_3[w_1 A'_1 + w_2 A'_2]\end{aligned}$$

Note that $0 < w_i < 1$. The negative contribution from A_3 in T leads to the last positive term in the above expression which leads to a higher variance, hence larger error in the estimate. This is the sign problem, if the negative contribution is large, the signal will disappear in the noise. Thus to sample T efficiently we need $w_3 \ll 1$.

Example 2. Now suppose that each term is itself an integral

$$T = \sum_i \int_{L_i} dx \; S_i W_i(x) A_i(x) \tag{A.2}$$

where S_i is the sign of the term i.e. ± 1, and each integral is over a different interval. Sampling of this expression proceeds exactly as above. Define the following

$$\mathcal{N}_i = \int_{L_i} dx W_i(x), \quad \mathcal{N} = \sum_i \mathcal{N}_i, \quad n_i = \mathcal{N}_i/\mathcal{N}, \quad w_i = W_i/\mathcal{N}_i, \quad A_i'(x) = \mathcal{N} S_i A_i(x)$$

Thus,

$$T = \sum_i n_i \int_{L_i} dx \; w_i(x)[S_i A_i'(x)] = \sum_i n_i T_i$$

Now, the n_is are normalized by construction, i.e. $\sum n_i = 1$, and hence can be used as probabilities. Just as in the previous example, we draw a random number ξ, to decide which term T_i to sample. Then its simply a matter of sampling x_k for the normalized distribution $w_i(x)$, and collecting the term $S_i A_i'(x_k)$.

A.8 Sampling Eq.(5.12).

Sampling of this equation proceeds along the ideas mentioned above. The first step is to calculate the N_i like terms,

$$\begin{aligned}\mathcal{N}_i^{(1)} = \frac{\varepsilon_i}{\varepsilon_k} \int_{\theta_{i+1}}^{\theta_i} \sin\theta \frac{d\theta}{2} \int_0^{2\pi} \frac{d\phi}{2\pi} &= \frac{1}{2}\frac{\varepsilon_i}{\varepsilon_k}(\cos\theta_{i+1} - \cos\theta_i), \quad \forall\ i = 0, \ldots, N-1 \\ &= \frac{1}{2}\frac{\varepsilon_i}{\varepsilon_k}\frac{\bar{d}_{i+1} - \bar{d}_i}{d_s}\end{aligned}$$

and,

$$\begin{aligned}\mathcal{N}_I^{(2)} &= \frac{1}{2}\frac{\Delta\varepsilon_I}{\varepsilon_k}\bar{d}_I \int_0^{2\pi} \frac{d\phi}{2\pi} \int_0^{L_I} \frac{\ell d\ell}{(d_I^2 + \ell^2)^{3/2}}; \quad L_I = \sqrt{d_s^2 - d_I^2}, \quad \forall\ I = 1, \ldots, N-1 \\ &= \frac{1}{2}\frac{\Delta\varepsilon_I}{\varepsilon_k}\bar{d}_I \left[\frac{1}{2}\int_{d_I^2}^{d_s^2} \frac{d\alpha}{\alpha^{3/2}}\right], \quad \text{where } \alpha = d_I^2 + \ell^2 \\ &= \frac{1}{2}\frac{\Delta\varepsilon_I}{\varepsilon_k}\bar{d}_I \left[\frac{1}{\sqrt{\alpha}}\right]_{d_s}^{d_I} \quad = \frac{1}{2}\frac{\Delta\varepsilon_I}{\varepsilon_k}\bar{d}_I \frac{1 - d_I/d_s}{d_I}\end{aligned}$$

Thus the total weight becomes

$$\mathcal{N} = \sum_{i=0}^{N-1} \frac{1}{2}\frac{\varepsilon_i}{\varepsilon_k}\frac{\bar{d}_{i+1} - \bar{d}_i}{d_s} + \sum_{I=1}^{N-1} \frac{1}{2}\frac{\Delta\varepsilon_I}{\varepsilon_k}\bar{d}_I \frac{1 - d_I/d_s}{d_I}$$

As before define $n_i^{(1)} = \mathcal{N}_i^{(1)}/\mathcal{N}$ etc., and

$$w_i^{(1)}(\theta,\phi) = \frac{d_s}{\bar{d}_{i+1}-\bar{d}_i}\frac{1}{2\pi}\sin\theta, \qquad w_I^{(2)}(\ell,\phi) = \frac{1}{2\pi}\frac{d_I}{1-d_I/d_s}\frac{\ell}{(d_I^2+\ell^2)^{3/2}}$$

Hence Eq.(5.12) is reduced to the form

$$\begin{aligned} G(\boldsymbol{r},\boldsymbol{R}_{s+1}) = G_{\mathcal{D}}(\boldsymbol{R}_s,\boldsymbol{r}) &+ \sum_{i=0}^{N-1} n_i^{(1)} \int_{\theta_{i+1}}^{\theta_i} d\theta \int_0^{2\pi} d\phi\ w_i^{(1)}(\theta,\phi)[S_i\mathcal{N}G(\boldsymbol{r}_s,\boldsymbol{R}_{s+1})] \\ &+ \sum_{I=1}^{N-1} n_I^{(2)} \int_0^{L_I} d\ell \int_0^{2\pi} d\phi\ w_I^{(2)}(\ell,\phi)[S_I\mathcal{N}G(\boldsymbol{r}_I,\boldsymbol{R}_{s+1})] \end{aligned} \tag{A.3}$$

where $S_i = 1,\ \forall\ i$, and $S_I = \text{sign}[-\Delta\varepsilon_I\bar{d}_I]$. So we just need to know how to sample the w_is. We note that for either of the ws the ϕ dependence is rather simple.

$$\begin{aligned} 1 &= \int w_i(\beta,\phi)d\beta d\phi, \qquad \beta = \text{either } \theta \text{ or } \ell \\ &= \int_\beta \omega_i(\beta)d\beta \int_0^{2\pi}\frac{d\phi}{2\pi}, \qquad \omega_i(\beta) = w_i(\beta,\phi)/2\pi \end{aligned}$$

This implies that we can simply sample ϕ uniformly between 0 and 2π, i.e. sample a random number $\xi \in (0,1]$, and $\phi = 2\pi\xi$.

So we need to sample from the p.d.f. $\omega_i(\theta)$. We know

$$\frac{d_s}{\bar{d}_{i+1}-\bar{d}_i}\int_{\theta_{i+1}}^{\theta_i}\sin\theta d\theta = 1$$

We can sample θ from this by solving

$$\frac{d_s}{\bar{d}_{i+1}-\bar{d}_i}\int_{\theta_{i+1}}^{\theta}\sin\theta d\theta = \xi$$

or,

$$\frac{d_s}{\bar{d}_{i+1}-\bar{d}_i}\int_{\cos\theta}^{\bar{d}_{i+1}/d_s} d[\cos\theta] = \frac{d_s}{\bar{d}_{i+1}-\bar{d}_i}\left[\frac{\bar{d}_{i+1}}{d_s}-\cos\theta\right] = \xi$$

solving

$$\cos\theta = (1-\xi)\mathcal{D}_{i+1} + \xi\mathcal{D}_i$$

where $\mathcal{D}_i \equiv \bar{d}_i/d_s$, the difference of the center from the interface scaled by the domain radius.

The other p.d.f. can be sampled in a similar fashion by solving for ℓ from

$$\frac{d_I}{1-d_I/d_s}\int_0^{\ell}\frac{\ell d\ell}{(d_I^2+\ell^2)^{3/2}} = \xi$$

Solving this we get,

$$\ell = d_s\mathcal{D}_I\left[\frac{1}{[1-(1-\mathcal{D}_I)\xi]^2}-1\right]^{1/2}$$

This completes the description of sampling Eq.(5.12).

Appendix B

The WOS Algorithm

The "Walk On Spheres" algorithm can be summed up by the following algorithm.

1. Initialize the runner at the point where the potential is required.
2. Determine the radius of the maximum sphere
3. Obtain the contribution from the first domain.
4. Uniformly sample the surface of the domain.
5. Determine if on/near the external surface.

   If on surface collect boundary value.

   while(not on surface)

   (a) Determine radius of maximum sphere

   (b) Obtain domain contribution.

   (c) Walk On Spheres.

   (d) check if on surface.
6. Collect the entire contribution from the walk.
7. Loop over the walk and particles.
8. Obtain averages and statistics.

This is the generic algorithm, for any specific geometry, the algorithm to determine the radius of the maximum sphere has to be written. Also the sampling of the domain surface may be altered to account for different dielectric media.

Appendix C

Overture to Spherical Quantum Dots

The QMC-WOS method will be particularly applicable to cases where the potential profile is difficult to estimate *a priori* without the knowledge of the charge density. This is particularly true for a certain type of spherical quantum dots. Recent research has shown [24] that the addition energy spectrum of these spherical dots is highly dependent on the dielectric constant of the surrounding medium. We follow this article to emphasize some key points, and propose the application of QMC-WOS to this system.

Recent experiments have allowed the observation of atom like electronic states in strongly-confined semiconductor quantum dots. In these experiments a scanning tunneling microscope (STM) tip is positioned above a specific dot, and the tunneling current-voltage spectrum is acquired by applying a voltage bias between the STM tip and the substrate. The conductance shows a series of peaks which correspond to the electron and hole charging energies. This addition spectrum depends profoundly on the dielectric environment [5]. Indeed semiconductor dots are now made with dielectric coatings: organic molecules, other semiconductors, or glasses. Theoretical understanding of the effect of these media will greatly influence the engineering of such devices.

Consider the dot represented in Fig.(C.1), where a spherical dot of dielectric constant $\varepsilon_{\rm in}$ is embedded within a material of dielectric $\varepsilon_{\rm out}$, in the presence of the STM tip (not shown in figure.) The initial configuration of the system, with energy E_0 consists of a neutral dot in the ground state. The charging energy is given by

$$\mu_1 \equiv E_1 - E_0 = \epsilon_{\rm el} + \Sigma^{\rm pol}_{\rm pol}$$

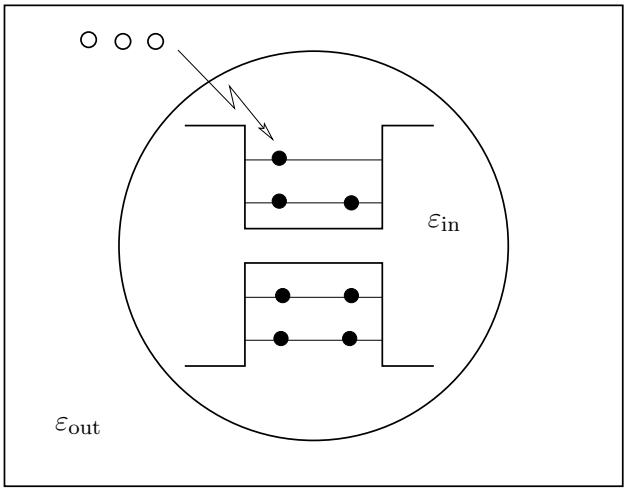

Figure C.1: Process of loading an electron into an otherwise neutral quantum dot

where E_1 is the total energy of the system with one additional electron, ϵ_{el} is the single-particle level with respect to the reference energy, and $\Sigma^{\text{pol}}_{\text{pol}}$ is the self-energy of the additional electron interacting with its own image charge created by the dielectric mismatch at the dot surface. The charging of the second electron will involve the coulomb repulsion which will be the sum of the direct repulsion between the electrons and the polarization contribution arising from the interaction between one electron with the image of the other.

Franceschetti et al [24] carries out atomistic pseudopotential calculations by solving the Poisson equation and the self-energy polarization contribution from the difference of the Green's functions $V_{\text{pol}}(\boldsymbol{r}) = \lim_{\boldsymbol{r}' \longrightarrow \boldsymbol{r}}[G(\boldsymbol{r}, \boldsymbol{r}') - G_{\text{bulk}}(\boldsymbol{r}, \boldsymbol{r}')]$.

Applying QMC-WOS to such systems will be straightforward, we do not have to worry about all the different contributions to the potential, WOS will simply compute the entire potential for us. Also the self-energy polarization term above is simply built into the framework of WOS. The calculations of Franceschetti et al demonstrates that when $\varepsilon_{\text{out}} \ll \varepsilon_{\text{in}}$, the electron-electron and electron-hole interactions are dominated by the surface polarization effects. Thus an exact model of the spherical dot becomes extremely relevant to the problem.

Here we briefly outline a method of evaluating the interaction in the presence of the spherical dot. The exact analytic solution is rather complicated, and the method of images produces a line charge and not a point. However the WOS algorithm is particularly simple and well suited for the purpose.

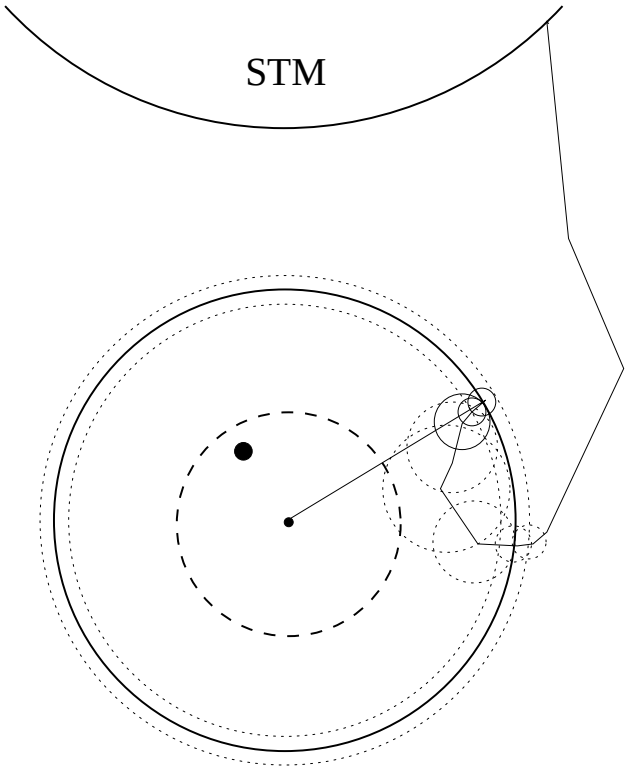

Figure C.2: WOS algorithm for the spherical dot

Divide the dot into two regions by a sphere which has half the radius of the dot. For any point within this sphere (marked by dashed line in Fig.(C.2)), we can use the interpolating technique described in section 2.7.1. Outside this sphere we have to use the regular WOS walk. So for the point shown in the figure we can construct a domain which coincides with the dot, and so on the very first step the walk reaches the dot surface. Here, a small skin region determines the radius of the next domain, and the ratio of the dielectrics determine the transmission or reflection probabilities. If reflected the walk continues by the basic algorithm, if it enters the inner sphere we can use the off-centered domains (and accumulate the corresponding weight), otherwise the walk will simply converge on the dot surface, pass through and continue toward the external boundary of which the STM tip is a part (as shown in the figure).

Appendix D

Effective Units

The Schrödinger equation in SI units is

$$\left[-\frac{\hbar^2}{2m_e}\nabla^2 - \frac{e^2}{4\pi\epsilon_0}\frac{1}{r}\right]\psi(\boldsymbol{r}) = E\psi(\boldsymbol{r}). \tag{D.1}$$

To transform this equation into dimensionless form, we scale the variables by λ ($\boldsymbol{r} \rightarrow \lambda\boldsymbol{r}'$), the above equation becomes

$$\left[-\frac{\hbar^2}{2m_e}\frac{1}{\lambda^2}\nabla'^2 - \frac{e^2}{4\pi\epsilon_0}\frac{1}{\lambda r'}\right]\psi'(\boldsymbol{r}') = E\psi'(\boldsymbol{r}'). \tag{D.2}$$

In order to factor out the constants in front of the kinetic and potential terms, we have to set

$$\frac{\hbar^2}{m_e}\frac{1}{\lambda^2} = \frac{e^2}{4\pi\epsilon_0}\frac{1}{\lambda} = E_\alpha$$

The value of the scaling factor which allows for this factorization to be possible is

$$\lambda = \frac{\hbar^2/m_e}{e^2/(4\pi\epsilon_0)}$$

Setting $E' = E/E_\alpha$, we can rewrite the Schrödinger equation in atomic units

$$\left[-\frac{1}{2}\nabla^2 - \frac{1}{r}\right]\psi'(\boldsymbol{r}) = E'\psi'(\boldsymbol{r}).$$

This is equivalent to setting $\hbar = e^2/(4\pi\epsilon_0) = m_e = 1$, and scaling the length scale r and energy E' to the atomic units of Bohr radius and Hartree respectively. Thus

$$\text{Ha} = \frac{m_e e^4}{(4\pi\epsilon_0)^2\hbar^2} = 27.211eV$$

and

$$a_0 = \frac{\hbar^2/m_e}{e^2/(4\pi\epsilon_0)} = 0.52918\mathring{A}.$$

If the system is some material in which the relative permittivity is ϵ and the electron has an effective mass of $m^\star m_e$ instead of that in vacuum, then these length and energy units scale differently and we have to use the effective units instead of the atomic units to properly represent the scales involved in the problem. It is easy to see that by replacing $\epsilon_0 \to \epsilon\epsilon_0$ and $m_e \to m^\star m_e$ we get

$$a_0^\star = \frac{\epsilon}{m^\star} a_0$$

and

$$\text{Ha}^\star = \frac{m^\star}{\epsilon^2}\text{Ha}$$

Appendix E

Cubic Splines

The interpolation problem can be stated as follows. Given $n+1$ points (x_i, y_i) for $i = 0 \dots n$, find a (smooth) function $g(x)$ satisfying

$$g(x_i) = y_i. \quad i = 0, \dots, n.$$

Obviously, an arbitrarily large number of functions could be constructed to satisfy the above constrains. For practical purposes, $g(x)$ should be a function that is inexpensive to compute; polynomials turn out to be a very efficient choice, i.e. $g(x) \equiv p_n(x)$ a polynomial of degree n.

We will first introduce a specialized problem for ease of understanding the spline interpolation. The following is a cubic Hermite interpolation, is easier to understand, and we will develop the cubic spline scheme based on the ideas developed here.

Let $x_1 < x_2$. Given $y(x_i) = f(x_i),\ i = 1, 2$, i.e. the values of the function $f(x)$ at points x_1 and x_2, let's solve a very special case:

Find a cubic polynomial $P(x)$ such that

$$P(x_1) = f(x_1), P'(x_1) = f'(x_1), P(x_2) = f(x_2), P'(x_2) = f'(x_2). \tag{E.1}$$

In other words, we want to find a polynomial $P(x)$ which not only fits the functional values $f(x)$ at the two points x_1 and x_2, but also the derivative $f'(x)$ at those two points. So the polynomial has to satisfy four conditions. To solve this we use the approach of Lagrange; the idea is to consider the special data sets first and find the so called "fundamental polynomials". So let's first find P_1

such that

$$P_1(x_1) = 1, P_1'(x_1) = 0, P_1(x_2) = 0, P_1'(x_2) = 0. \tag{E.2}$$

Since $P_1(x)$ has a double zero at x_2 and an extrema at x_1, we consider a product form that is linear in x_1 and quadratic in x_2. Thus $P_1(x) = (x - x_2)^2[a + b(x - x_1)]$ for some a And b. Now fitting the above conditions on $P_1(x)$ we find $a = 1/(x_1 - x_2)^2$ and $b = -2/(x_1 - x_2)^3$.

Similarly we define three more polynomials, each to appropriately account for each of the conditions in Eq.(E.1), for example Q_1 is defined by

$$Q_1(x_1) = 0, Q_1'(x_1) = 1, Q_1(x_2) = 0, Q_1'(x_2) = 0.$$

and $Q_1(x) = a(x - x_1)^2(x - x_1)$. So $P_i(x)$ fits the function at x_i, and $Q_i(x)$ fits the derivative at x_i, for $i = 1, 2$. So the polynomial $P(x)$ can be expressed as

$$P(x) = f(x_1)P_1(x) + f'(x_1)Q_1(x) + f(x_2)P_2(x) + f'(x_2)Q_2(x). \tag{E.3}$$

So from the above equation we see that

$$(x - x_1)^2, (x - x_1)^2(x - x_2), (x - x_2)^2, (x - x_2)^2(x - x_1)$$

is a good basis for cubic Hermite interpolation. Redefine $h = x_2 - x_1$, and $t = (x - x_1)/h$, and we can simplify the expressions

$$P(x) = f(x_1)p_1(t) + f(x_2)p_2(t) + h[f'(x_1)q_1(t) + f'(x_2)q_2(t)],$$

with

$$p_1(t) = (t - 1)^2(1 + 2t), \qquad q_1(t) = t(t - 1)^2$$

and

$$p_2(t) = t^2(3 - 2t), \qquad q_2(t) = t^2(t - 1).$$

These will be very useful in the discussion of splines. In Fig.(E.1) we plot these functions. Extending

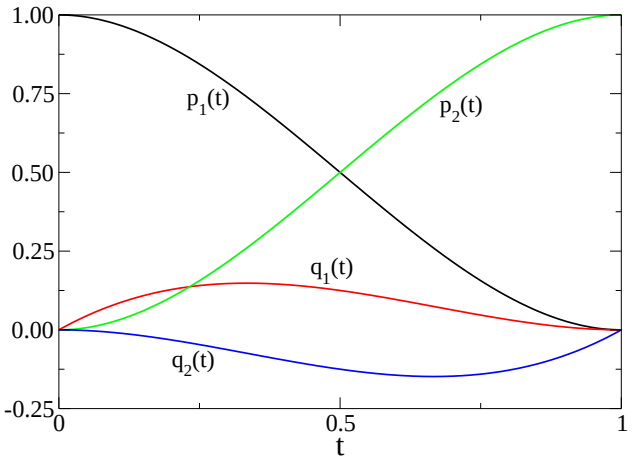

Figure E.1: The polynomial basis functions for interpolation. The range $[x_1, x_2]$ has been mapped into $[0, 1]$ with the choice of the parameter t. Note the properties of these functions; $p_1(t)$ is 1 at 0 and 0 at 1, conversely for $p_2(t)$. As for the $q_i(t)$ functions, their derivative vanishes at one of the ends.

the above idea of interpolation between two points to an arbitrary range $[x_1, x_k]$, we can construct a piecewise cubic Hermite interpolation. It has the following properties

1. The interpolating function $s(x_i)$ equals the given functional value $y(x_i)$ at every data point x_i, i.e. $s(x_i) = y(x_i)\ \forall i = 1, \ldots, k$

2. $s(x)$ is singly differentiable in the range $[x_1, x_k]$.

3. $s(x)$ coincides with a cubic polynomial on every subinterval $[x_{i-1}, x_i]\ \forall\ i = 1, \ldots, k$.

E.1 Cubic Splines

The cubic splines have the same properties as above, except that we require that the interpolating function be doubly differentiable over the entire range, unlike the Hermite interpolation where it is only singly differentiable.

So if we require

$$s(x_i) = y_i, \quad i = 0, \ldots, k$$

then there are $k+1$ interpolation conditions, and we need to impose two more (linear) independent boundary conditions to achieve uniqueness. The commonly used boundary conditions are

1. $s''(x_0) = s''(x_k) = 0$. (natural spline) In this case we assume that the second derivative vanishes at either end point.

2. $s'(x_0) = y'_0, s'(x_k) = y'_k$ (complete spline), we fit the first derivative at the end points.

and there can be many other boundary conditions like "periodic" or "not-a-knot", but we primarily focus on the natural spline, vanishing second derivative is a sufficiently good assumption for our purposes.

We will be computing the interpolating cubic splines by the method of the m-relations which is a very efficient numerical algorithm. Note that a spline $s(x)$ is also a piecewise cubic Hermite interpolating functions. Hence the spline $s(x)$ can also be expressed in the form

$$s(x) = y_{i-1}p_1(t) + y_i p_2(t) + h_i[m_{i-1}q_1(t) + m_i q_2(t)], \tag{E.4}$$

where t and h_i are as described before and $m_i = s'(x_i) \; \forall \; i = 0, \ldots, k$ represents the first derivative at each point. The problem thus boils down to determining the m_is at each point.

To find the m_is, we can use the continuity of $s''(x)$ at each x_i for $i = 1, \ldots, k-1$. Differentiating Eq.(E.4) and after some algebra we find that

$$s'' = y_{i-1}\frac{12t-6}{h_i^2} + y_i\frac{6-12t}{h_i^2} + m_{i-1}(1-4t+3t^2) + m_i t(3t-2), \quad x \in [x_{i-1}, x_i].$$

Therefore,

$$s''(x_i^-) = y_{i-1}\frac{6}{h_i^2} + y_i\frac{-6}{h_i^2} + m_{i-1}\frac{2}{h_i} + m_i\frac{4}{h_i}, \quad i = 1, \ldots, k$$

and

$$s''(x_i^+) = y_{i-1}\frac{-6}{h_i^2} + y_i\frac{6}{h_i^2} + m_{i-1}\frac{-4}{h_i} + m_i\frac{-2}{h_i}, \quad i = 0, \ldots, k-1.$$

Now from the continuity of the second derivative (a requirement for the spline) we equate the two, i.e. $s''(x_i^-) = s''(x_i^+)$ and rearranging in terms of the unknown m_is we get

$$\lambda_i m_{i-1} + 2m_i + \mu_i m_{i+1} = 3\lambda_i\frac{y_i - y_{i-1}}{h_i} + 3\mu_i\frac{y_{i+1} - y_i}{h_{i+1}}, \quad i = 1, \ldots, k-1.$$

where $\lambda_i = h_{i+1}/(h_i + h_{i+1})$ and $\mu_i = 1 - \lambda_i$ for all interior points $x_i, i = 1, \ldots, k-1$.

Now we can use the boundary condition for the natural splines, and set the second derivative at the two end points to zero. These will give us two additional equations. This can be summarized by $k+1$ equations which can be solved by simple linear algebra techniques like Gaussian elimination. These can be rewritten in a more illustrative form:

$$
\begin{array}{ccccccccccccc}
2m_0 & + & m_1 & & & & & & & & & = & d_0 \\
\lambda_1 m_0 & + & 2m_1 & + & \mu_1 m_2 & & & & & & & = & d_1 \\
 & & \lambda_2 m_1 & + & 2m_2 & + & \mu_2 m_3 & & & & & = & d_2 \\
 & & & & & & & \ddots & & & & & \\
 & & & & & & & & \lambda_{k-1} m_{k-2} & + & 2m_{k-1} + \mu_{k-1} m_k & = & d_{k-1} \\
 & & & & & & & & & & m_{k-1} + 2m_k & = & d_k
\end{array}
$$

with

$$d_0 = 3\frac{y_1 - y_0}{h_1}, \quad d_k = 3\frac{y_k - y_{k-1}}{h_k},$$

and

$$d_i = 3\lambda_i \frac{y_i - y_{i-1}}{h_i} + 3\mu_i \frac{y_{i+1} - y_i}{h_{i+1}}$$

E.2 TriCubic Splines

Interpolation in three dimensions will follow exactly similar approach, except that we have to account for the cross derivatives as well. In a rectangular grid, the tricubic splines will satisfy the following conditions:

1. $S(\boldsymbol{r})$ is a cubic polynomial in $\boldsymbol{r}$:

$$S(\boldsymbol{r}) = \sum_{l,m,n=0}^{3} a_{l,m,n}^{(i,j,k)} (x - x_i)^l (y - y_j)^m (z - z_k)^n$$

2. $S(\boldsymbol{r})$ is doubly differentiable, i.e. the following functions are continuous:

$$\frac{\partial^{\alpha+\beta+\gamma} S(\boldsymbol{r})}{\partial x^\alpha \partial y^\beta \partial z^\gamma}, \quad \alpha, \beta = 0, 1, 2$$

Thus the interpolation condition involves 64 coefficients at each point, namely the values of the following terms

$$f,\ \frac{\partial f}{\partial x},\ \frac{\partial f}{\partial y},\ \frac{\partial f}{\partial z},\ \frac{\partial^2 f}{\partial x \partial y},\ \frac{\partial^2 f}{\partial y \partial z},\ \frac{\partial^2 f}{\partial x \partial z},\ \frac{\partial^3 f}{\partial x \partial y \partial z}$$

evaluated at each point. Hence the value of the interpolating function $S(x, y, z)$ at any point $\boldsymbol{r}(x, y, z)$ is dependent on the above eight coefficients at each of the eight corner points of the cubic grid the point $\boldsymbol{r}$ resides in, i.e. a total of $8 \times 8 = 64$ coefficients in all. Then on each of these cubes, we have 64 interpolation conditions for the 64 coefficients of the tricubic polynomial that represents the tricubic spline. The same ideas of the piecewise cubic Hermite interpolation are used.

In the same notation as in the case of the Hermite polynomial, we define the following;

$$h_i^{(x)} = x_{i+1} - x_i, h_j^{(y)} = y_{j+1} - y_j, h_k^{(z)}(z) = z_{k+1} - z_k$$

and three four-vectors

$$\begin{aligned}
\boldsymbol{a}(u) &= [p_1(u), p_2(u), h_i^{(x)} q_1(u), h_i^{(x)} q_2(u)] \\
\boldsymbol{b}(v) &= [p_1(v), p_2(v), h_j^{(y)} q_1(v), h_j^{(y)} q_2(v)] \\
\boldsymbol{c}(w) &= [p_1(w), p_2(w), h_k^{(z)} q_1(w), h_k^{(z)} q_2(w)]
\end{aligned}$$

where

$$u = (x - x_i)/h_i^{(x)}, v = (y - y_j)/h_j^{(y)}, w = (z - z_k)/h_k^{(z)}$$

Then we define a three tensor F_{ijk} $i, j, k = 0, \ldots 3$ which contains the 64 coefficients of the function and its derivatives as described in the previous paragraph. For each of the indices, the values denote the following.

$$0 = f_i, 1 = f_{i+1}, 2 = f_i', 3 = f_{i+1}'$$

For example,

$$F_{013} = \frac{\partial f}{\partial z}\Big|_{i,j+1,k+1}, F_{332} = \frac{\partial^3 f}{\partial x \partial y \partial z}\Big|_{i+1,j+1,k} \text{ etc.}$$

With this notation the expression for the spline becomes simple

$$S(\boldsymbol{r}) = \sum_{i,j,k=0}^{3} F_{ijk} a_i(u) b_j(v) c_k(w)$$

The m-derivatives are evaluates as follows. We start by evaluating all three first derivatives for all the grid points following the method outlined for one dimensional splines. Then use these values in the same matrix equation to calculate the second derivatives and so on. This needs to be done only once at the beginning of the calculation, so when the actual interpolation is taking place, it involves only the addition (and multiplication) of 64 terms.

E.3 Wave function and Derivatives

Since the second derivative of the cubic spline is continuous, these can be used to interpolate tabulated orbital values and the kinetic energy computed from that interpolation will be continuous. However the kinetic energy is guarantied to be not smooth.

First, we see that the spline $S(\boldsymbol{r})$ depends on the coordinates only through the (u, v, w) parameters, and so we simply need to evaluate the derivative of the p and qs. This proves to be a simple task.

Now consider the fact that the splines are cubic polynomials and so their second derivative will be linear. This will imply a function which is continuous but not smooth, and hence the kinetic energy (of the form $-\nabla^2\Psi/\Psi$) is a piecewise smooth function divided by a smooth function will have discontinuous derivatives. This is usually not a problem for diffusion Monte Carlo.

References

[1] Ashcroft N. W. and Mermin N. D., *Solid State Physics*, Sanders College Publishing, 1976.

[2] Ashoori R. C., *Electrons in artificial atoms*, Nature **379** (1996), 413–419.

[3] Bachelier L., *Theorie de la speculation*, Ann. Sci. Ecole. Norm. Sup. **17** (1900), 21–86, (English translation in The Random character of Stock Market Prices, edited by Paul H. Cootner, M.I.T. Press, Cambridge, MA, 1964).

[4] Bevensee R. M., *Probabilistic Potential Theory Applied to Electrical Engineering Problem*, Proceedings of IEEE **61** (1973), no. 4, 423.

[5] Brus L. E., *A simple model for the ionization potential, electron affinity, and aqueous redox potentials of small semiconductor crystallites*, Journal of Chemical Physics **79** (1983), 5566.

[6] Bryant G. W., Physical Review Letters **59** (1987), 1140.

[7] Caffarel M., Rerat M., and Pouchan C., *Evaluating dynamic multipole polarizabilities and van der Waals dispersion coefficients of two-electron systems with a quantum Monte Carlo calculation: A comparison with some ab initio calculations*, Physical Review A **47** (1993), no. 5, 3704–3717.

[8] Ceperley D. M., *Microscopic Simulations in Physics*, Reviews of Modern Physics **71** (1999), no. 2, S438–S443.

[9] Ceperley D. M. and Alder B. J., *The Low Density Phases of the Electron Gas*, Journal de Physique **C7** (1980), 295.

[10] ———, *The Calculation of the Properties of Metallic Hydrogen using Monte Carlo*, Physica **108B** (1981), 875.

[11] Ceperley D. M., Chester G. V., and Kalos M. H., *Monte Carlo simulation of a many-fermion study*, Physical Review B **16** (1977), no. 7, 3081.

[12] Ceperley D. M. and Dewing M., *The penalty method for random walks with uncertain energies*, Journal of Chemical Physics **10** (1999), no. 20, 9812–9820.

[13] Clementi E. and Roetti C., Atomic Data and Nuclear Data Tables **14** (1977), 177.

[14] Courant R., Friedrichs K., and Lewy H., *Uber die partiellen Differenzengleichungen der mathematischen Physik*, Math. Ann. **100** (1928), 32–74, (English translation in IBM J. Res. Develop. 11, 215-234 (1967).

[15] David R. Lide (ed.), *CRC Handbook of Chemistry and Physics*, 85 ed., CRC Press, 2004, pp 12-18.

[16] de Oliveira M. J., *Ground-state properties of the spin 1/2 antiferromagnetic Heisenberg chain obtained by use of a Monte Carlo method*, Physical Review B **48** (1993), no. 9, 6141–6143.

[17] DeLaurentis J. M. and Romero L. A., *A Monte Carlo Method for Poisson's Equation*, Journal of Computational Physics **90** (1990), 123–140.

[18] Doob J. L., *Semimartingales and subharmonic functions*, Trans. Amer. Math. Soc. **77** (1954), 86–121.

[19] Einstein A., *Investigations on theTheory of the Brownian Movement*, Dover, New York, 1956, translated by A. D. Cooper.

[20] Elzerman J. M., Hanson R., Greidanus J. S., Willems van Beveren L. H., Franceschi S. De, and Vandersypen L. M, *Few-electron quantum dot circuit with integrated charge read out*, Physical Review B **67** (2003), 161308(R).

[21] Fahy S., Wang X. W., and Louie S. G., Physical Review Letters **61**, 1631.

[22] Filippi C. and Umrigar C. J., *Correlated sampling in quantum Monte Carlo: a route to forces*, arXiv:cond-mat/991132v1 (1999).

[23] Foulkes W. M. C, Mitas L., Needs R. J., and Rajagopal G., *Quantum Monte Carlo simulations of solids*, Reviews of Modern Physics **73** (2001), no. 1, 33.

[24] Franceschetti A., Williamson A., and Zunder A., *Addition Spectra of Quantum Dots: the Role of Dielectric Mismatch*, Journal of Physical Chemistry **104** (2000), 3398–3401.

[25] Grossman J. C. and Mitas L., Physical Review Letters **74** (1995), 1323.

[26] Hagstrom S. A. and Sims J. S., *High Precision Hy-CI Variational Calculations for the Ground State of Neutral Helium and Helium-Like ions*, The International Journal of Quantum Chemistry. (2002).

[27] Haji-Sheikh A. and Sparrow E. M., *The Solution of Heat Conduction Problems by Probability Methods*, Journal of Heat Transfer **C89** (1967), 121–131.

[28] Hammond B. L., Lester W. A. Jr., and Reynolds P. J., *Monte Carlo Methods in Ab Intio Quantum Chemistry*, vol. 1, World Scientific, 1994.

[29] Harrison Paul, *Quantum Wells, Wires and Dots*, John Wiley and Sons Ltd., 1999.

[30] Hess K., *Advanced Theory of Semiconductor Devices*, Prentice Hall, 1988.

[31] Hirose K. and Wingreen N. S., *Spin-density-functional thoery of circular and elliptic quantum dots*, Physical Review B **59** (1999), no. 7, 4604–4607.

[32] Hoffman C. and Bronsvort W. (eds.), *Fast Monte Carlo Domain Sampling for Discrete Field Value Estimation*, Atlanta, GA, May 1997, pp. 354-363.

[33] Jackson J. D., *Classical Electrodynamics*, 2 ed., John Wiley and Co., 1974.

[34] ———, *Classical Electrodynamics*, 2 ed., John Wiley and Co., 1974, pp 56.

[35] Jaswal S. S. and Sharma T. P., J. Phys. Chem. Solids **34** (1973), 509.

[36] Jere J. N. and LeCoz Y. L., *An Improved Floating-Random-Walk Algorithm for Solving the Multi-Dielectric Dirichlet Problem*, IEEE Transactions on Microwave Theory and Techniques **41** (1993), no. 2, 325–329.

[37] Kakutani S., *Two-dimensional Brownian motion and harmonic functions*, Proc. Imp. Acad. (Tokyo) **20** (1944), 706–714.

[38] Kalos M. H., Levesque D., and Verlet L., *Helium at zero temperature with hard-sphere and other forces*, Physical Review A **9** (1974), no. 5, 2178.

[39] Kalos Malvin H. and Whitlock Paula A., *Monte Carlo Methods*, vol. I: Basics, John Wiley & Sons, 1986.

[40] Kastner M. A., *The single-electron transistor*, Review of Modern Physics **64** (1992), no. 3, 849–858.

[41] Kim Y., Lee I., Hood R. Q., and Martin R. M., *Two-dimensional limit of exchange-correlation energy functional approximations*, Physical Review B **61** (2000), 5202–5211.

[42] Kohn W. and Sham L. J., Physical Review **140** (1965), A1133.

[43] Koskinen M., Manninen M., and Reimann S. M., *Hund's Rules and Spin Density Waves in Quantum Dots*, Physical Review Letters **79** (1997), no. 7, 1389–1392.

[44] Kouwenhoven L. P. and McEuen P. L., *Nanotechnology*, p. 471, 1999.

[45] Kouwenhoven L. P., Oosterkamp T. H., Danoesastro M. W. S., Eto M., Austing D. G., Honda T., and Tarucha S., *Excitation Spectra of Circular Few-Electron Quantum Dots*, Science **278** (1997), 1788–1792.

[46] Liu Z., Shang S., and Kalos M. H., *Model fermion Monte Carlo method with antithetical pairs*, Physical Review E **50** (1994), no. 4, 3220.

[47] Matagne P. and Leburton J.P., *Self-consistent simulations of a four-gated vertical quantum dot*, Physical Review B **65** (2002), 155311.

[48] Matagne P., Wilkens T., Leburton J. P., and Martin R. M., *Hybrid LSDA/Diffusion Quantum Monte-Carlo Method for Spin Sequences in Vertical Quantum Dots*, Proceedings of the 8th International Workshop on Computational Electronics (ICWE-8), Journal of Computational Electronics **1** (2002), 135.

[49] Melnikov D., Zhang L. X., and Leburton J.P., *DFT Calculations of Laterally Coupled Quantum Dots*, private communication, 2005, The Computation Electronics Group provided the DFT solutions of their calculations. This involved the device structure, the converged potential, charge density distribution, and trial wave-function. The input data was distributed on a grid, and we interpolated their values using tricubic splines to obtain values at intermediate points.

[50] Melnikov D., Zhang L.X., and Leburton J.P., private correspondence.

[51] Metropolis N., Rosenbluth A. W., Rosenbluth M. N., Teller A. H., and Teller E., *Equations of state calculations by fast computing machines*, Journal of Chemical Physics **21** (1953), 1087.

[52] Metropolis N. and Ulam S., *The Monte Carlo Method*, Journal of American Statistical Associaton **44** (1949), 335.

[53] Moroni S., Ceperley D. M., and Senatore G., Physical Review Letters **75**, 689.

[54] Muller M. E., *Some Continuous Monte Carlo Methods for the Dirichlet Problem*, Annals of Mathematical Statistics **27** (1956), 567–589.

[55] Natoli V., Martin R. M., and Ceperley D. M., Physical Review Letters **70** (1993), 1952.

[56] Pauling L, Proc. Roy. Soc., London **A114** (1927), 181.

[57] Perdew J. and Wang Y., *Accurate and simple analytic representation of the electron-gas correlation energy*, Physical Review B **45** (1992), no. 23, 13244–13249.

[58] Petroff P. M., Gossard A. C., Logan R. A., and Wiegmann W., *Toward quantum well wires: Fabrication and optical properties*, Applied Physics Letters **41** (1982), 635.

[59] Philippe Matagne, *Quantum Modelling of Single-Electron Charging in Vertical Quantum Dots*, Ph.D. thesis, Universite de Liege, 2001.

[60] Pickles J. H., *Monte Carlo field calculations*, Proceedings of IEE **124** (1977), no. 12, 1271.

[61] Port S. C. and Stone C. J., *Brownian Motion and Classical Potential Theory*, Probability and Mathematical Statistis, Academic Press, New York, 1978.

[62] Reimann S. M. and Manninen M., *Electronic structure of quantum dots*, Reviews of Modern Physics **74** (2002), 1283–1342.

[63] Reinhard Schlott, *A Monte Carlo Method for the Dirichlet Problem of Dielectric Wedges*, IEEE Transactions on Microwave Theory and Techniques **36** (1988), no. 4, 724–730.

[64] Reynolds P. J., Ceperley D. M., Alder B. J., and Lester W. A., Journal of Chemical Physics **77** (1982), 5593.

[65] Rontani M., Rossi F., Manghi F., and Molinari F., *Coulomb Correlation Effects in Semiconductor Quantum Dots*, Physical Review B **59** (1999), no. 15, 10165.

[66] Royer G. M., *A Monte Carlo Procedure for Potential Theory Problems*, IEEE Transactions on Microwave Theory and Techniques **19** (1971), no. 10.

[67] Saarikoski H., Rasanen E., Siljamaki S., Harju A., Puska M. J., and Nieminen R. M., *Electronic properties of model quantum-dot structures in zero and finite magnetic fields*, The European Physical Journal B **26** (2002), 241–252.

[68] Umrigar C. J., Nightingale M. P., and Runge K. J., *A diffusion Monte Carlo Algorithm with very small time-step errors*, Journal of Chemical Physics **99** (1993), no. 4, 2865–2890.

[69] Umrigar C. J., Wilson K. G., and Wilkins J. W., *Optimized Trial Wave Functions for Quantum Monte Carlo Calculations*, Physical Review Letters **60** (1988), no. 17, 1719–1722.

[70] Veillard A. and Clementi E., *Corrleation Energy in Atomic Systems. V. Degeneracy Effects for the Second-Row Atoms*, Journal of Chemical Physics **49** (1968), no. 5, 2415.

[71] Wiener J., *Certain notions in potential theory*, J. Math. Phys. **3** (1924), 24–51.

[72] Wilkens T. J., *Accurate Treatments of Electronic Correlation: Phase Transitions in an Idealized 1D Ferroelectric and Modelling Experimental Quantum Dots*, Ph.D. thesis, University of Illinois at Urbana Champaign, 2001.

[73] Yannouleas C. and Landman U., *Magnetic-Field Manipulation of Chemical Bonding in Artificial Molecules*, International Journal of Quantum Chemistry **90** (2002), 699–708.

[74] Zachmanoglou E. C. and Thoe D. W., *Introduction to Partial Differential Equations with Applications*, Dover Publications, Inc., 1976.

[75] Zaloj V. and Agmon N., *Electrostatics by Brownian dynamics: solving the Poisson euqation near dielectric interfaces*, Chem. Phys. Lett **270** (1997), 476–483.

[76] Zhang L. X., Matagne P., and Leburton J.P., *Single electron charging and detection in a laterally-coupled quantum dot circuit in the few-electron regime*, Physical Review B **69** (2004), 245301.

Author's Biography

Dyutiman Das was born in Calcutta, West Bengal, India on January 12th, 1976. He obtained his bachelors in physics from Presidency College, Calcutta and went on to get a masters from The Indian Institute of Technology, Kanpur India. He arrived in the United States in 1999, to pursue Ph.D. in physics at the University of Illinois at Urbana Champaign. In collaboration with Prof. Richard M. Martin and Jeongnim Kim, he worked on quantum Monte Carlo methods, and developed a new technique of incorporating the potential in Monte Carlo calculations.